MODELING, MODULATION AND CONTROL OF HEXVERTER–BASED MODULAR MULTILEVEL CONVERTERS

by

HÉCTOR R. ROBLES–CAMPOS

B.S., Universidad Panamericana Campus Guadalajara, 1997

M.S., University of Colorado Denver, 2018

A thesis submitted to the
Faculty of the Graduate School of the
University of Colorado in partial fulfillment
of the requirements for the degree of
Doctor of Philosophy
Engineering and Applied Science
2022

This thesis for the Doctor of Philosophy degree by
Héctor R. Robles–Campos
has been approved for the
Engineering and Applied Science Program
by

Fernando Mancilla–David, Advisor
Miloje Radenkovic, Chair
Alireza Vahid
Tom Altman
Alejandro Angulo Cardenas

April 27, 2022

Robles–Campos, Héctor R. (Ph.D., Engineering and Applied Science)

Modeling, modulation and control of Hexverter–based modular multilevel converters

Thesis directed by Professor Fernando Mancilla–David

ABSTRACT

Electrical power extraction from renewable energy sources such as photovoltaics (PV), wind farms, and some others, have their own technical challenges. It is necessary to perform the power processing tasks according to the nature of the power supply and, at the same time, it is required to be compliant with technical regulations and particular needs of final users. These tasks are achieved with the development of power electronics converters and suitable control systems.

Modular multilevel converters (MMCs) have been during the last years, and will continue to be in the near future, a trending research topic. To better process the electrical power, MMCs can be used where two or three level power converters are used today. This is essentially due to multiple advantages, such as, *(i)* inherent fault tolerance or some times called redundancy, *(ii)* application in medium and high power levels, *(iii)* high scalability: in function of the number of power modules, *(iv)* better quality of output power, and *(v)* comparatively low switching frequency.

Among the MMCs power converters there is a particular multilevel topology, called “Hexverter”, suitable to connect two different three–phase AC systems typically running at two different frequencies. In this dissertation studies and solutions developed for a Hexverter–based system spans from its modeling, control and detailed assessment of modulation strategies.

Moreover, it is a fact that PV technology is a key tool that have enabled a significant increment of electrical power extraction from renewable energy sources. However, a phenomenon known as partial shading is a major source of power losses for PV plants. The presented research spans from PV array modeling, bypass diodes modeling, and an application example of the proposed model comprising a comparative evaluation of several maximum power point tracking algorithms operating in a large grid–connected photovoltaic power plant. Simulation–based and experimental validation results show the performance of the proposed solutions.

The form and content of this abstract are approved. I recommend its publication.

Approved: Fernando Mancilla–David

DEDICATION

This thesis is dedicated to my family and entourage who have supported me all the way since the beginning of my studies. In particular, this work is dedicated to my parents Lucio and María, they provide me a great source of motivation and inspiration. To all my teachers, students, colleagues and friends. Lastly, this thesis is dedicated to all who have encouraged me to go further during my life.

ACKNOWLEDGMENT

Foremost, I would like to express my deepest gratitude to my advisor, Prof. Fernando Mancilla–David, for his guidance, valuable advice and support during the whole period of my doctoral studies. As a student coming from a developing country I would not have been able to come this far without the support provided by Prof. Mancilla–David. He has guided me in my research endeavors, and has always ensured that high standards were maintained in all our research enterprises.

I acknowledge my deepest gratitude to the Mexican institution "Consejo Nacional de Ciencia y Tecnología"–(CONACYT) and to "Universidad Panamericana", without their financial support during my whole academic process this significant achievement would not be possible.

I would also like to thank my thesis committee members, Dr. Miloje Radenkovic, Dr. Alireza Vahid, Dr. Tom Altman and Dr. Alejandro Angulo, for their valuable time invested for reviewing this dissertation and for their suggestions provided on improving my thesis.

In particular, I would like to thank Dr. Alejandro Angulo and Dr. Pedro García–Vite for enhancing the present dissertation through many academic discussions and for his assistance during this journey.

Sincere thanks go to all my research group members, specially thanks to my dear friends Miguel Carrasco, Carlos A. Soriano–Rangel, Bernardo Azuaje–Berbecí, Gadi Ogbogu and Christopher Scheller for their friendship, academic discussions, assistance and motivation.

I sincerely acknowledge the academic body of Universidad Panamericana, Dr. Antonio Valderrabano–González, Dr. Julio César Rosas–Caro, Dr. Sergio Velázquez–Rodríguez, Dr. Francisco Orozco–Argote and Dr. Antonio Esquivias–Romero, for their support and motivation. Particularly, I would like to express my deepest gratitude to Dr. Abraham Mendoza–Andrade, without his support, motivation and friendship this dream would not be possible.

Finally, and most importantly, I would like to thank my family. Thank you to my wife Ángeles, and my children Monse, Roger and Santi. They were always there cheering me up and stood by me through the good and bad times.

TABLE OF CONTENTS

CHAPTER

1. INTRODUCTION 1
    1.1 Background 1
    1.2 Objectives 2
2. AC–AC MODULAR MULTILEVEL CONVERTERS 4
    2.1 Motivation & present state of knowledge 4
    2.2 Technical approach 4
        2.2.1 Modular multilevel converter in back–to–back configuration . 5
        2.2.2 Modular multilevel Matrix converter 5
        2.2.3 Modular multilevel Hexverter 6
            2.2.3.1 Hexverter principle of operation 7
3. MODELING & CONTROL APPROACH IN THE *DQ* REFERENCE FRAME FOR HEXVERTER–BASED SYSTEMS 10
    3.1 Motivation & present state of knowledge 10
    3.2 Technical approach 11
        3.2.1 Branch voltages and currents analysis 11
        3.2.2 Branch voltages 12
        3.2.3 Branch currents 13
        3.2.4 Synthesized branch current controller in the *dq* reference frame 15
        3.2.5 Hexverter {abc} side, differential equations 15
            3.2.5.1 From {abc} to *dq* transformation 15
        3.2.6 Hexverter {123} side, differential equations 16
            3.2.6.1 From {123} to *dq* transformation 16
        3.2.7 Control approach 17
        3.2.8 Hexverter–based system integration 18
        3.2.9 Branch current controllers 19

3.2.10 Modulator and voltage balancing algorithm 20
3.3 Simulation results 20
3.3.1 Performance assessment of the proposed control scheme . . . 21
3.4 Conclusions 23
4. DETAILED ASSESSMENT OF MODULATION STRATEGIES FOR HEXVERTER–BASED MODULAR MULTILEVEL CONVERTERS 26
4.1 Motivation & present state of knowledge 26
4.2 Technical approach 27
4.2.1 Modeling and control approach in a unified two–frequency *dq* framework 28
4.2.1.1 Branch current controllers 28
4.2.2 Modulation strategies 30
4.2.2.1 Nearest level control modulation 30
4.2.2.2 Phase disposition–sinusoidal pulse width modulation . 31
4.2.3 Proposed “virtual V_{C}^2 controller” 33
4.2.4 Hexverter–based system integration 35
4.3 Detailed validation 37
4.3.1 Assessment results of NLC 37
4.3.2 Assessment results of PD–SPWM 39
4.3.3 NLC and PD–SPWM discussion of results 41
4.3.4 Performance of “virtual V_{C}^2 controller” 42
4.3.5 Test Case I 42
4.3.6 Test Case II 44
4.3.7 Assessment of harmonic spectrum and total harmonic distortion 47
4.3.8 Single phase voltage THD assessment under NLC 47
4.3.9 Single phase voltage THD assessment under PD–SPWM . . . 50
4.3.10 Single phase current THD assessment under NLC 50

4.3.11 Single phase current THD assessment under PD–SPWM . . . 50

4.4 Conclusions 51

5. DETAILED MODELING OF LARGE SCALE PHOTOVOLTAIC POWER PLANTS UNDER PARTIAL SHADING CONDITIONS 53

5.1 Motivation & present state of knowledge 53

5.2 Technical approach 60

5.2.1 Mathematical modeling 60

5.2.2 Thermoelectric model of $\mathcal{P}_{\text{cell}}$ 62

5.2.2.1 Electrical model of $\mathcal{P}_{\text{cell}}$ 62

5.2.2.2 Thermal model of $\mathcal{P}_{\text{cell}}$ 65

5.2.2.3 Unified model of $\mathcal{P}_{\text{cell}}$ 65

5.2.3 Thermoelectric model of $\mathcal{P}_{\text{diode}}$ 65

5.2.3.1 Electrical model of a single BPD 66

5.2.3.2 Thermal model of a single BPD 67

5.2.4 Unified model of $\mathcal{P}_{\text{diode}}$ 67

5.2.5 Thermal model of the BPD junction box 68

5.2.5.1 Estimation of BPD T_{j} considering its junction box physical properties and thermal effects 69

5.2.5.2 Estimation of BPD T_{j} considering junction box experimental results 71

5.2.5.3 Comparison of modeled vs experimental results of BPD T_{j} 72

5.2.6 Model of $\mathcal{P}_{\text{block}}$ 73

5.2.7 Model of $\mathcal{P}_{\text{panel}}$ 74

5.2.8 Model of $\mathcal{P}_{\text{array}}$ 76

5.3 Detailed validation 77

5.3.1 Case study I 78

5.3.2 Case study II 82

5.3.3 Case study III 82

5.3.4 Case study IV 84

5.4 Application example 86

5.4.1 Partial shading due to a cloud movement 86

5.4.2 Single–stage PV system 88

5.4.3 Simulation results 91

5.5 Conclusions 92

6. CONCLUDING REMARKS 96

6.1 Contributions 96

6.2 Research products 97

6.3 Conclusions 97

6.4 Future work 99

REFERENCES 100

LIST OF TABLES

TABLE

3.1 Simulation parameters 21

4.1 Simulation parameters. 38

4.2 Nominal parameters of the IGBT and Diode part number: IRG4BC30KDPbF and operational conditions. 45

5.1 Illustration of the lookup table 71

5.2 Electrical and temperature parameters of PV panel Canadian Solar CS6X–325P at STC 79

5.3 Reference parameters of PV panel Canadian Solar CS6X–325P at STC . 79

5.4 Reference parameters of LITEON Schottky barrier diode 15SQ045 80

5.5 $\text{RMS}_{\text{error}}$ in % between SPV panel block and $\mathcal{P}_{\text{panel}}$ model 81

5.6 Case study I: simulation results 81

5.7 Case study II: simulation results 83

5.8 Case study III: simulation results 84

5.9 Case study IV: results 86

5.10 Performance of conventional and enhanced MPPT algorithms 93

LIST OF FIGURES

FIGURE

2.1 Back to back configuration of the modular multilevel converter (MMC). . 5

2.2 Modular multilevel matrix converter (M3C). 6

2.3 AC–AC Hexverter topology. 7

2.4 AC–AC Hexverter equivalent circuit. 8

3.1 Phasor diagram of branch voltages. 13

3.2 Phasor diagram of branch currents. 14

3.3 Hexverter–based system integration. 19

3.4 Blocks diagram for $i_{\mathrm{b135}}^{\mathrm{abc}}$ current control. 19

3.5 Three–phase powers $\mathrm{P/Q}_{\mathrm{abc}}^{*}$ and $\mathrm{P/Q}_{123}^{*}$ vs filtered measurements. 22

3.6 Branch currents $i_{\mathrm{b135}}^{\mathrm{abc},dq*}$ and $i_{\mathrm{b135}}^{123,dq*}$ vs filtered measurements. 22

3.7 Modulation indices calculated for branches [135]. 23

3.8 Synthesized three–phase voltages and currents. 24

3.9 Synthesized branch voltage v_{b1} and branch current i_{b1}. 25

3.10 NLC VBA performance. 25

4.1 Block diagrams of current control to determine $m_{\mathrm{b135}}^{\mathrm{xyz}}$. 29

4.2 General flowchart of NLC modulation technique. 30

4.3 NLC VBA flowchart. 31

4.4 12^{th} PD–SPWM carriers and synthesized voltage. 32

4.5 General flowchart of PD–SPWM modulation technique. 32

4.6 PD–SPWM VBA flowchart. 33

4.7 Elements storing energy in the Hexverter system. 34

4.8 Virtual V_{C}^{2} controller block diagram. 35

4.9 Hexverter–based system integration. 36

4.10 NLC: AC three–phase voltages $v_{\mathrm{abc}}, v_{123}$, branch voltage v_{bs1} and branch current i_{b1}. 39

4.11 NLC VBA performance. Top) zoom–out depicting transients at initial conditions. Bottom) zoom–in at steady–state. 40

4.12 PD–SPWM: AC three–phase voltages $v_{\mathrm{abc}}, v_{123}$, branch voltage v_{bs1} and branch current i_{b1}. 40

4.13 PD–SPWM VBA performance. Top) zoom–out depicting transients at initial conditions. Bottom) zoom–in at steady–state. 41

4.14 Test Case I: NLC ΔP value obtained with "virtual V_{C}^2 control". 42

4.15 Test Case I: PD–SPWM ΔP parameter obtained with "virtual V_{C}^2 control". 43

4.16 Test Case II: NLC ΔP value obtained with "virtual V_{C}^2 control". 45

4.17 Test Case II: comparison of ($P^*_{\mathrm{abc}}, Q^*_{\mathrm{abc}}, P^*_{123}$ and P^*_{123}) vs measurements under NLC modulation. 46

4.18 Test Case II: PD–SPWM ΔP value obtained with "virtual V_{C}^2 control". . 46

4.19 Test Case II: comparison of ($P^*_{\mathrm{abc}}, Q^*_{\mathrm{abc}}, P^*_{123}$ and P^*_{123}) vs measurements under PD–SPWM. 47

4.20 Spectrum of v_{a}, v_1 and THD calculations, when NLC modulation technique is utilized. 48

4.21 Spectrum of v_{a}, v_1 and THD results, when PD–SPWM modulation technique is utilized. 49

4.22 Spectrum of i_{a}, i_1 and THD calculations, when NLC modulation technique is utilized. 49

4.23 Spectrum of i_{a}, i_1 and THD results, when PD–SPWM modulation technique is utilized. 51

5.1 Construction of $\mathcal{P}_{\mathrm{array}}$ from partitions $\mathcal{P}_{\mathrm{cell}}$, $\mathcal{P}_{\mathrm{diode}}$, $\mathcal{P}_{\mathrm{block}}$ and $\mathcal{P}_{\mathrm{panel}}$ using the Kyocera KC85TS PV panel as an example. 63

5.2 (a) an array of PV cells, (b) its equivalent thermoelectric model $\mathcal{P}_{\mathrm{cell}}$. . . 66

5.3 (a) an array of BPD, (b) its equivalent thermoelectric model $\mathcal{P}_{\mathrm{diode}}$. . . . 69

5.4 Equivalent junction box thermal model. 69

5.5 (a) Comparison of experimental and proposed model values for T_j, (b) nonlinear surface of $\mathrm{R}_{\theta\mathrm{eq}}$. 72
5.6 Proposed thermoelectric modular model of a PV panel section identified as $\mathcal{P}_\mathrm{block}$. 73
5.7 Improved PV panel representation, named as $\mathcal{P}_\mathrm{panel}$. 75
5.8 Equivalent circuit of $N_\mathrm{ps} \times N_\mathrm{pp}$ array of PV panels, named as $\mathcal{P}_\mathrm{array}$. . . 77
5.9 Case study I: (a) SPV panel block, (b) $\mathcal{P}_\mathrm{panel}$ based model. 80
5.10 Case study I: SPV panel block and $\mathcal{P}_\mathrm{panel}$ model I–V curves comparison at different irradiance values. 81
5.11 Case study II: (a) SPV panel based array, (b) $\mathcal{P}_\mathrm{panel}$ based array. 82
5.12 Case study II: SPV panel based array and $\mathcal{P}_\mathrm{panel}$ based array I–V curves comparison including BPDs and PS. 83
5.13 Case study III: (a) SPV array, (b) $\mathcal{P}_\mathrm{array}$ model based. 84
5.14 Case study III: SPV array and $\mathcal{P}_\mathrm{array}$ model based I–V curves comparison including BPDs and PS. 85
5.15 Case study IV: (a) SPV array, (b) $\mathcal{P}_\mathrm{array}$ model based. 86
5.16 Case study IV: SPV array and $\mathcal{P}_\mathrm{array}$ model based I–V curves comparison including BPDs and PS. 87
5.17 Cloud moving across a PV plant. 88
5.18 Actual G, T_a and V_w profiles that were used during the simulation. . . . 89
5.19 Circuit schematic of the grid–connected single–stage PV plant. 90
5.20 Performance of the IC, P&O, enhanced IC, P&O and, the NN algorithms. 92
5.21 Performance of the MPPT algorithms at specific periods of time. 93

CHAPTER 1

INTRODUCTION

1.1 Background

Among all varieties of power electronic converters, modular multilevel topologies have attracted plenty of research attention within the last decades. This category of power electronic converters can be used where two or three level power converters are used today. Modular multilevel topologies feature advantages when compared to other power converters. The main advantages include, but are not limited to, reduced requirements for series connection of semiconductor devices for same voltage level, inherent redundancy, increased output power quality and relatively low switching frequency. Conversely, a drawback of these topologies is that as the number of level increases, so does the complexity of the control. From this family of power electronic converters there is a particular topology well suited to connect two different three–phase ac systems. It was firstly proposed back in 2010 [1] and it was named "Hexverter". The context and main features of this multilevel power converter are concisely introduce in Chapter II of this dissertation. Nonetheless some control approaches particularly designed in the so called "$\alpha\beta0$" frame for Hexverter–based systems are available in the literature, the modeling and a control approach in a unified two–frequency dq reference frame for a Hexverter–based system is synthesized and validated in Chapter III of this dissertation.

Multilevel topologies family is typically characterized by a number of series connections of power submodules forming a cluster or branch. These power submodules are referred either as full–bridge or half–bridge. The converter voltage rating can be easily enlarged by increasing the number of series–connected submodules per branch. The capacitor voltage of each submodule is floating and it could charge–discharge under operational conditions. Hence, an important control objective is to keep each submodule's capacitor voltage within an acceptable range when compared to a given reference. An additional objective, is to be complaint with international standards, such as the IEEE 519 [2] and IEC 61000–3–2 [3], regarding the quality of the power being supplied to the load. These objectives can be successfully accomplished by the proper implementation of suitable modulation strategies. In this dissertation, the performance of modulation strategies through analysis of harmonic distortion of voltages and currents is thoroughly assessed in Chapter IV.

Furthermore, it is a fact that photovoltaic technology is a key tool that have enabled a significant increment of electrical power extraction from renewable energy sources. One of the goals of the presented dissertation is to help advance the integration of photovoltaic systems into the distribution grids by tackling technical challenges this technology is facing. Some technical solutions developed in this research could help support the high penetration of photovoltaic systems, while improving efficiency, reliability and power quality of distribution grids. The research presented in Chapter V, spans from PV array modeling, bypass diodes modeling, and an application example of the proposed model comprising a comparative evaluation of several maximum power point tracking algorithms operating in a large grid–connected photovoltaic power plant.

1.2 Objectives

The specific objectives of the research presented in this dissertation are listed in the following:

- To synthesize a branch current controller for a Hexverter–based system able to track DC control signals instead of sinusoidal functions of time.
- To model and propose an appropriate controller to determine active power losses of a Hexverter–based system.

- To investigate and validate the performance of suitable modulation strategies for the multilevel power converter “Hexverter”.
- To investigate how a large–scale PV plant of an arbitrary size can be represented by an equivalent circuital model including both PV cells and bypass diodes.
- To study the heat transfer phenomena of bypass diodes utilized in PV panels in order to estimate its junction temperature.
- To validate the proposed model integrated to a large–scale PV plant affected by partial shading conditions.

CHAPTER 2

AC–AC MODULAR MULTILEVEL CONVERTERS

2.1 Motivation & present state of knowledge

Modular multilevel converters (MMCs) have been during the last years, and will continue to be in the near future, a trending research topic. To better process the electrical power, MMCs can be used where two or three level power converters are used today. This is essentially due to multiple advantages, such as, *(i)* inherent fault tolerance or some times called redundancy: a faulty module can be bypass without affecting the converter operation, *(ii)* application in medium and high power levels, *(iii)* high scalability: the maximum/minimum voltage can be easily modified by increasing/reducing the number of power modules, *(iv)* better quality of output power, and *(v)* comparatively low switching frequency. Conversely, a drawback of these topologies is that proportional to the number of levels, complex challenges appear in the development process of a controller system. As it is well stablished in the literature, modular multilevel converters are a family of power electronic topologies mainly designed for medium and high power levels.

2.2 Technical approach

The fundamental building block of every MMC topology is a single cell. Typically, it comprises an inverter stage, based on half–bridge or full–bridge topology, which is connected to a capacitor "C". In the Hexverter case, full bridge cells are utilized in order to synthesize positive and negative voltage. Cells connected in series create a branch, which in turn is able to generate a multilevel voltage. Branch current controllability is achieved by introducing the connected branch inductor L_b in series. Branch current controller tracks the reference value of the branch current i_b^* by the control of the value of branch voltage v_b^*. In steady state, the average value of the capacitor voltage V_C in every cell in the branch should be stabilized at the same reference value. In MMC topologies, DC–links of the cells are not supplied from external power supplies. It means that voltages of the DC–link capacitors are controlled only by changing the branch current and output voltages of cells in the branch [4].

2.2.1 Modular multilevel converter in back–to–back configuration

The modular multilevel topology is readily available in the market today. It has mainly been proposed for HVDC transmission systems [5]. However, it can be used in a back–to–back configuration shown in Fig. 2.1, to achieve bidirectional electrical power transfer between two different three–phase AC systems and for high–power drive systems in medium–voltage range. An issue of using this topology is the comparatively small output frequency of modern wind generators that may be as low as 10–20 Hz. This small frequency directly leads to require large energy storage requirements in the submodules. The control scheme utilized in this topology can help to mitigate this issue. However, this will require additional circulating current components, hence it directly affects the system's efficiency. The modular multilevel converter features 12 branches and it features a DC link.

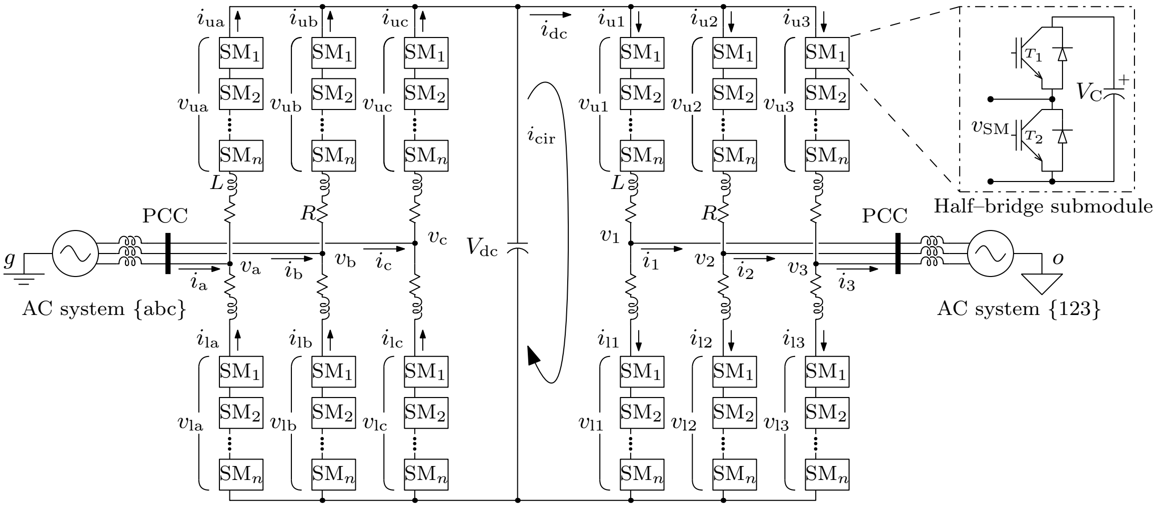

Figure 2.1: Back to back configuration of the modular multilevel converter (MMC).

2.2.2 Modular multilevel Matrix converter

By utilizing a similar technology, the modular multilevel matrix converter has been introduced as an alternative [6]. It is shown in Fig. 2.2. It reduces the number of branches to 9 instead of 12, it does not feature a central DC–link. However, it needs full–bridge submodules that can synthesize both polarities of output voltage. This in turn, doubles the number of switches in comparison to the modular multilevel converter.

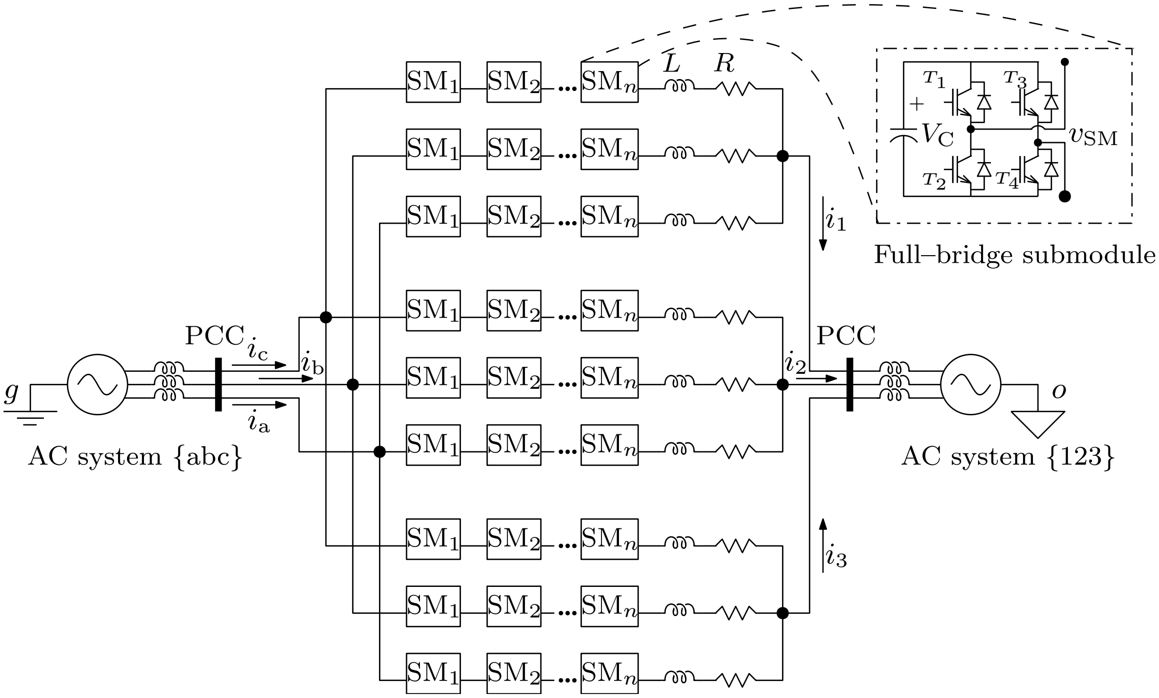

Figure 2.2: Modular multilevel matrix converter (M3C).

2.2.3 Modular multilevel Hexverter

The Hexverter topology is depicted in Fig. 2.3. Typically, the Hexverter is the interphase to connect two different AC three–phase systems operating at two different frequencies, e.g. the supply three–phase grid and an electrical three–phase machine. The Hexverter equivalent circuit is depicted in Fig. 2.4. On the contrary to a back–to–back configuration of AC–DC–AC modular multilevel power converter, shown in Fig. 2.1, the Hexverter has no central DC–link. It further reduces to 6 branches instead of 9 of the modular multilevel matrix converter that is depicted in Fig. 2.2.

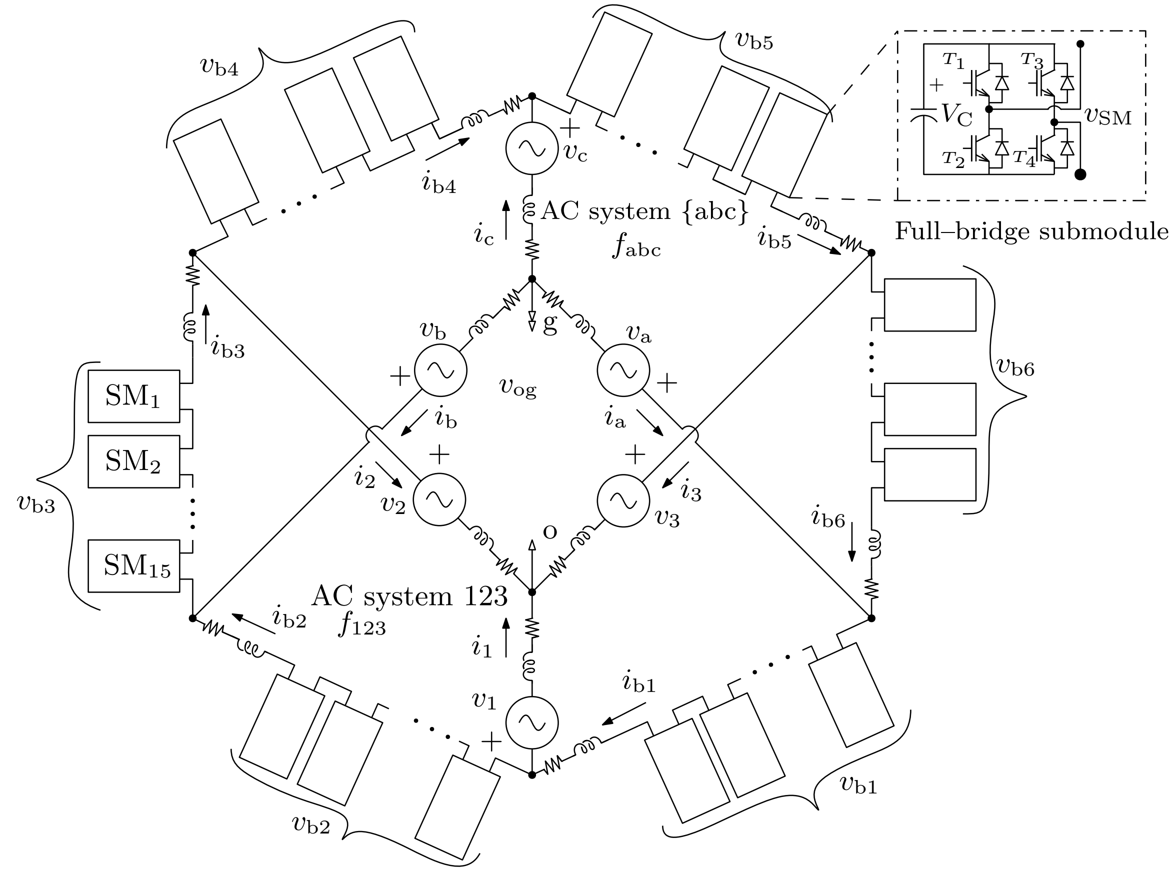

Figure 2.3: AC–AC Hexverter topology.

2.2.3.1 Hexverter principle of operation

Since, this topology require the SMs to synthesize positive and negative voltage. Each of the Hexverter' branches consist of n identical series–connected H–bridge submodules (SM), a branch inductor L_{b} and resistor R_{b}. Each single phase of system {abc} is connected to two phases of system {123} by two branches. Two phases of system {abc} are connected by two branches to a single phase of system {123}. As depicted in Fig. 2.4(a), it is clear that the topology arrangement forms a loop, which in turn allows a circular current i_{cir} to flow.

This current is defined as the circulating current flowing through all branches m, and it is determine by (2.1),

$$i_{\mathrm{cir}} = \frac{1}{6}\sum_{m=1}^{6} i_{\mathrm{bm}}. \tag{2.1}$$

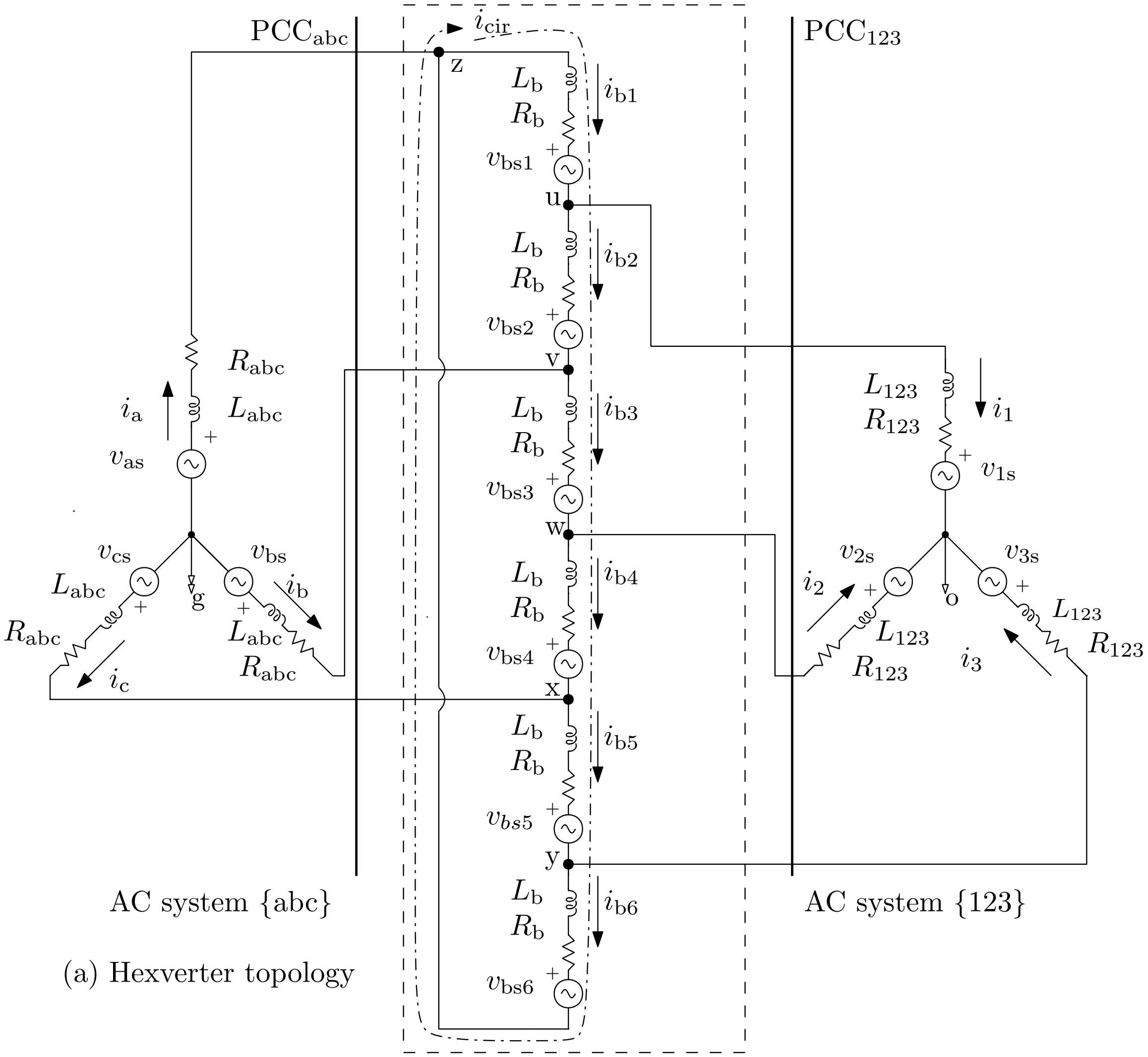

(a) Hexverter topology

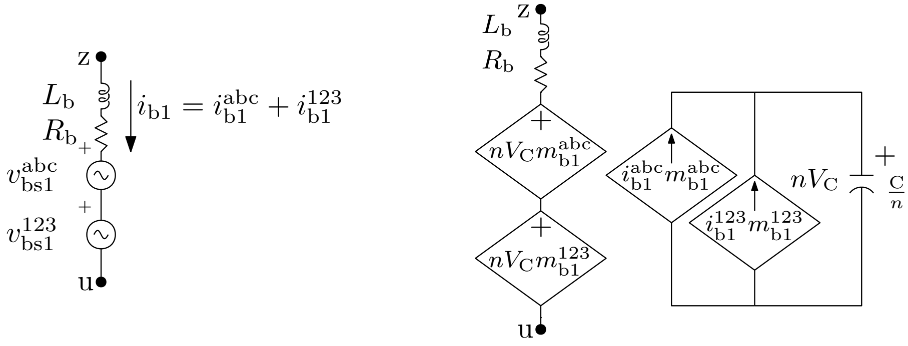

(b) Branch representation f_{abc}, f_{123} (c) Branch average representation

Figure 2.4: AC–AC Hexverter equivalent circuit.

As depicted, in Fig. 2.4, AC phase voltages of Hexverter are not referenced to ground, phase voltages of system {abc} are referenced to phase voltages of system

{123} and viceversa. In addition, a voltage difference v_{og} between both star–point potentials is set. In one hand, considering positive sequence for supply and load of balanced AC three–phase systems respectively, single phase voltages {a} and {1} are fully described by (2.2)–(2.4),

$$v_{\text{a}} = \hat{v}_{\text{abc}}\cos(\omega_{\text{abc}}t), \tag{2.2}$$

$$\hat{v}_{123} = p\hat{v}_{\text{abc}}, \tag{2.3}$$

$$v_1 = \hat{v}_{123}\cos(\omega_{123}t + \theta_{v_{123-\text{abc}}}). \tag{2.4}$$

Voltages of system {123} have a phase difference of $\theta_{v_{123-\text{abc}}}$ at $t = 0$ to system {abc} and p times its voltage magnitude. In the other hand, sinusoidal currents of phases {a} and {1} are characterized by (2.5) and (2.6),

$$i_{\text{a}} = \hat{i}_{\text{abc}}\cos(\omega_{\text{abc}}t - \theta_{i_{\text{abc}}}), \tag{2.5}$$

$$i_1 = \hat{i}_{123}\cos(\omega_{123}t - \theta_{i_{123}} + \theta_{v_{123-\text{abc}}}). \tag{2.6}$$

Taking into account equations (2.1)–(2.6), voltages and currents of branch ($m \in \{1, 2, ..., 6\}$) are characterized by (2.7) and (2.8),

$$\begin{aligned} v_{\text{bs}m} = {} & \hat{v}_{\text{abc}}\cos\Big(\omega_{\text{abc}}t - \frac{m+1+2(-1)^m}{3}\pi\Big) \\ & + \hat{v}_{123}\cos\Big(\omega_{123}t + \theta_{v_{123-\text{abc}}} - \frac{m-2(-1)^m}{3}\pi\Big) \\ & - v_{\text{og}}(-1)^m, \end{aligned} \tag{2.7}$$

$$\begin{aligned} i_{\text{b}m} = {} & \frac{\hat{i}_{\text{abc}}}{\sqrt{3}}\cos\Big(\omega_{\text{abc}}t - \theta_{i_{\text{abc}}} - \frac{2m+2-(-1)^m}{6}\pi\Big) \\ & + \frac{\hat{i}_{123}}{\sqrt{3}}\cos\Big(\omega_{123}t - \theta_{i_{123}} + \theta_{v_{123-\text{abc}}} - \frac{2m+(-1)^m}{6}\pi\Big) \\ & + i_{\text{cir}}. \end{aligned} \tag{2.8}$$

CHAPTER 3

MODELING & CONTROL APPROACH IN THE *DQ* REFERENCE FRAME FOR HEXVERTER–BASED SYSTEMS

3.1 Motivation & present state of knowledge

Modular multilevel converters are a family of power electronic topologies mainly designed for medium and high power levels. Due to their three–phase connection type, these can be classified as either star or delta connection–based [7]. From this family of electronic converters there is a particular topology well suited to intermediate two different three–phase ac systems. It was first proposed back in 2010 [1] and it was named "Hexverter". Control techniques designed for Hexverter–based systems are available in the literature. Considering the so called stationary $\alpha\beta0$ frame, two control schemes were developed in [8] and [9]. The studies presented in [10], [11], [12] and [13], improved the former studies by accomplishing power balance between Hexverter adjacent branches. Alternatively, a control approach developed in the dq reference frame was proposed in [14]. The authors modeled the Hexverter as a double delta full bridge topology. Although this investigation reported acceptable results, semiconductors losses and voltages of branch inductors and resistors were neglected. Additionally, no derivation of power conservation was provided and no experimental validations were presented. Moreover, the Hexverter's dq model was considered as a multiple input multiple output system including inherently complicated coupling effects and time–varying characteristics. Consequently, this generated difficulties into the design of a traditional PI–based control structure. A second control approach considering the dq reference frame was proposed in [15]. The model was developed using the Clark power invariant $\alpha\beta0$ transformation. The authors introduced what they called "double dq transformation" to accomplish decoupling of branch voltages into their respective dq coordinates. Despite the fact this study provided acceptable results, no detailed derivations to represent $\alpha\beta0$ branch currents components were included and no experimental validations were incorporated.

In this chapter, it is proposed a control approach based in [16], along with ideas extracted from state–of–the–art techniques regarding multilevel topologies. The purpose of this chapter is to synthesize a branch current controller in the *dq* reference frame for a Hexverter–based system. It will be assessed by integrating it to a suitable modulation technique, voltage balancing algorithm and a Hexverter–based converter. This chapter is organized as follows. Branch voltages and currents are analyzed in depth in section 3.2.1. Branch current controller is synthesized in section 3.2.4. The Hexverter–based system integration is introduced in Section 3.2.8. Simulation results are laid out in section 3.3. Lastly, conclusions are summarized in Section 3.4.

3.2 Technical approach

3.2.1 Branch voltages and currents analysis

By properly adjusting the six branch voltages, i_{cir} can be controlled either, (*i*) into dynamic operation: to achieve a specific energy adjustment and distribution between all branches, or (*ii*) in steady state operation: by eliminating or suppressing it to its minimum [14]. According to [9], branch power transfer between adjacent branches $\mathrm{P}_{\mathrm{adj}}$, depends on the difference between reactive power of both three–phase systems. It can be controlled using (*i*) or (*ii*) as follows,

- (*i*) using the "adjacent power" compensation approach defined by (3.1),

$$\begin{aligned} \mathrm{P}_{\mathrm{adj}} &= I_{\mathrm{cir}} V_{\mathrm{og}}, \qquad (3.1) \\ \mathrm{P}_{\mathrm{adj}} &= \frac{\sqrt{3}}{18} \left(\mathrm{Q}_{\mathrm{abc}} - \mathrm{Q}_{123} \right) \text{or,} \end{aligned}$$

- (*ii*) setting both reactive powers to the same value.

In this work, it is assumed that the Hexverter system is performing in steady state and both reference reactive power values are set to zero.

3.2.2 Branch voltages

From equations (2.2)–(2.4), branch voltages for branch m ($m \in 1, 2, ..., 6$) can be calculated as follows, [9],

$$\begin{aligned} v_{\mathrm{b}m} = {} & \hat{v}_{\mathrm{abc}}\cos\Big(\omega_{\mathrm{abc}}t - \frac{m+1+2(-1)^m}{3}\pi\Big) \\ & + \hat{v}_{123}\cos\Big(\omega_{123}t + \theta_{v_{123-\mathrm{abc}}} - \frac{m-2(-1)^m}{3}\pi\Big) \\ & - v_{\mathrm{og}}(-1)^m. \end{aligned} \tag{3.2}$$

Based on equation (3.1), $v_{\mathrm{og}} = 0$. Taking into account, unity power factor at $\mathrm{PCC_{abc}}$ and $\mathrm{PCC_{123}}$, and $\theta_{v_{123-\mathrm{abc}}} = -\frac{\pi}{3}$, branch voltage v_{b1} can be calculated as,

$$v_{\mathrm{b1}} = \hat{v}_{\mathrm{abc}}\cos\Big(\omega_{\mathrm{abc}}t\Big) + \hat{v}_{123}\cos\Big(\omega_{123}t + \frac{2}{3}\pi\Big). \tag{3.3}$$

Equation (3.3), indicates that v_{b1} is composed by two phasors rotating at ω_{abc} and ω_{123}. Similar to v_{b1}, all branch voltages can be represented as,

$$\begin{aligned} v_{\mathrm{b1}} &= \hat{v}_{\mathrm{abc}}\cos\Big(\omega_{\mathrm{abc}}t + 0\Big) + \hat{v}_{123}\cos\Big(\omega_{123}t + \frac{2}{3}\pi\Big), \\ v_{\mathrm{b2}} &= \hat{v}_{\mathrm{abc}}\cos\Big(\omega_{\mathrm{abc}}t + \frac{\pi}{3}\Big) + \hat{v}_{123}\cos\Big(\omega_{123}t - \frac{\pi}{3}\Big), \\ v_{\mathrm{b3}} &= \hat{v}_{\mathrm{abc}}\cos\Big(\omega_{\mathrm{abc}}t - \frac{2\pi}{3}\Big) + \hat{v}_{123}\cos\Big(\omega_{123}t + 0\Big), \\ v_{\mathrm{b4}} &= \hat{v}_{\mathrm{abc}}\cos\Big(\omega_{\mathrm{abc}}t - \frac{\pi}{3}\Big) + \hat{v}_{123}\cos\Big(\omega_{123}t - \pi\Big), \\ v_{\mathrm{b5}} &= \hat{v}_{\mathrm{abc}}\cos\Big(\omega_{\mathrm{abc}}t + \frac{2\pi}{3}\Big) + \hat{v}_{123}\cos\Big(\omega_{123}t - \frac{2\pi}{3}\Big), \\ v_{\mathrm{b6}} &= \hat{v}_{\mathrm{abc}}\cos\Big(\omega_{\mathrm{abc}}t - \pi\Big) + \hat{v}_{123}\cos\Big(\omega_{123}t + \frac{\pi}{3}\Big), \\ v_{\mathrm{b}m} &= v_{\mathrm{b}m}^{\mathrm{abc}} + v_{\mathrm{b}m}^{123}. \end{aligned} \tag{3.4}$$

Branch voltages $[v_{\mathrm{b135}}^{\mathrm{abc}}]$, $[v_{\mathrm{b246}}^{\mathrm{abc}}]$, $[v_{\mathrm{b135}}^{123}]$, and $[v_{\mathrm{b246}}^{123}]$ can be grouped, due to the fact that they are $\frac{2\pi}{3}$ radians apart from each other, see Fig. 3.1. As depicted in Fig. 2.4(b), two series–connected controlled voltage sources are an equivalent representation of a branch voltage. Considering a modulation index M = 1, and n number of series–connected SMs, $v_{\mathrm{bs}m}$ can be defined by (3.5), where variables $m_{\mathrm{b}m}^{\mathrm{abc}}$ and $m_{\mathrm{b}m}^{123}$ stand

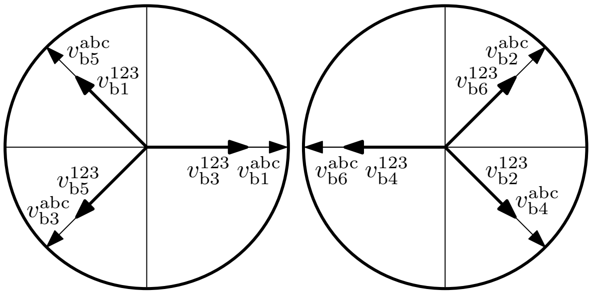

Figure 3.1: Phasor diagram of branch voltages.

for modulation indices calculated at each frequency,

$$v_{\mathrm{bs}m} = nV_{\mathrm{C}}(m_{\mathrm{b}m}^{\mathrm{abc}} + m_{\mathrm{b}m}^{123}). \tag{3.5}$$

3.2.3 Branch currents

From equations (2.5) and (2.6), mathematical derivations for branch currents yields, [9],

$$\begin{aligned} i_{\mathrm{b}m} = {} & \frac{\hat{i}_{\mathrm{abc}}}{\sqrt{3}}\cos\Big(\omega_{\mathrm{abc}}t - \theta_{i_{\mathrm{abc}}} - \frac{2m+2-(-1)^m}{6}\pi\Big), \\ & + \frac{\hat{i}_{123}}{\sqrt{3}}\cos\Big(\omega_{123}t - \theta_{i_{123}} + \theta_{v_{123-\mathrm{abc}}} - \frac{2m+(-1)^m}{6}\pi\Big), \\ & + i_{\mathrm{cir}}. \end{aligned} \tag{3.6}$$

Referencing equation (3.1), $i_{\mathrm{cir}} = 0$. Taking into account, unity power factor at $\mathrm{PCC}_{\mathrm{abc}}$ and PCC_{123}, and $\theta_{v_{123-\mathrm{abc}}} = -\frac{\pi}{3}$, branch current i_{b1} can be calculated as,

$$i_{\mathrm{b1}} = \frac{\hat{i}_{\mathrm{abc}}}{\sqrt{3}}\cos\Big(\omega_{\mathrm{abc}}t - \frac{5\pi}{6}\Big) + \frac{\hat{i}_{123}}{\sqrt{3}}\cos\Big(\omega_{123}t - \frac{3\pi}{6}\Big). \tag{3.7}$$

Equation (3.7), reveals i_{b1} is composed by two phasors rotating at ω_{abc} and ω_{123}. Analogous to i_{b1}, all branch current equations become,

$$\begin{aligned}
i_{\mathrm{b1}} &= \frac{\hat{i}_{\mathrm{abc}}}{\sqrt{3}}\cos\Big(\omega_{\mathrm{abc}}t - \frac{5\pi}{6}\Big) + \frac{\hat{i}_{123}}{\sqrt{3}}\cos\Big(\omega_{123}t - \frac{3\pi}{6}\Big), \\
i_{\mathrm{b2}} &= \frac{\hat{i}_{\mathrm{abc}}}{\sqrt{3}}\cos\Big(\omega_{\mathrm{abc}}t - \frac{5\pi}{6}\Big) + \frac{\hat{i}_{123}}{\sqrt{3}}\cos\Big(\omega_{123}t + \frac{5\pi}{6}\Big), \\
i_{\mathrm{b3}} &= \frac{\hat{i}_{\mathrm{abc}}}{\sqrt{3}}\cos\Big(\omega_{\mathrm{abc}}t - \frac{9\pi}{6}\Big) + \frac{\hat{i}_{123}}{\sqrt{3}}\cos\Big(\omega_{123}t + \frac{5\pi}{6}\Big), \\
i_{\mathrm{b4}} &= \frac{\hat{i}_{\mathrm{abc}}}{\sqrt{3}}\cos\Big(\omega_{\mathrm{abc}}t - \frac{9\pi}{6}\Big) + \frac{\hat{i}_{123}}{\sqrt{3}}\cos\Big(\omega_{123}t + \frac{\pi}{6}\Big), \\
i_{\mathrm{b5}} &= \frac{\hat{i}_{\mathrm{abc}}}{\sqrt{3}}\cos\Big(\omega_{\mathrm{abc}}t - \frac{\pi}{6}\Big) + \frac{\hat{i}_{123}}{\sqrt{3}}\cos\Big(\omega_{123}t + \frac{\pi}{6}\Big), \\
i_{\mathrm{b6}} &= \frac{\hat{i}_{\mathrm{abc}}}{\sqrt{3}}\cos\Big(\omega_{\mathrm{abc}}t - \frac{\pi}{6}\Big) + \frac{\hat{i}_{123}}{\sqrt{3}}\cos\Big(\omega_{123}t - \frac{3\pi}{6}\Big), \\
i_{\mathrm{b}m} &= i_{\mathrm{b}m}^{\mathrm{abc}} + i_{\mathrm{b}m}^{123}.
\end{aligned} \tag{3.8}$$

Taking into account the phasor diagram depicted in Fig. 3.2. Branch currents $[i_{\mathrm{b135}}^{\mathrm{abc}}]$, $[i_{\mathrm{b246}}^{\mathrm{abc}}]$, $[i_{\mathrm{b135}}^{123}]$, and $[i_{\mathrm{b246}}^{123}]$ can be grouped. As illustrated in Fig. 2.4(c), two parallel–connected controlled current sources are an equivalent average branch currents representation. Similar to the branch voltage equation, any of the six branch currents $i_{\mathrm{b}m}$ can be determined by (3.9),

$$i_{\mathrm{b}m} = i_{\mathrm{bm}}^{\mathrm{abc}} m_{\mathrm{b}m}^{\mathrm{abc}} + i_{\mathrm{bm}}^{\mathrm{abc}} m_{\mathrm{b}m}^{123}. \tag{3.9}$$

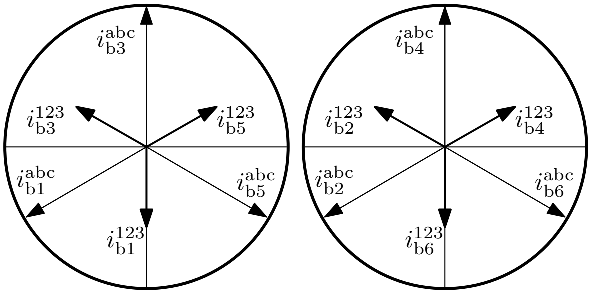

Figure 3.2: Phasor diagram of branch currents.

3.2.4 Synthesized branch current controller in the dq reference frame

3.2.5 Hexverter {abc} side, differential equations

From the circuit characterized in Fig. 2.4, assuming superposition principle can be applied, let us consider only frequency components of the three–phase system {abc}. By doing so, the following set of differential equations are obtained.

State–space equations of system {abc}

$$\begin{aligned}
L_\mathrm{b}\frac{d}{dt}i_\mathrm{b1}^\mathrm{abc} &= v_\mathrm{a} - R_\mathrm{b}i_\mathrm{b1}^\mathrm{abc} - nV_\mathrm{C}m_\mathrm{b1}^\mathrm{abc},\\
L_\mathrm{b}\frac{d}{dt}i_\mathrm{b2}^\mathrm{abc} &= -v_\mathrm{b} - R_\mathrm{b}i_\mathrm{b2}^\mathrm{abc} - nV_\mathrm{C}m_\mathrm{b2}^\mathrm{abc},\\
L_\mathrm{b}\frac{d}{dt}i_\mathrm{b3}^\mathrm{abc} &= v_\mathrm{b} - R_\mathrm{b}i_\mathrm{b3}^\mathrm{abc} - nV_\mathrm{C}m_\mathrm{b3}^\mathrm{abc},\\
L_\mathrm{b}\frac{d}{dt}i_\mathrm{b4}^\mathrm{abc} &= -v_\mathrm{c} - R_\mathrm{b}i_\mathrm{b4}^\mathrm{abc} - nV_\mathrm{C}m_\mathrm{b4}^\mathrm{abc},\\
L_\mathrm{b}\frac{d}{dt}i_\mathrm{b5}^\mathrm{abc} &= v_\mathrm{c} - R_\mathrm{b}i_\mathrm{b5}^\mathrm{abc} - nV_\mathrm{C}m_\mathrm{b5}^\mathrm{abc},\\
L_\mathrm{b}\frac{d}{dt}i_\mathrm{b6}^\mathrm{abc} &= v_\mathrm{a} - R_\mathrm{b}i_\mathrm{b6}^\mathrm{abc} - nV_\mathrm{C}m_\mathrm{b6}^\mathrm{abc}.
\end{aligned} \tag{3.10}$$

Recalling, the cosine–based Park transformation matrix $\mathbf{T}_\mathrm{xyz}^{dq}$ is defined as,

$$\mathbf{T}_\mathrm{xyz}^{dq} = \frac{2}{3}\begin{bmatrix} \cos(\omega_\mathrm{xyz}) & \cos(\omega_\mathrm{xyz} - \frac{2\pi}{3}) & \cos(\omega_\mathrm{xyz} + \frac{2\pi}{3}) \\ -\sin(\omega_\mathrm{xyz}) & -\sin(\omega_\mathrm{xyz} - \frac{2\pi}{3}) & -\sin(\omega_\mathrm{xyz} + \frac{2\pi}{3}) \end{bmatrix}. \tag{3.11}$$

3.2.5.1 From {abc} to dq transformation

By the use of $\mathbf{T}_\mathrm{abc}^{dq}$ transformation matrix, $i_\mathrm{b135}^{\mathrm{abc},dq}$ can be calculated by (3.12),

$$\begin{aligned}
L_\mathrm{b}\frac{d}{dt}i_\mathrm{b135}^\mathrm{abc} &= -R_\mathrm{b}i_\mathrm{b135}^\mathrm{abc} - nV_\mathrm{C}m_\mathrm{b135}^\mathrm{abc} + v_\mathrm{abc},\\
L_\mathrm{b}\mathbf{T}_\mathrm{abc}^{dq}\frac{d}{dt}i_\mathrm{b135}^\mathrm{abc} &= -R_\mathrm{b}\mathbf{T}_\mathrm{abc}^{dq}i_\mathrm{b135}^\mathrm{abc} - nV_\mathrm{C}\mathbf{T}_\mathrm{abc}^{dq}m_\mathrm{b135}^\mathrm{abc} + \mathbf{T}_\mathrm{abc}^{dq}v_\mathrm{abc},\\
\frac{d}{dt}\begin{bmatrix} i_\mathrm{b135}^{\mathrm{abc},d} \\ i_\mathrm{b135}^{\mathrm{abc},q} \end{bmatrix} &= \begin{bmatrix} -\frac{R_\mathrm{b}}{L_\mathrm{b}} & \omega_\mathrm{abc} \\ -\omega_\mathrm{abc} & -\frac{R_\mathrm{b}}{L_\mathrm{b}} \end{bmatrix}\begin{bmatrix} i_\mathrm{b135}^{\mathrm{abc},d} \\ i_\mathrm{b135}^{\mathrm{abc},q} \end{bmatrix} - \frac{nV_\mathrm{C}}{L_\mathrm{b}}\begin{bmatrix} m_\mathrm{b135}^{\mathrm{abc},d} \\ m_\mathrm{b135}^{\mathrm{abc},q} \end{bmatrix} + \frac{1}{L_\mathrm{b}}\begin{bmatrix} v_\mathrm{abc}^{d} \\ v_\mathrm{abc}^{q} \end{bmatrix}.
\end{aligned} \tag{3.12}$$

Correspondingly, $i_{\mathrm{b246}}^{\mathrm{abc},dq}$ can be calculated by (3.13),

$$\begin{aligned}
L_{\mathrm{b}}\frac{d}{dt}i_{\mathrm{b246}}^{\mathrm{abc}} &= -R_{\mathrm{b}}i_{\mathrm{b246}}^{\mathrm{abc}} - nV_{\mathrm{C}}m_{\mathrm{b246}}^{\mathrm{abc}} - v_{\mathrm{bca}}, \qquad (3.13)\\
L_{\mathrm{b}}\mathbf{T}_{\mathrm{abc}}^{dq}\frac{d}{dt}i_{\mathrm{b246}}^{\mathrm{abc}} &= -R_{\mathrm{b}}\mathbf{T}_{\mathrm{abc}}^{dq}i_{\mathrm{b246}}^{\mathrm{abc}} - nV_{\mathrm{C}}\mathbf{T}_{\mathrm{abc}}^{dq}m_{\mathrm{b246}}^{\mathrm{abc}} - \mathbf{T}_{\mathrm{abc}}^{dq}v_{\mathrm{bca}},\\
\frac{d}{dt}\begin{bmatrix} i_{\mathrm{b246}}^{\mathrm{abc},d} \\ i_{\mathrm{b246}}^{\mathrm{abc},q} \end{bmatrix} &= \begin{bmatrix} -\frac{R_{\mathrm{b}}}{L_{\mathrm{b}}} & \omega_{\mathrm{abc}} \\ -\omega_{\mathrm{abc}} & -\frac{R_{\mathrm{b}}}{L_{\mathrm{b}}} \end{bmatrix} \begin{bmatrix} i_{\mathrm{b246}}^{\mathrm{abc},d} \\ i_{\mathrm{b246}}^{\mathrm{abc},q} \end{bmatrix} - \frac{nV_{\mathrm{C}}}{L_{\mathrm{b}}}\begin{bmatrix} m_{\mathrm{b246}}^{\mathrm{abc},d} \\ m_{\mathrm{b246}}^{\mathrm{abc},q} \end{bmatrix} - \frac{1}{L_{\mathrm{b}}}\begin{bmatrix} v_{\mathrm{bca}}^{d} \\ v_{\mathrm{bca}}^{q} \end{bmatrix}.
\end{aligned}$$

3.2.6 Hexverter {123} side, differential equations

Considering only frequency components of three–phase system {123} yields a set of differential equations listed as follows, **State–space equations of system {123}**

$$\begin{aligned}
L_{\mathrm{b}}\frac{d}{dt}i_{\mathrm{b1}}^{123} &= -v_1 - R_{\mathrm{b}}i_{\mathrm{b1}}^{123} - nV_{\mathrm{C}}m_{\mathrm{b1}}^{123}, \qquad (3.14)\\
L_{\mathrm{b}}\frac{d}{dt}i_{\mathrm{b2}}^{123} &= v_1 - R_{\mathrm{b}}i_{\mathrm{b2}}^{123} - nV_{\mathrm{C}}m_{\mathrm{b2}}^{123},\\
L_{\mathrm{b}}\frac{d}{dt}i_{\mathrm{b3}}^{123} &= -v_2 - R_{\mathrm{b}}i_{\mathrm{b3}}^{123} - nV_{\mathrm{C}}m_{\mathrm{b3}}^{123},\\
L_{\mathrm{b}}\frac{d}{dt}i_{\mathrm{b4}}^{123} &= v_2 - R_{\mathrm{b}}i_{\mathrm{b4}}^{123} - nV_{\mathrm{C}}m_{\mathrm{b4}}^{123},\\
L_{\mathrm{b}}\frac{d}{dt}i_{\mathrm{b5}}^{123} &= -v_3 - R_{\mathrm{b}}i_{\mathrm{b5}}^{123} - nV_{\mathrm{C}}m_{\mathrm{b5}}^{123},\\
L_{\mathrm{b}}\frac{d}{dt}i_{\mathrm{b6}}^{123} &= v_3 - R_{\mathrm{b}}i_{\mathrm{b6}}^{123} - nV_{\mathrm{C}}m_{\mathrm{b6}}^{123}.
\end{aligned}$$

3.2.6.1 From {123} to dq transformation

By the use of $\mathbf{T}_{123}^{dq}$ transformation matrix, $i_{\mathrm{b135}}^{123,dq}$ can be calculated by (3.15),

$$\begin{aligned}
L_{\mathrm{b}}\frac{d}{dt}i_{\mathrm{b135}}^{123} &= -R_{\mathrm{b}}i_{\mathrm{b135}}^{123} - nV_{\mathrm{C}}m_{\mathrm{b135}}^{123} - v_{123}, \qquad (3.15)\\
L_{\mathrm{b}}\mathbf{T}_{123}^{dq}\frac{d}{dt}i_{\mathrm{b135}}^{123} &= -R_{\mathrm{b}}\mathbf{T}_{123}^{dq}i_{\mathrm{b135}}^{123} - nV_{\mathrm{C}}\mathbf{T}_{123}^{dq}m_{\mathrm{b135}}^{123} - \mathbf{T}_{123}^{dq}v_{123},\\
\frac{d}{dt}\begin{bmatrix} i_{\mathrm{b135}}^{123,d} \\ i_{\mathrm{b135}}^{123,q} \end{bmatrix} &= \begin{bmatrix} -\frac{R_{\mathrm{b}}}{L_{\mathrm{b}}} & \omega_{123} \\ -\omega_{123} & -\frac{R_{\mathrm{b}}}{L_{\mathrm{b}}} \end{bmatrix} \begin{bmatrix} i_{\mathrm{b135}}^{123,d} \\ i_{\mathrm{b135}}^{123,q} \end{bmatrix} - \frac{nV_{\mathrm{C}}}{L_{\mathrm{b}}}\begin{bmatrix} m_{\mathrm{b135}}^{123,d} \\ m_{\mathrm{b135}}^{123,q} \end{bmatrix} - \frac{1}{L_{\mathrm{b}}}\begin{bmatrix} v_{123}^{d} \\ v_{123}^{q} \end{bmatrix}.
\end{aligned}$$

Moreover, $i_{\mathrm{b}246}^{123,dq}$ can be determined by (3.16),

$$\begin{aligned}
L_{\mathrm{b}}\frac{d}{dt}i_{\mathrm{b}246}^{123} &= -R_{\mathrm{b}}i_{\mathrm{b}246}^{123} - nV_{\mathrm{C}}m_{\mathrm{b}246}^{123} + v_{123}, \qquad (3.16)\\
L_{\mathrm{b}}\mathbf{T}_{123}^{dq}\frac{d}{dt}i_{\mathrm{b}246}^{123} &= -R_{\mathrm{b}}\mathbf{T}_{123}^{dq}i_{\mathrm{b}246}^{123} - nV_{\mathrm{C}}\mathbf{T}_{123}^{dq}m_{\mathrm{b}246}^{123} + \mathbf{T}_{123}^{dq}v_{123},\\
\frac{d}{dt}\begin{bmatrix} i_{\mathrm{b}246}^{123,d} \\ i_{\mathrm{b}246}^{123,q} \end{bmatrix} &= \begin{bmatrix} -\frac{R_{\mathrm{b}}}{L_{\mathrm{b}}} & \omega_{123} \\ -\omega_{123} & -\frac{R_{\mathrm{b}}}{L_{\mathrm{b}}} \end{bmatrix}\begin{bmatrix} i_{\mathrm{b}246}^{123,d} \\ i_{\mathrm{b}246}^{123,q} \end{bmatrix} - \frac{nV_{\mathrm{C}}}{L_{\mathrm{b}}}\begin{bmatrix} m_{\mathrm{b}246}^{123,d} \\ m_{\mathrm{b}246}^{123,q} \end{bmatrix} + \frac{1}{L_{\mathrm{b}}}\begin{bmatrix} v_{123}^{d} \\ v_{123}^{q} \end{bmatrix}.
\end{aligned}$$

3.2.7 Control approach

From (3.12), the following differential equations can be obtained,

$$\frac{d}{dt}i_{\mathrm{b}135}^{\mathrm{abc},d} = -\frac{R_{\mathrm{b}}}{L_{\mathrm{b}}}i_{\mathrm{b}135}^{\mathrm{abc},d} + \omega_{\mathrm{abc}}i_{\mathrm{b}135}^{\mathrm{abc},q} - \frac{nV_{\mathrm{C}}}{L_{\mathrm{b}}}m_{\mathrm{b}135}^{\mathrm{abc},d} + \frac{1}{L_{\mathrm{b}}}v_{\mathrm{abc}}^{d}, \qquad (3.17)$$

$$\frac{d}{dt}i_{\mathrm{b}135}^{\mathrm{abc},q} = -\omega_{\mathrm{abc}}i_{\mathrm{b}135}^{\mathrm{abc},d} - \frac{R_{\mathrm{b}}}{L_{\mathrm{b}}}i_{\mathrm{b}135}^{\mathrm{abc},q} - \frac{nV_{\mathrm{C}}}{L_{\mathrm{b}}}m_{\mathrm{b}135}^{\mathrm{abc},q} + \frac{1}{L_{\mathrm{b}}}v_{\mathrm{abc}}^{q}, \qquad (3.18)$$

considering a change of variable as,

$$m_{\mathrm{b}135}^{\mathrm{abc},d} = \frac{1}{nV_{\mathrm{C}}}\left(-u_{135}^{\mathrm{abc},d} + L_{\mathrm{b}}\omega_{\mathrm{abc}}i_{\mathrm{b}135}^{\mathrm{abc},q} + v_{\mathrm{abc}}^{d}\right), \qquad (3.19)$$

$$m_{\mathrm{b}135}^{\mathrm{abc},q} = \frac{1}{nV_{\mathrm{C}}}\left(-u_{135}^{\mathrm{abc},q} - L_{\mathrm{b}}\omega_{\mathrm{abc}}i_{\mathrm{b}135}^{\mathrm{abc},d} + v_{\mathrm{abc}}^{q}\right), \qquad (3.20)$$

two decoupled equations that can be independently controlled, standing for dq components of branch currents [135] at frequency {abc}, are indicated in (3.21),

$$\begin{aligned}
\frac{d}{dt}i_{\mathrm{b}135}^{\mathrm{abc},d} &= -\frac{R_{\mathrm{b}}}{L_{\mathrm{b}}}i_{\mathrm{b}135}^{\mathrm{abc},d} + \frac{1}{L_{\mathrm{b}}}u_{135}^{\mathrm{abc},d}, \qquad (3.21)\\
\frac{d}{dt}i_{\mathrm{b}135}^{\mathrm{abc},q} &= -\frac{R_{\mathrm{b}}}{L_{\mathrm{b}}}i_{\mathrm{b}135}^{\mathrm{abc},q} + \frac{1}{L_{\mathrm{b}}}u_{135}^{\mathrm{abc},q}.
\end{aligned}$$

Hence, from equations (3.13), (3.15) and (3.16), following a similar procedure, equations (3.22) to (3.24) can be derived,

$$\begin{aligned}
\frac{d}{dt} i_{\mathrm{b246}}^{\mathrm{abc},d} &= -\frac{R_{\mathrm{b}}}{L_{\mathrm{b}}} i_{\mathrm{b246}}^{\mathrm{abc},d} + \frac{1}{L_{\mathrm{b}}} u_{246}^{\mathrm{abc},d}, && (3.22)\\
\frac{d}{dt} i_{\mathrm{b246}}^{\mathrm{abc},q} &= -\frac{R_{\mathrm{b}}}{L_{\mathrm{b}}} i_{\mathrm{b246}}^{\mathrm{abc},q} + \frac{1}{L_{\mathrm{b}}} u_{246}^{\mathrm{abc},q};\\
\frac{d}{dt} i_{\mathrm{b135}}^{123,d} &= -\frac{R_{\mathrm{b}}}{L_{\mathrm{b}}} i_{\mathrm{b135}}^{123,d} + \frac{1}{L_{\mathrm{b}}} u_{135}^{123,d}, && (3.23)\\
\frac{d}{dt} i_{\mathrm{b135}}^{123,q} &= -\frac{R_{\mathrm{b}}}{L_{\mathrm{b}}} i_{\mathrm{b135}}^{123,q} + \frac{1}{L_{\mathrm{b}}} u_{135}^{123,q};\\
\frac{d}{dt} i_{\mathrm{b246}}^{123,d} &= -\frac{R_{\mathrm{b}}}{L_{\mathrm{b}}} i_{\mathrm{b246}}^{123,d} + \frac{1}{L_{\mathrm{b}}} u_{246}^{123,d}, && (3.24)\\
\frac{d}{dt} i_{\mathrm{b246}}^{123,q} &= -\frac{R_{\mathrm{b}}}{L_{\mathrm{b}}} i_{\mathrm{b246}}^{123,q} + \frac{1}{L_{\mathrm{b}}} u_{246}^{123,q}.
\end{aligned}$$

These equations are an equivalent representation of the former set of differential equations, which in turn can be easily transformed into the Laplace domain. Following the procedure from [16], by the use of PI regulators, a suitable control scheme in the dq reference frame for a Hexverter–based system can be implemented.

3.2.8 Hexverter–based system integration

The framework of the Hexverter–based system integration is depicted in Fig. 3.3. Branch current controllers, modulator, voltage balancing algorithm and Hexverter multilevel converter can be readily identified. $\mathbf{x} = [i_{\mathrm{b135}}^{\mathrm{abc},dq}, i_{\mathrm{b246}}^{\mathrm{abc},dq}, i_{\mathrm{b135}}^{123,dq}, i_{\mathrm{b246}}^{123,dq}]'$ is a column vector representing the state variables. For instance, $i_{\mathrm{b135}}^{\mathrm{abc},dq}$ indicates dq current components of branches [135] at a unique frequency $\{\mathrm{abc}\}$. The same applies for the remaining state variables. Each branch current controller outputs a three–phase modulating signal labeled as $m_{\mathrm{b135}}^{\mathrm{abc}}$, $m_{\mathrm{b246}}^{\mathrm{abc}}$, m_{b135}^{123} and m_{b246}^{123}. These signals are then split and recombined as follows, $m_{\mathrm{b1}} = m_{\mathrm{b1}}^{\mathrm{abc}} + m_{\mathrm{b1}}^{123}, m_{\mathrm{b2}} = m_{\mathrm{b2}}^{\mathrm{abc}} + m_{\mathrm{b2}}^{123}, ..., m_{\mathrm{b6}} = m_{\mathrm{b6}}^{\mathrm{abc}} + m_{\mathrm{b6}}^{123}$. Subsequently, these signals are multiplied by the reference branch voltage nV_{C}^{*}, obtaining reference branch voltages $v_{\mathrm{bs}m}^{*}$, which are then fed into the modulator. In this work, nearest level control modulation technique and voltage balancing algorithm are implemented according to [17].

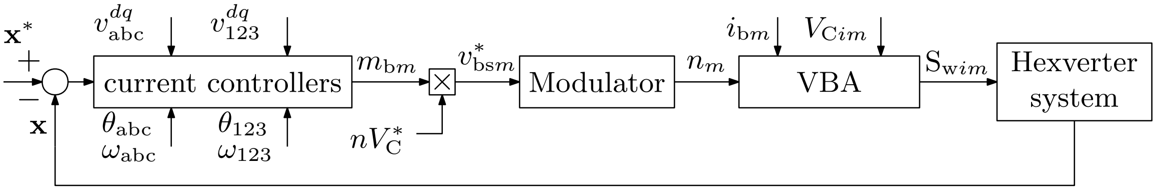

Figure 3.3: Hexverter–based system integration.

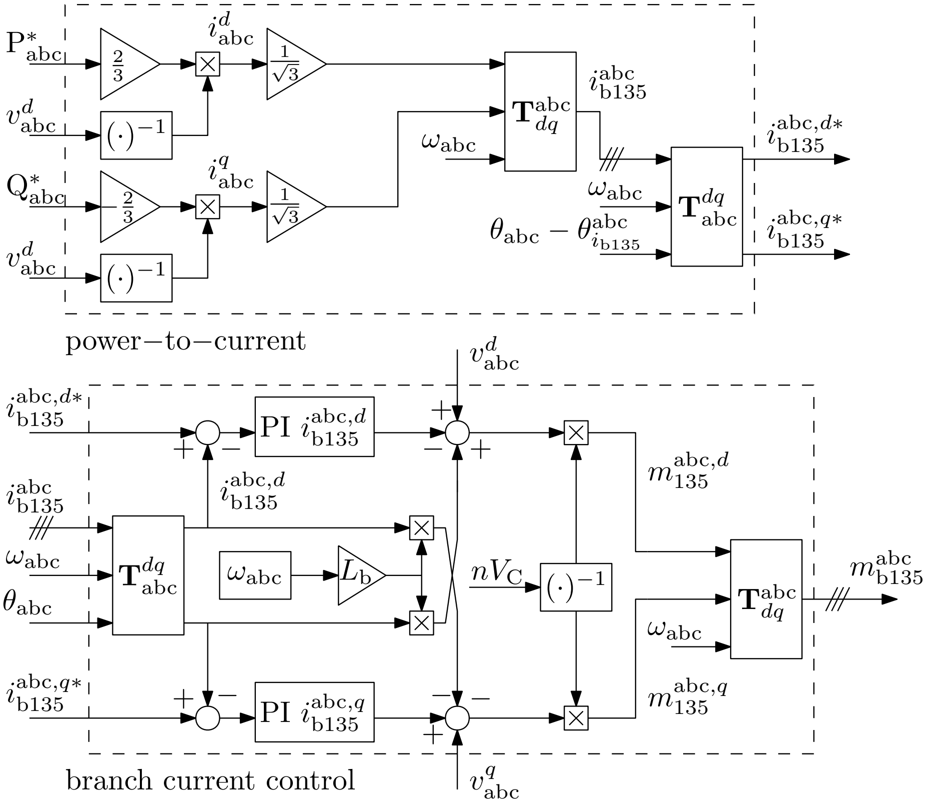

Figure 3.4: Blocks diagram for $i_{\mathrm{b135}}^{\mathrm{abc}}$ current control.

3.2.9 Branch current controllers

A block diagram of branch current controller corresponding to the state variable [$i_{\mathrm{b135}}^{\mathrm{abc},dq}$], is described by Fig. 3.4. It consists of two main subsystems labeled as “power–to–current” and “branch current control”. Reference branch currents are compared with its measurements in the dq reference frame. Then, its corresponding errors are driven to zero through decoupled PI compensators. Similar schematics can be drawn for branch current controllers of state variables $i_{\mathrm{b246}}^{\mathrm{abc},dq}$, $i_{\mathrm{b135}}^{123,dq}$ and $i_{\mathrm{b246}}^{123,dq}$. In total, eight single input single output (SISO) branch current controllers, indicated by equations (3.21)–(3.24) are designed.

3.2.10 Modulator and voltage balancing algorithm

The Hexverter's efficiency (η) analysis was performed in [9]. Depending on operational conditions, η might vary between a range of $93-97\%$. In this work, $\eta = 93.33\%$ can be approximated by (3.25):

$$\mathrm{S}_{123} = \mathrm{S}_{\mathrm{abc}} - \sum_{m=1}^{6} |i_{\mathrm{b}m}|^2 R_{\mathrm{b}}, \quad \eta = \frac{\mathrm{S}_{123}}{\mathrm{S}_{\mathrm{abc}}} \times 100. \tag{3.25}$$

3.3 Simulation results

To validate the performance of the synthesized current control a detailed computer simulation in PSCAD/EMTDC of a Hexverter–based system was implemented. Active power $\mathrm{P}_{\mathrm{abc}}$ as well as reactive power $\mathrm{Q}_{\mathrm{abc}}$ and Q_{123} were considered known. Conversely, active power P_{123} was calculated using equation (3.25). Using simulation parameters listed on table 3.1, $i_{\mathrm{b135}}^{\mathrm{abc},d*}$ and $i_{\mathrm{b135}}^{\mathrm{abc},q*}$ can be calculated as,

$$\begin{aligned} i_{\mathrm{b135}}^{\mathrm{abc},d*} &= \frac{2}{3}\frac{\mathrm{P}_{\mathrm{abc}}}{v_{\mathrm{abc}}^{d}\sqrt{3}}\cos(\frac{\pi}{6}) = 5.0 \text{ A},\\ i_{\mathrm{b135}}^{\mathrm{abc},q*} &= \frac{2}{3}\frac{\mathrm{P}_{\mathrm{abc}}}{v_{\mathrm{abc}}^{d}\sqrt{3}}\sin(\frac{\pi}{6}) = 2.88 \text{ A}, \end{aligned}$$

in the same fashion $i_{\mathrm{b135}}^{123,d*}$ and $i_{\mathrm{b135}}^{123,q*}$ are determined as,

$$\begin{aligned} i_{\mathrm{b135}}^{123,d*} &= \frac{2}{3}\frac{\mathrm{P}_{123}}{v_{123}^{d}\sqrt{3}}\cos(-\frac{\pi}{6}) = 7.78 \text{ A},\\ i_{\mathrm{b135}}^{123,q*} &= \frac{2}{3}\frac{\mathrm{P}_{123}}{v_{123}^{d}\sqrt{3}}\sin(-\frac{\pi}{6}) = -4.49 \text{ A}. \end{aligned}$$

Table 3.1: Simulation parameters

Hexverter	Branch resistance	R_{b}	1.2 Ω
	Branch inductance	L_{b}	30 mH
	SMs per branch	n	12
	SM capacitance	C	20 mF
	Nominal SM voltage	V_{C}	133.33 V
System {abc}	Active power	$\mathrm{P}_{\mathrm{abc}}$	15 kVA
	Reactive power	$\mathrm{Q}_{\mathrm{abc}}$	0 kVar
	Peak voltage	$\hat{v}_{\mathrm{abc}}$	1 kV
	Frequency/phase	$f_{\mathrm{abc}}/\theta_{\mathrm{abc}}$	50 Hz/0 rad
	Resistance/Inductance	$R_{\mathrm{abc}}/L_{\mathrm{abc}}$	1.0 Ω/10 mH
System {123}	Active power	P_{123}	15 kVA×η
	Reactive power	Q_{123}	0 kVar
	Peak voltage	$\hat{v}_{123}$	600 V
	Frequency/phase	f_{123}/θ_{123}	10 Hz/0 rad
	Resistance/Inductance	R_{123}/L_{123}	0.8 Ω/15 mH

3.3.1 Performance assessment of the proposed control scheme

The overall performance of the proposed control scheme, when integrated to a suitable modulation strategy, voltage balancing algorithm and the Hexverter–based system, is illustrated by representative waveforms. As depicted in Fig. 3.5, power transfer is achieved according to the given references. Similarly, reference values of branch currents $i_{\mathrm{b135}}^{\mathrm{abc},dq*}$ and $i_{\mathrm{b135}}^{123,dq*}$, can be readily compared in Fig. 3.6. Modulation indices of group [135] are depicted in Fig. 3.7. Proper frequency and magnitude can be observed. Moreover, measurements of synthesized three–phase voltages and

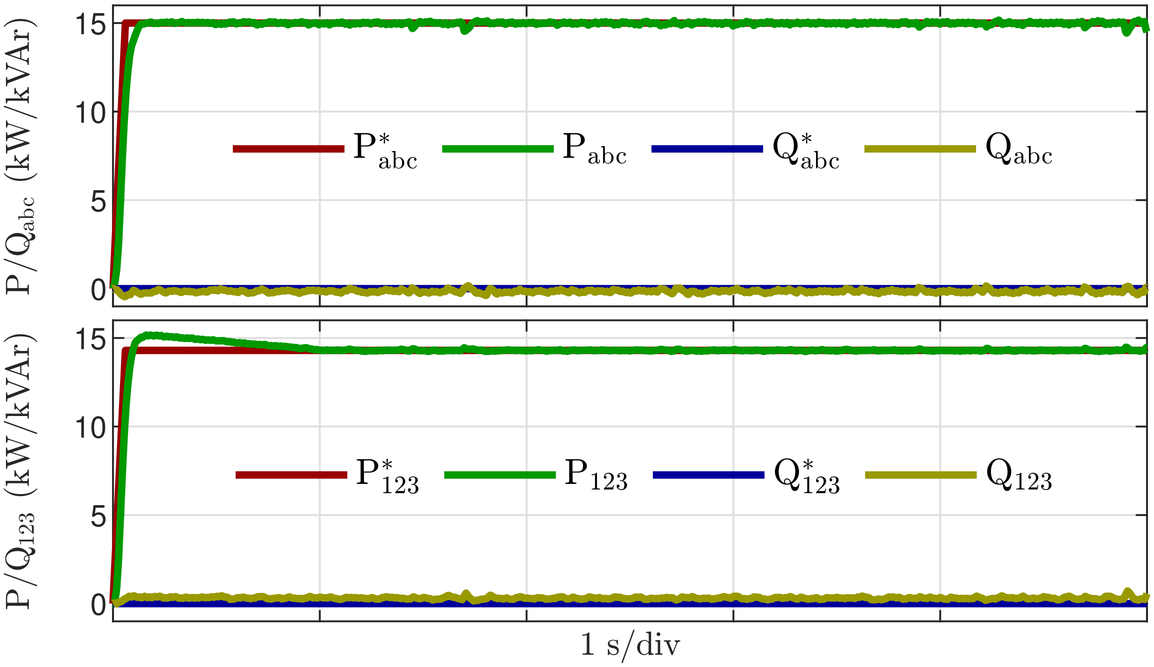

Figure 3.5: Three–phase powers P/Q^*_{abc} and P/Q^*_{123} vs filtered measurements.

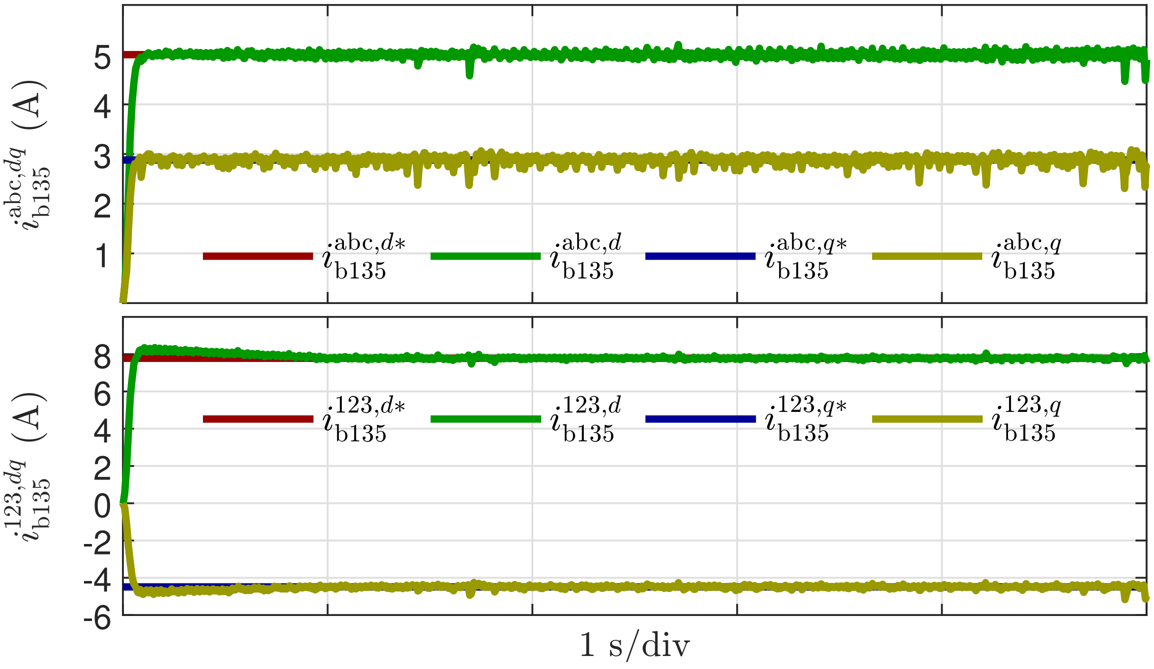

Figure 3.6: Branch currents $i^{\text{abc},dq*}_{\text{b135}}$ and $i^{123,dq*}_{\text{b135}}$ vs filtered measurements.

currents are illustrated in Fig. 3.8. Although, these waveforms feature a small ripple, its magnitude, phase and frequencies are correct. In addition, measurements of synthesized branch voltage v_{b1} and branch current i_{b1} are shown in Fig. 3.9. As

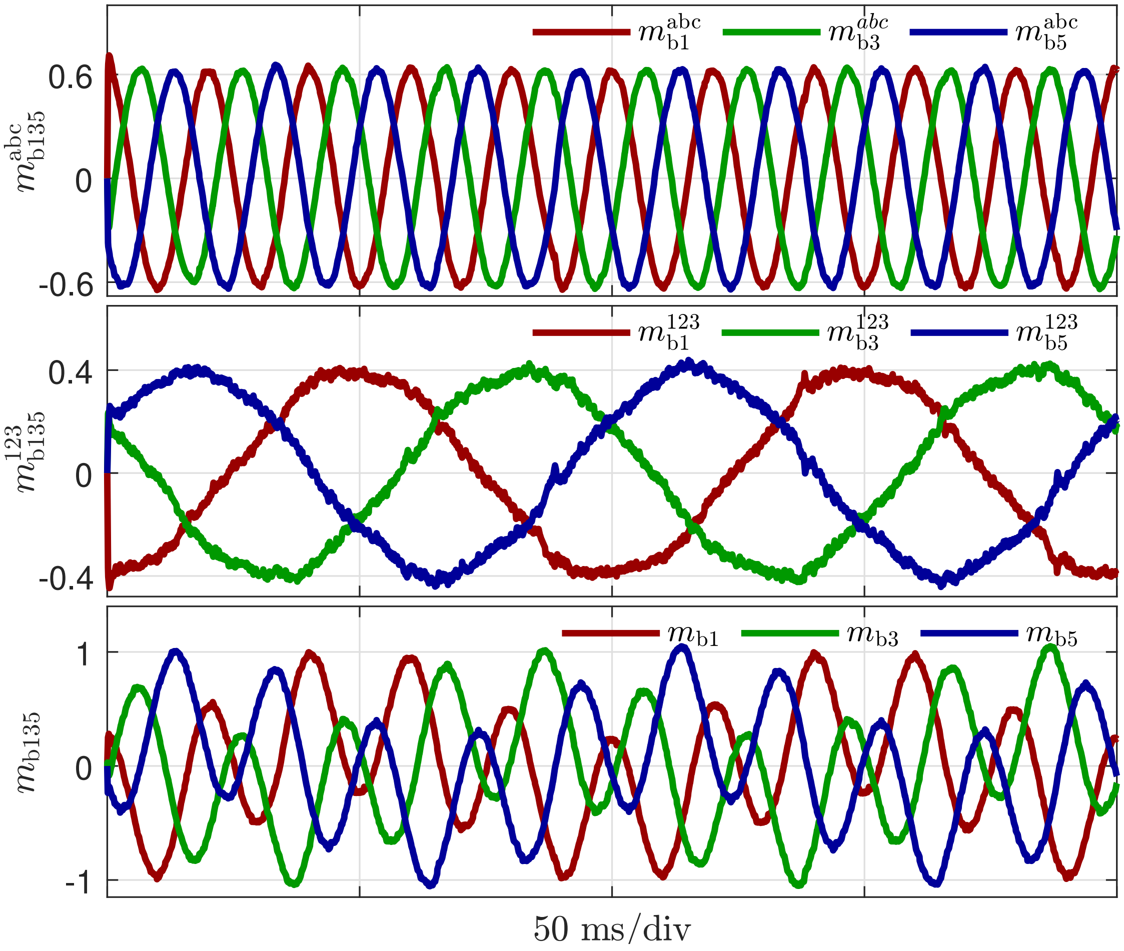

Figure 3.7: Modulation indices calculated for branches [135].

expected, both waveforms contain frequency components (f_{abc}, f_{123}) of the two ac systems. Lastly, performance of a voltage balancing algorithm is included in Fig. 3.10, where n number of controlled capacitor voltage waveforms are shown. In comparison to the given SM capacitor voltage V_C^*, a voltage difference of approximately ± 1 V represents 1.5% error.

3.4 Conclusions

In this chapter, a control scheme in the dq reference frame for a Hexverter–based system was synthesized. Its performance was validated when integrated to a suitable modulation strategy and a voltage balancing algorithm via a detailed PSCAD/EMTDC computer simulation. Representative waveforms featuring proper

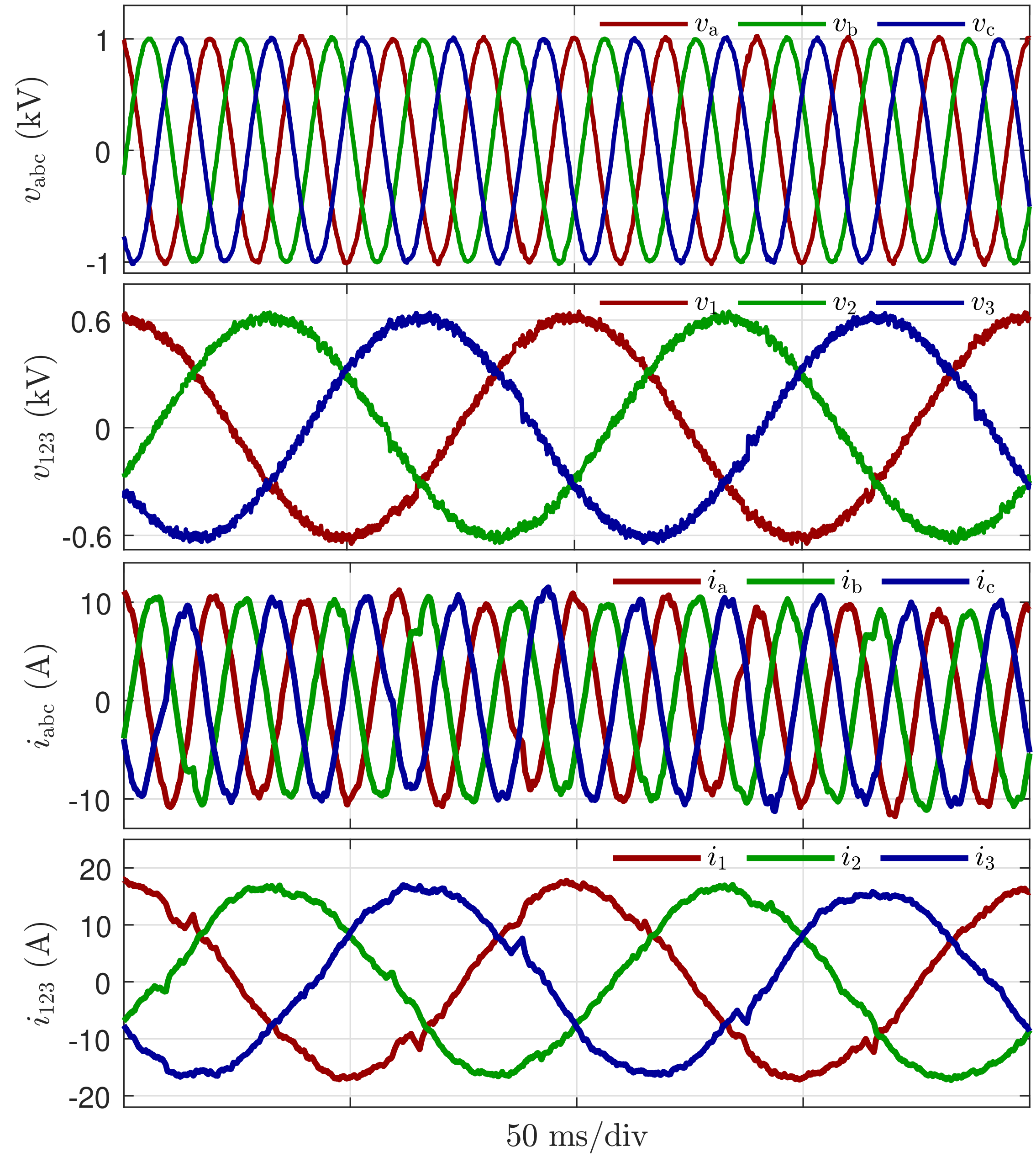

Figure 3.8: Synthesized three–phase voltages and currents.

phase, magnitude and frequency components validate the effectiveness of the characterized system.

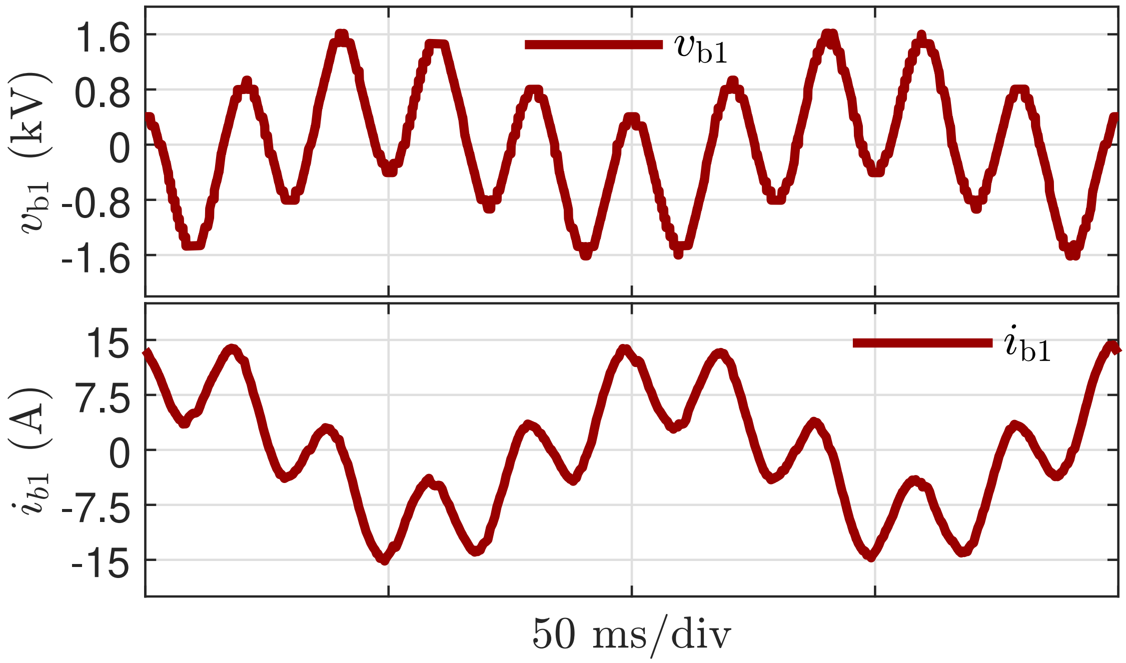

Figure 3.9: Synthesized branch voltage v_{b1} and branch current i_{b1}.

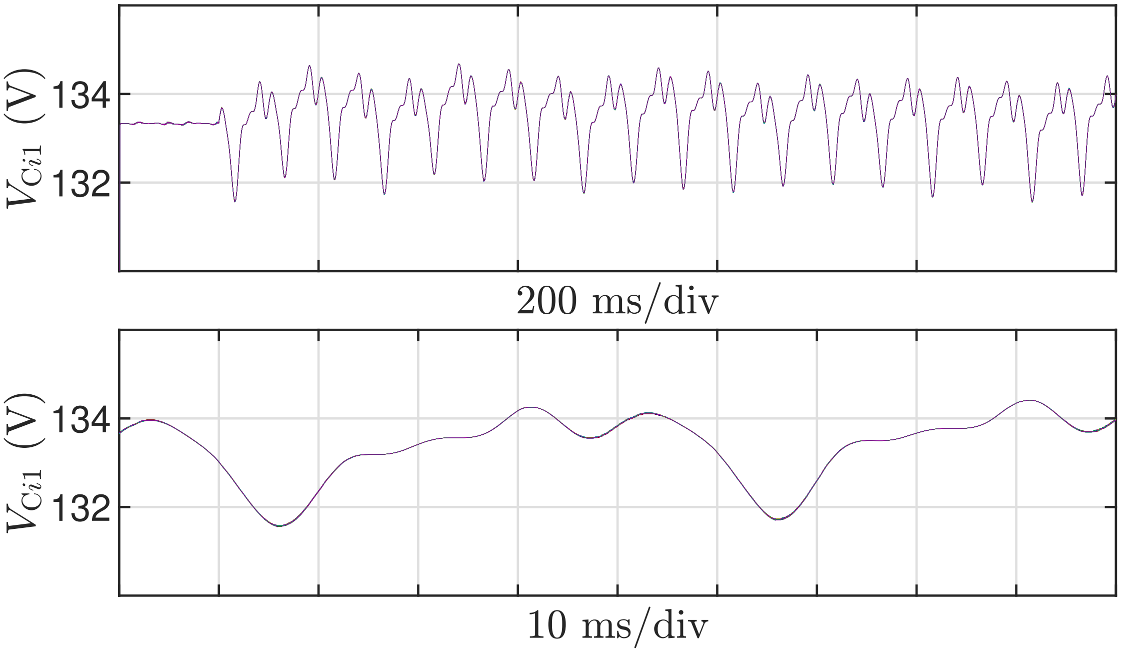

Figure 3.10: NLC VBA performance.

CHAPTER 4

DETAILED ASSESSMENT OF MODULATION STRATEGIES FOR HEXVERTER–BASED MODULAR MULTILEVEL CONVERTERS

4.1 Motivation & present state of knowledge

Among the multilevel topologies available in the literature, there is one multilevel topology suitable to connect two different three phase AC systems. In particular when these AC systems run at two different frequencies. It is called Hexverter and it was firstly introduced in 2010 [1]. Since then, a number of control approaches, including its current control in the so call $\alpha, \beta, 0$ frame was reported in [18], [9], [14], [10]. Moreover, an improved Hexverter topology with magnetically coupled branch inductors was investigated in [19]. Furthermore, a full branch energy adjustment concept was investigated in [11]. This proposal was assessed in detail controlling an electrical machine running at low frequencies [20]. In addition, a different strategy to control branch energy balance between branches was reported in [21]. A Hexverter–based power flow controller was studied in [22]. Regarding the matrix converter, it is categorized as a direct AC–AC modular multilevel converter featuring nine multilevel branches. It is more suitable for low–speed high–power applications. However, this converter has an inherent issue when this device performs close to the grid frequency [12]. Since the Hexverter requires only six multilevel branches when functioning, a matrix converter was put to work as a Hexverter considering defective conditions in [23]. In order to manage the task of transferring power from source to load, all kind of power multilevel converters share a common need, that is, n number of submodules (SMs) to be connected at any given time must be accurately calculated. At the same time, the power quality injected to a load must be compliant with international standards including, but not limited to, the IEEE 519 [2] and IEC61000–3–2 [3]. Despite the fact that some modulation techniques such as: nearest level control (NLC) and phase disposition–sinusoidal pulse width modulation (PD–SPWM) have been implemented and investigated for some multilevel topologies there is still room to investigate and present a detailed assessment of modulation strategies when these are implemented for the direct AC–AC modular multilevel topology called in short "Hexverter". Expanding the research results presented in [17], and based on the discussion above, the main contributions of this chapter are:

- Hexverter modeling and control in a unified two–frequency *dq* framework
- Proposal and evaluation of a "virtual V_C^2 controller" to dynamically account for Hexverter's active power losses allowing to achieve active power balance on the fly
- Detailed assessment of modulation strategies through total harmonic distortion of synthesized voltages and currents

This chapter is organized as follows. The modeling and control approach in a unified two–frequency *dq* framework is described in depth in Section 4.2.1. Modulation strategies NLC and PD–SPWM are thoroughly described in Section 4.2.2. The proposed "virtual V_C^2 controller" is presented and derived in Section 4.2.3. Integration of the Hexverter–based system is shown in section 4.2.4. Simulation results of synthesized voltages, currents and performance of the voltage balancing algorithms are discussed in Section 4.3. Similarly, active power losses obtained by the "virtual V_C^2 controller" are discussed in section 4.3.4. In addition, a detailed assessment of spectrum and harmonic content of synthesized voltages and currents is thoroughly presented in Section 4.3.7. Finally, conclusions are summarized in Section 4.4.

4.2 Technical approach

4.2.1 Modeling and control approach in a unified two–frequency *dq* framework

From (3.12), the next differential equations are obtained,

$$\frac{d}{dt} i_{\mathrm{b135}}^{\mathrm{abc},d} = -\frac{R_{\mathrm{b}}}{L_{\mathrm{b}}} i_{\mathrm{b135}}^{\mathrm{abc},d} + \omega_{\mathrm{abc}} i_{\mathrm{b135}}^{\mathrm{abc},q} - \frac{nV_{\mathrm{C}}}{L_{\mathrm{b}}} m_{\mathrm{b135}}^{\mathrm{abc},d} + \frac{1}{L_{\mathrm{b}}} v_{\mathrm{abc}}^{d}, \tag{4.1}$$

$$\frac{d}{dt} i_{\mathrm{b135}}^{\mathrm{abc},q} = -\omega_{\mathrm{abc}} i_{\mathrm{b135}}^{\mathrm{abc},d} - \frac{R_{\mathrm{b}}}{L_{\mathrm{b}}} i_{\mathrm{b135}}^{\mathrm{abc},q} - \frac{nV_{\mathrm{C}}}{L_{\mathrm{b}}} m_{\mathrm{b135}}^{\mathrm{abc},q} + \frac{1}{L_{\mathrm{b}}} v_{\mathrm{abc}}^{q}, \tag{4.2}$$

making use of a change of variable as,

$$m_{\mathrm{b135}}^{\mathrm{abc},d} = \frac{1}{nV_{\mathrm{C}}} \left(-u_{135}^{\mathrm{abc},d} + L_{\mathrm{b}} \omega_{\mathrm{abc}} i_{\mathrm{b135}}^{\mathrm{abc},q} + v_{\mathrm{abc}}^{d} \right), \tag{4.3}$$

$$m_{\mathrm{b135}}^{\mathrm{abc},q} = \frac{1}{nV_{\mathrm{C}}} \left(-u_{135}^{\mathrm{abc},q} - L_{\mathrm{b}} \omega_{\mathrm{abc}} i_{\mathrm{b135}}^{\mathrm{abc},d} + v_{\mathrm{abc}}^{q} \right), \tag{4.4}$$

two independent and decoupled equations are obtained, which stand for dq components of branch currents $\{135\}$ at frequency $\{\mathrm{abc}\}$, those are described by (4.5),

$$\begin{aligned} \frac{d}{dt} i_{\mathrm{b135}}^{\mathrm{abc},d} &= -\frac{R_{\mathrm{b}}}{L_{\mathrm{b}}} i_{\mathrm{b135}}^{\mathrm{abc},d} + \frac{1}{L_{\mathrm{b}}} u_{135}^{\mathrm{abc},d}, \\ \frac{d}{dt} i_{\mathrm{b135}}^{\mathrm{abc},q} &= -\frac{R_{\mathrm{b}}}{L_{\mathrm{b}}} i_{\mathrm{b135}}^{\mathrm{abc},q} + \frac{1}{L_{\mathrm{b}}} u_{135}^{\mathrm{abc},q}. \end{aligned} \tag{4.5}$$

Similar mathematical manipulations can be done with equations (3.13), (3.15) and (3.16), in order to obtain decoupled equations to control branch currents $\{i_{\mathrm{b246}}^{\mathrm{abc},d}\}$,$\{i_{\mathrm{b246}}^{\mathrm{abc},q}\}$, $\{i_{\mathrm{b135}}^{123,d}\}$,$\{i_{\mathrm{b135}}^{123,q}\}$, $\{i_{\mathrm{b246}}^{123,d}\}$ and $\{i_{\mathrm{b246}}^{123,q}\}$. This set of equations is an equivalent and decoupled representation of the former set of differential equations that can be managed and transformed into the Laplace domain. Afterwards, by applying techniques from [16], a suitable control scheme in a unified two–frequency dq framework for a Hexverter–based system is elaborated.

4.2.1.1 Branch current controllers

Variable $\mathbf{x} = [i_{\mathrm{b135}}^{\mathrm{abc},dq}, i_{\mathrm{b246}}^{\mathrm{abc},dq}, i_{\mathrm{b135}}^{123,dq}, i_{\mathrm{b246}}^{123,dq}]'$ corresponds to a column vector that includes the state variables. From it, $i_{\mathrm{b135}}^{\mathrm{abc},dq}$ indicates dq components of currents flowing through branches $\{135\}$ at frequency $\{\mathrm{abc}\}$. Same notation applies for the rest of state variables. Each branch current controller outputs a three–phase modulating signal

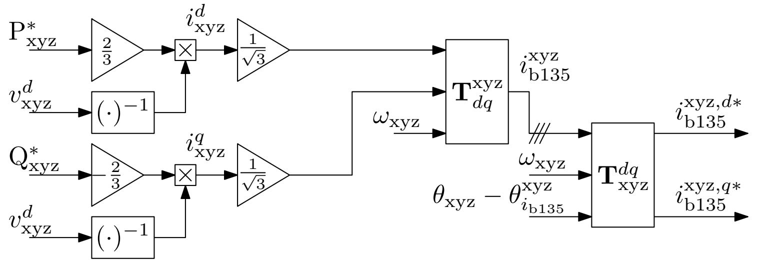

(a) power−to−current

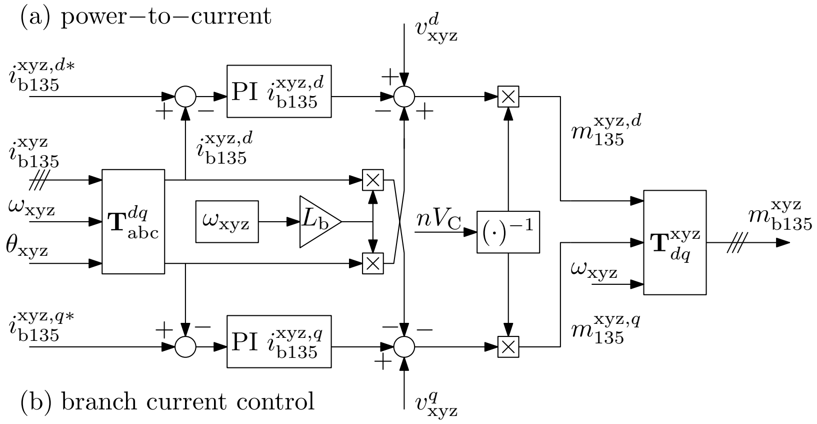

(b) branch current control

Figure 4.1: Block diagrams of current control to determine m^{xyz}_{b135}.

labeled as m^{abc}_{b135}, m^{abc}_{b246}, m^{123}_{b135} and m^{123}_{b246}. These signals are then de–multiplexed and recombined as follows, $m_{b1} = m^{abc}_{b1} + m^{123}_{b1}, m_{b2} = m^{abc}_{b2} + m^{123}_{b2}, ..., m_{b6} = m^{abc}_{b6} + m^{123}_{b6}$. Afterwards, these signals are augmented by the reference branch voltage nV^*_C, generating reference branch voltages v^*_{bsm}, which suitable inputs for the modulator. A general schematic of a single branch current controller is depicted in Fig. 4.1. From it, {xyz} stands for frequency {abc} or {123}, respectively. Figure 4.1 shows two main subsystems marked as "power–to–current" and "branch current control". As depicted branch current' error is driven to zero through a decoupled PI compensator. For instance, if {xyz} is replaced by {abc} then the schematic agrees with the state variable $[i^{abc,dq}_{b135}]$, and as a consequence, the modulation index m^{abc}_{b135} is the output of the subsystem "branch current control". Analogous diagrams of branch current controllers corresponding to state variables $i^{abc,dq}_{b246}$, $i^{123,dq}_{b135}$ and $i^{123,dq}_{b246}$ can be elaborated [24].

4.2.2 Modulation strategies

This section is devoted to describe in depth two modulation techniques that will further be assessed when implemented into the Hexverter–based system.

4.2.2.1 Nearest level control modulation

Some of the features that makes NLC an attractive option to modulate a modular multilevel converter are: *(i)* comparatively low switching frequency, *(ii)* simple to implement, and *(iii)* remarkably suitable for a power converter that require a large number of levels [25],[26],[27]. Notice the objective of NLC is to determine "how many" SMs per branch n_m are going to be connected/bypassed at any given time. A detailed diagram depicting the implementation of NLC is shown in Fig 4.2. First, branch reference voltage $v^*_{\mathrm{bs}m}$, containing two frequency components ($f_{\mathrm{abc}}, f_{123}$), is the input. Right after, it is divided by a SM reference voltage V^*_{C} and rounded. Then, variable n_m indicating the number of SMs to be inserted/bypass for each branch m is obtained. In the end, in regard to positive or negative values of n_m, variables $n_{\mathrm{up}m}$ and $n_{\mathrm{down}m}$ are calculated. Recalling, each full–bridge submodule contains a capacitor that is set to a reference voltage denoted as V^*_{C}. Since each submodule will switch to synthesize AC voltage on its terminals, voltage variations of V_{C} will occur. Therefore, with the objective to minimize V_{C} fluctuations of each submodule, a voltage balancing algorithm (VBA) utilized by NLC is shown in Fig. 4.3. The sorting process is performed by the use of the merge–sort algorithm, which is an efficient, general–purpose, and comparison–based sorting algorithm. It was proposed

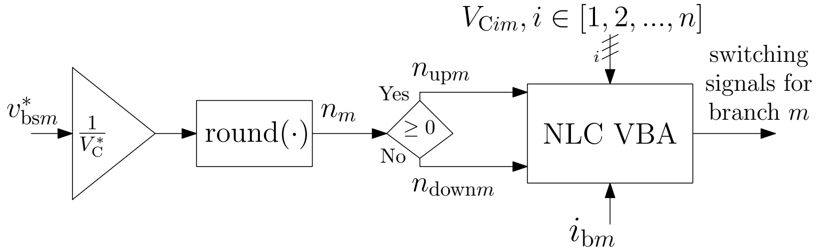

Figure 4.2: General flowchart of NLC modulation technique.

in 1945 by John von Neumann[28]. As illustrated, the inputs are: *(i)* number of SMs $n_{\mathrm{up}m}$, *(ii)* measurements of capacitors' voltage comprising each branch $V_{\mathrm{C}im}$ and *(iii)* measurement of currents flowing through each branch $i_{\mathrm{b}m}$. Thus, "which" of the submodules required to be inserted/bypass for each Hexverter branch, when synthesizing positive semi–cycles, can be determined.

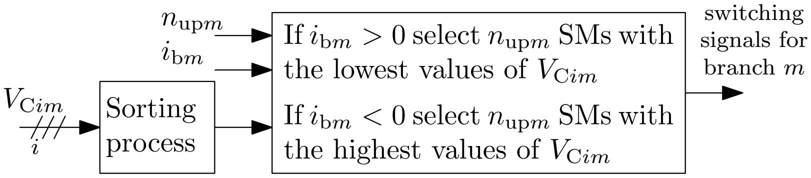

Figure 4.3: NLC VBA flowchart.

When variable $n_{\mathrm{up}m}$ is substituted by $n_{\mathrm{down}m}$ in Fig. 4.3. "Which" of the SMs required to be connected/bypass for each Hexverter branch are known. Performance evaluation of NLC VBA is discussed in Section 4.3.1.

4.2.2.2 Phase disposition–sinusoidal pulse width modulation

PD–SPWM is an extended version of the standard pulse width modulation strategy. In this case, n number of triangular waveforms [v_k=carriers] shown in Fig. 4.4, are employed. Each carrier has an amplitude of $|v_k| = -1 + \frac{2k-1}{n}$ where $k \in \{1, 2, ..., n\}$. At it can be seen, each carrier features a symmetrical offset with respect to the horizontal zero–axis. These carriers, when compared to a provided sinusoidal reference $\pm v^*_{\mathrm{bs}m}$, are employed to specifically compute the number of series connected H–bridge SMs to be connected/bypassed at any given time. Variable $n_{\mathrm{up}m}$ stores values when $+v^*_{\mathrm{bs}m}$ is used, whereas variable $n_{\mathrm{down}m}$ stores values when $-v^*_{\mathrm{bs}m}$ is utilized. A flowchart describing the process to determine $n_{\mathrm{up}m}$ is shown in Fig. 4.5. The next step is to determine "which" of the SMs will be connected at any given time, to this end, a PD–SPWM VBA is implemented. It is depicted in Fig. 4.6. The sorting process is performed by the use of the merge–sort algorithm. As shown, the inputs are: *(i)* number of SMs $n_{\mathrm{up}m}$, *(ii)* measurements of capacitors' voltage of each branch

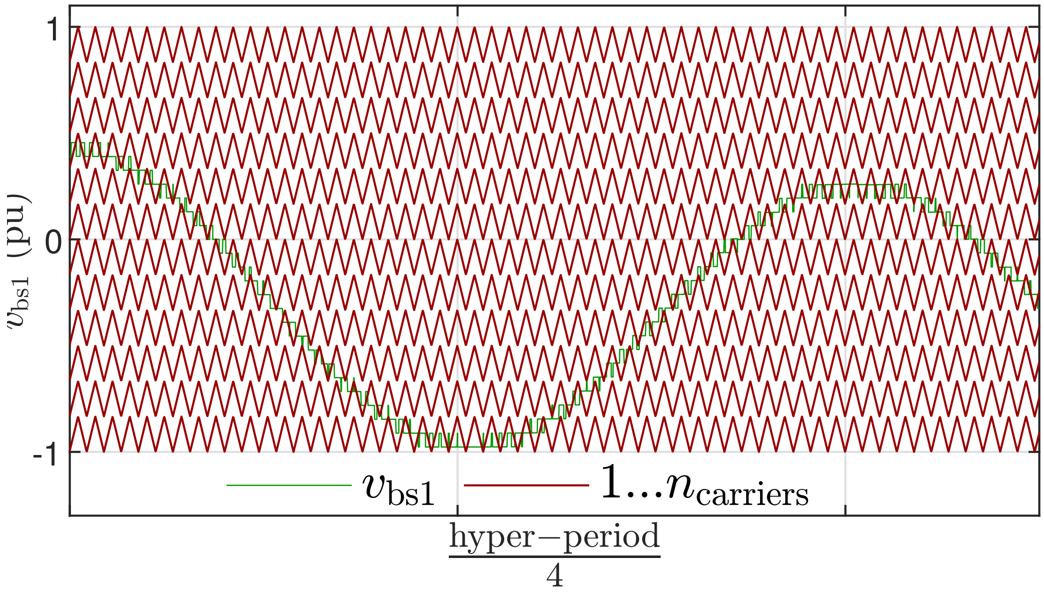

Figure 4.4: 12^{th} PD–SPWM carriers and synthesized voltage.

$V_{\mathrm{C}im}$, *(iii)* measurements of currents flowing through each branch $i_{\mathrm{b}m}$ and *(iv)* trigger signals of each branch $\mathrm{PD}-\mathrm{SPWM}_{\mathrm{up}m}$. The internal process of the PD–SPWM VBA is illustrated in Fig. 4.6, where the output is a set of switching signals for each SM comprising any of the Hexverter' branches.If variable $+v^*_{\mathrm{bs}m}$ is replaced by $-v^*_{\mathrm{bs}m}$ in Fig. 4.5, variable $n_{\mathrm{down}m}$ and trigger signals $\mathrm{PD}-\mathrm{SPWM}_{\mathrm{down}m}$ are calculated. Additionally, by plugin those in Fig. 4.6, instead of $n_{\mathrm{up}m}$ and $\mathrm{PD}-\mathrm{SPWM}_{\mathrm{up}m}$, switching signals for each submodule forming a Hexverter branch m are obtained. Performance assessment of PD–SPWM VBA is presented in Section 4.3.2.

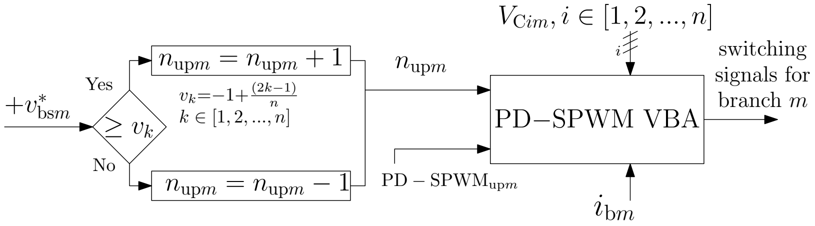

Figure 4.5: General flowchart of PD–SPWM modulation technique.

Each carrier feature a switching frequency of f_{sw}=5 kHz. However, in average each SM will switch at $\frac{f_{\mathrm{sw}}}{n}$=334 Hz per hyper–period. Be aware, a hyper–period is defined as T_h=1/gcd($f_{\mathrm{abc}}, f_{123}$).

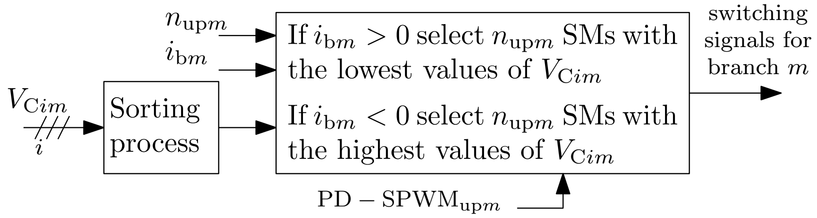

Figure 4.6: PD–SPWM VBA flowchart.

4.2.3 Proposed “virtual V_{C}^2 controller”

In order for the Hexverter–based system to perform properly, active and reactive power references (P^*_{abc}, Q^*_{abc}, P^*_{123} and Q^*_{123}) must be provided. However, as depicted in Fig. 4.9, active power reference P^*_{123} is dependent of the Hexverter’ active power losses (ΔP). In general, ΔP is composed of: (*i*) energy variations of the elements storing energy (P_{C} and P_{L} respectively), (*ii*) active power losses due to switching (P_{sw}) and conduction (P_{cond}) of semiconductors, and (*iii*) active power losses due to parasitic effects of the Hexverter’ elements which are typically modeled as resistors dissipating power (P_{R}). In this research, an approach to determine active power losses “ΔP” is studied and proposed. The main objectives are: (*i*) to achieve active power balance on the fly of the Hexverter–based system and (*ii*) to keep the submodules’ capacitor voltage as close as possible to the given reference, so that, almost all the incoming power can be transferred into the load. As shown earlier in this document, the Hexverter topology does not feature a real DC link between the connection of two AC three–phase systems, however a “virtual DC link” can be modeled by calculating an average DC voltage per submodule of each Hexverter’ branch. The DC voltage provided as the reference V^*_{C}, which in turn is the initial voltage over each full–bridge submodule before starting the operation of the Hexverter system, can be calculated as follows,

$$V^*_{\mathrm{C}} = \frac{\hat{v}_{\mathrm{abc}} + \hat{v}_{123}}{n}. \tag{4.6}$$

Considering only elements storing energy inside the Hexverter system and ideal behavior of the power converter ($P_{\mathrm{sw}} = 0$) and ($P_{\mathrm{cond}} = 0$), a general figure of the

Hexverter system is shown in Fig. 4.7. By the use of Poynting's theorem, equation (4.7) is derived,

$$P_{\mathrm{abc}} = \underbrace{\sum_{m=1}^{6}\sum_{i=1}^{n}\frac{d}{dt}\frac{1}{2}CV_{\mathrm{C}_{im}}^{2} + \sum_{i=1}^{m}\frac{d}{dt}\frac{1}{2}L_{\mathrm{b}}i_{\mathrm{b}m}^{2} + (P_{\mathrm{sw}}=0) + (P_{\mathrm{cond}}=0) + P_{\mathrm{R}}}_{\Delta P} + P_{123}. \tag{4.7}$$

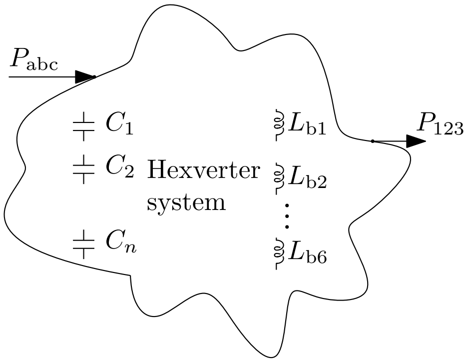

Figure 4.7: Elements storing energy in the Hexverter system.

Since the energy stored over the branch inductors is relatively low in comparison to the energy stored in the capacitors of each submodule, and the active power dissipated by the P_{R} term will add a DC–offset, active power losses "ΔP", can be estimated by considering the rate of change of the energy stored in the capacitors only. In other words, equation (4.7) becomes,

$$P_{\mathrm{abc}} = \underbrace{\sum_{m=1}^{6}\sum_{i=1}^{n}\frac{d}{dt}\frac{1}{2}CV_{\mathrm{C}_{im}}^{2}}_{\Delta P} + P_{123}. \tag{4.8}$$

Specifically, an approximation to determine "ΔP" is described by,

$$\Delta P = \frac{1}{2}C\sum_{m=1}^{6}\sum_{i=1}^{n}\frac{d}{dt}V_{\mathrm{C}_{im}}^{2}. \tag{4.9}$$

In this work, this fact is used in order to compute the Hexverter active power losses "ΔP". Furthermore, this will allow to achieve active power balance of the Hexverter–based system on the fly. A general scheme of the so called "virtual V_{C}^{2} controller" is

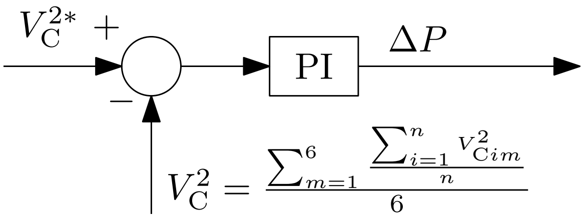

Figure 4.8: Virtual V_{C}^{2} controller block diagram.

shown in Fig. 4.8. To validate the performance of the proposed "virtual V_{C}^{2} controller" under different scenarios, Test Case I and Test Case II are developed. In Test Case I, the Hexverter–based system is considered to function keeping ideal behavior, in the sense that P_{sw} and P_{cond} are both equal to zero. By contrast, in Test Case II, a more realistic scenario of the Hexverter–based system is assessed when $P_{\mathrm{sw}}^{\mathrm{T}}$ and $P_{\mathrm{cond}}^{\mathrm{T}}$ of the IGBT's and $P_{\mathrm{cond}}^{\mathrm{D}}$ of diodes are taken into account. As described earlier, the calculation of ΔP is a necessary condition to compute active power (P_{123}^{*}) reference value for the {123} side. Once P_{123}^{*} and Q_{123}^{*} are entered to the subsystem "power–to–current" depicted in Fig. 4.1(a), correct reference values for branch currents $i_{\mathrm{b135}}^{123,dq*}$ and $i_{\mathrm{b246}}^{123,dq*}$ are obtained.

4.2.4 Hexverter–based system integration

A general schematic of the Hexverter–based system is portrayed in Fig. 4.9. It shows the integration of subsystems "virtual V_{C}^{2} controller" Fig. 4.8, branch current controllers in a unified dq framework Fig. 4.1 (a) and (b), modulator Fig. 4.2, voltage balancing algorithm Fig. 4.3 and the Hexverter system shown above on Fig. 2.4. Initially, active and reactive power references of the {abc} side (P_{abc}^{*} and Q_{abc}^{*}) are necessary operational inputs to the subsystem "power–to–current" depicted in Fig. 4.1(a), that in turn, output reference values of branch currents $i_{\mathrm{b135}}^{abc,dq*}$ and $i_{\mathrm{b246}}^{abc,dq*}$, respectively. Then, ΔP obtained from the "virtual V_{C}^{2} controller" is subtracted to P_{abc}^{*} to determine active power reference P_{123}^{*}. Based on operational conditions reactive power reference (Q_{123}^{*}) is set. These power references are feed into the "power–to–current" depicted in Fig. 4.1(a), outputting reference values of branch currents

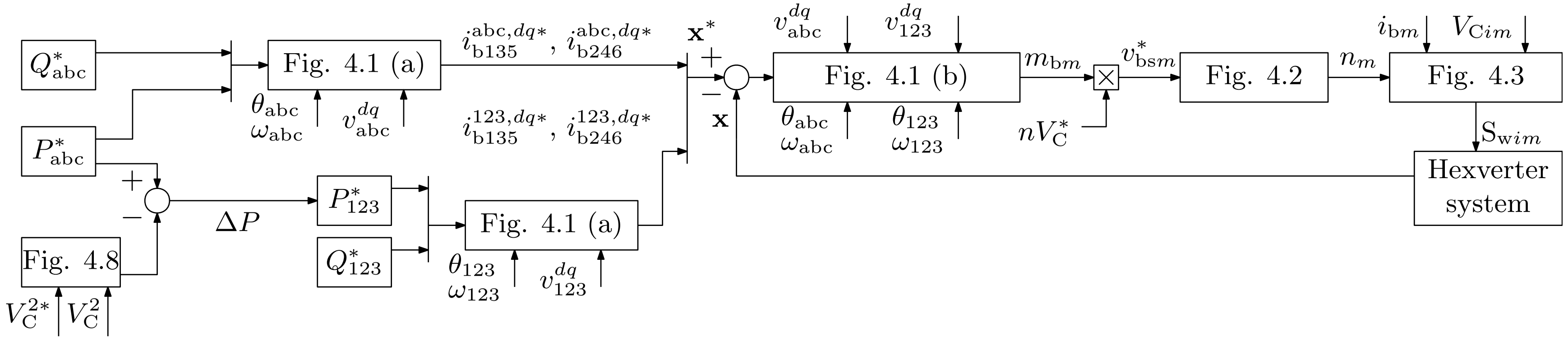

Figure 4.9: Hexverter–based system integration.

$i_{\mathrm{b135}}^{123,dq*}$ and $i_{\mathrm{b246}}^{123,dq*}$, respectively. Once x* is complete, it is compared against proper measurements and its error is fed into the branch current controller shown in Fig. 4.1 (b). Modulation indexes $m_{\mathrm{b}m}$, whose are output of the branch current controllers, become inputs for a modulator either NLC or PD–SPWM, see Figures 4.2 or 4.5. According to the selected modulation strategy the modulator outputs the number of submodules to be connected (n_m) at any given time. This is the input for the VBA that in turn generates switching signals for each power submodule comprising each Hexverter branch.

4.3 Detailed validation

Detailed simulations are implemented into the software platform PSCAD/EMTDC [29]. The objective is to verify the operation and performance of the Hexverter power converter under the application of modulations techniques NLC and PD–SPWM. The reader is referred to Table 4.1, where simulation parameters are listed. Meanwhile, an experimental prototype is being built in the author's laboratory.

4.3.1 Assessment results of NLC

Recalling that both three–phase systems are labeled as {abc} or {123}. Fig. 4.10, shows top two sub–figures depicting waveforms corresponding to AC voltages v_{abc} and v_{123}. Comparing the provided simulation parameters, both AC voltages show good match in magnitude, frequency and phase. In addition, at the bottom of Fig. 4.10, two more waveforms are presented. In one hand, v_{bs1} corresponds to synthesized branch voltage utilizing NLC modulation technique. As observed, it features typical "discrete steps or levels" indicating NLC has been precisely implemented. Moreover, a voltage magnitude nearly of 2 kV can be measured. In the other hand, i_{b1} depicts current that flows through branch one. A current magnitude close to 10 Amperes is shown. Furthermore, by carefully observing traces of voltage v_{bs1} and current i_{b1}, it can be realized they feature both frequency components ($f_{\mathrm{abc}}, f_{123}$) of the connected

Table 4.1: Simulation parameters.

Hexverter	Branch resistance	R_b	0.6 Ω
	Branch inductance	L_b	10 mH
	Number of SMs per branch	n	12
	Capacitance	C	20 mF
	Nominal SM voltage	V_C	166.67 V
System {abc}	Active power	P_abc	15 kVA
	Reactive power	Q_abc	0 kVar
	Voltage magnitude	v_abc	1 kV
	Frequency	f_abc	50 Hz
	Resistance	R_abc	1 Ω
	Inductance	L_abc	10 mH
System {123}	Active power	P_{123}	from V_C^2 control
	Reactive power	Q_{123}	0 kVar
	Voltage magnitude	v_{123}	1 kV
	Frequency	f_{123}	10 Hz
	Resistance	R_{123}	0.8 Ω
	Inductance	L_{123}	15 mH
	Voltage between neutrals	v_og	0 V
	Circulating current	i_cir	0 A

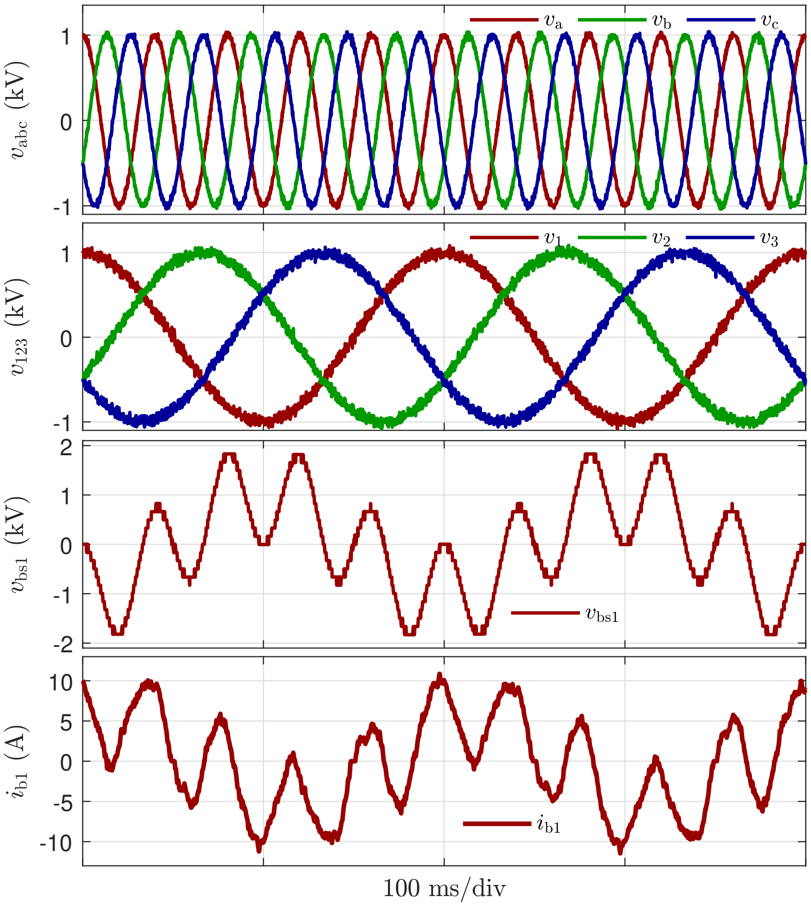

Figure 4.10: NLC: AC three–phase voltages $v_{\mathrm{abc}}, v_{123}$, branch voltage v_{bs1} and branch current i_{b1}.

AC three–phase systems. In summary, it can be mentioned that both v_{bs1} and i_{b1} are fully compliant to equations (2.7) and (2.8). In regard to the performance of the so called NLC VBA, Fig. 4.11, illustrates n traces that correspond to measurements of controlled capacitor's voltage. Based in the reported results, it can be stated that NLC VBA is controlling n voltages between a reasonable range of $V_{\mathrm{C}i1} = \pm 2.5\mathrm{V}$. This variation is approximately equal to 1.5% average error in comparison to V_{C}^{*}. NLC VBA achieves steady–state in about 200 ms.

4.3.2 Assessment results of PD–SPWM

Top two sub–figures of Fig. 4.12, depict waveforms corresponding to AC voltages v_{abc} and v_{123}. These are compliant with the provided simulation parameters due to

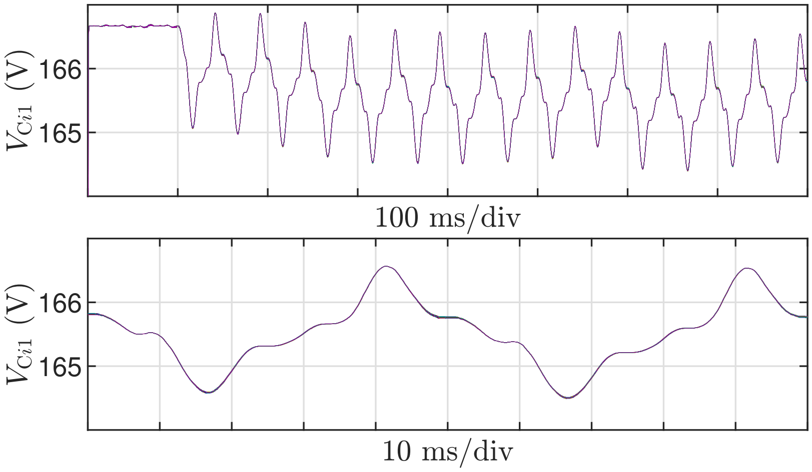

Figure 4.11: NLC VBA performance. Top) zoom–out depicting transients at initial conditions. Bottom) zoom–in at steady–state.

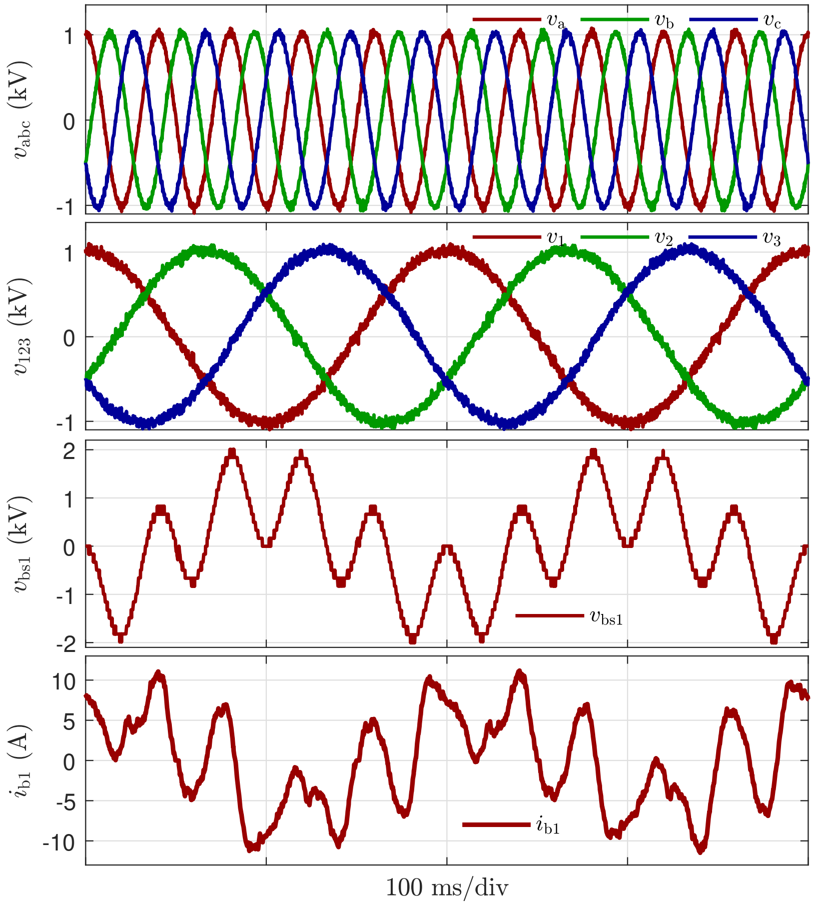

Figure 4.12: PD–SPWM: AC three–phase voltages v_{abc}, v_{123}, branch voltage v_{bs1} and branch current i_{b1}.

the fact that a good match in magnitude, frequencies and phase is observed. Moreover, bottom two sub–figures depict waveforms of v_{bs1} and i_{b1}, respectively. With respect to v_{bs1}, it shows a peak voltage of approximately 2 kV. Its trace shows typical on and off switching over the “levels” indicating PD–SPWM has been adequately implemented into the simulation. Current flowing through branch one is shown by trace i_{b1}. As expected, a peak value of about 10 Amperes can be measured. Consistent to equations (2.7) and (2.8), v_{bs1} and i_{b1} contain both frequency components $(f_{\text{abc}}, f_{123})$ of the connected AC three–phase systems. Performance of PD–SPWM VBA is presented in Fig. 4.13, where n number of controlled capacitor's voltage waveforms are depicted. PD–SPWM VBA is controlling all branch capacitor's voltages $V_{\text{C}i1} = \pm 3.0\text{V}$ compared to V_{C}^{*}; representing 1.80% average error. PD–SPWM VBA performs the same in all other branches. It reaches steady–state, in about 300 ms.

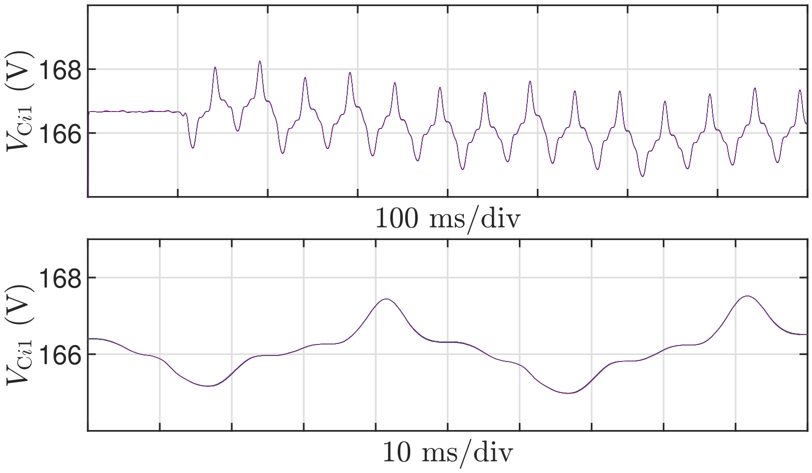

Figure 4.13: PD–SPWM VBA performance. Top) zoom–out depicting transients at initial conditions. Bottom) zoom–in at steady–state.

4.3.3 NLC and PD–SPWM discussion of results

Regarding the implementation of NLC and PD–SPWM into the Hexverter–based multilevel converter and based on simulation results shown from Fig. 4.10 to Fig. 4.13, three main points can be mentioned. *(i)* since with the naked eye almost no difference can be observed in both synthesized AC voltages and currents, it becomes necessary to analyze in depth these waveforms. Thus, in order to determine which modulation technique outperform the other in terms of its harmonic spectrum and total harmonic distortion, the reader is referred to section 9. *(ii)* in one hand, branch v_{bs1} voltages show a small difference in the number of levels to synthesize the same Hexverter' terminal voltages; in the other hand, both branch currents i_{b1} are clearly different, it can be mentioned branch current out of PD–SPWM is more distorted than the one measure when NLC modulation technique is utilized. *(iii)* a small difference of 0.3% average error is measured when comparing both voltage balancing algorithms.

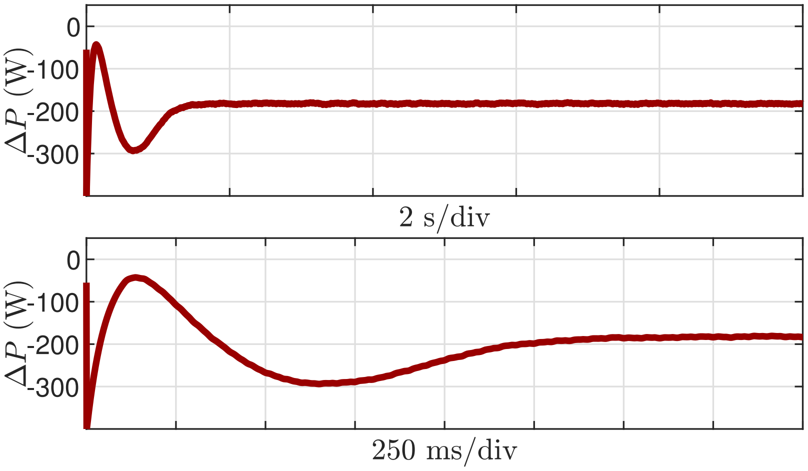

Figure 4.14: Test Case I: NLC ΔP value obtained with "virtual V_{C}^2 control".

4.3.4 Performance of "virtual V_{C}^2 controller"

In order to validate the performance of the "virtual V_{C}^2 controller" two different scenarios are considered.

4.3.5 Test Case I

In this scenario the Hexverter power converter is considered a lossless system. In other words, P_{sw} and P_{cond} are both equal to zero. Be aware, the parasitic effects of the Hexverter' reactive elements are modeled into the branch resistor R_{b}. Performance of "virtual V_{C}^2 control" under NLC modulation technique is depicted in Fig. 4.14. At the beginning of the trace a transient behavior appear due to the rate of change of energy into the submodule's capacitor and branch inductors, nevertheless, under this transient conditions the controller is able to achieve and provide correct active power balance reference for the AC system $\{123\}$. As observed the controller takes approximately 1.25 seconds to reach steady state with a ΔP value of 184 W. By analyzing equation (4.7), this value of ΔP parameter corresponds to a DC–offset due to the embedded calculation of P_{R} term. In order to verify the correctness of the calculated ΔP value, the reader is referred to Table 4.1, where the active power reference of the AC system $\{abc\}$ $\mathrm{P}^*_{\mathrm{abc}}$ =15kVA is provided.

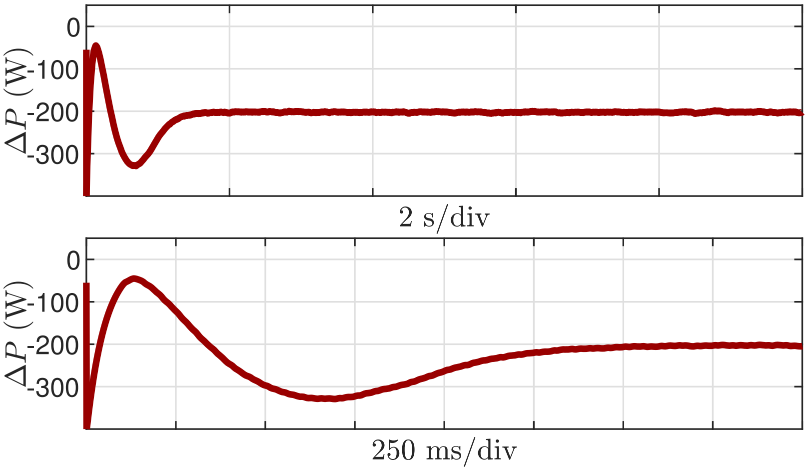

Figure 4.15: Test Case I: PD–SPWM ΔP parameter obtained with "virtual V_{C}^2 control".

In the same fashion, performance of "virtual V_{C}^2 control" under PD–SPWM modulation technique is depicted in Fig. 4.15. As expected, a transient behavior of ΔP trace appears at the beginning. However, one more time the controller is able to achieve and provide correct active power balance reference for the AC system $\{123\}$. As it is depicted, the controller takes about 1.5 seconds to achieve steady state with a value of 202 W, that corresponds to a DC–offset due to the embedded calculation of P_{R} term. By comparing both ΔP parameter values out of both modulation techniques, an active power difference of 18 W is observed. It seems that by utilizing this simulation setup, active power losses are 18 W higher when PD–SPWM is utilized.

4.3.6 Test Case II

In this scenario, the Hexverter power converter is no longer considered a lossless system. The IGBT transistor part number IRG4BC30KDPbF is selected. Its main parameters are listed in Table 4.2, and it includes an ultrafast soft recovery diode connected in antiparallel. Since all branch reference voltages coming out from the implemented current controllers, submodules' DC–link voltages and branch current directions are known, duty cycles for the IGBTs and diodes define with variables ($d^{\mathrm{T}}_{\mathrm{b},mi}$ and $d^{\mathrm{D}}_{\mathrm{b},mi}$) can be determine [9]. Switching and conduction losses of a single transistor are define by variables $P^{\mathrm{T}}_{\mathrm{sw}}$ and $P^{\mathrm{T}}_{\mathrm{cond}}$, respectively. Those can be estimated by equations (4.10) and (4.11),

$$P^{\mathrm{T}}_{\mathrm{sw}} = (E_{\mathrm{ON_T}} + E_{\mathrm{OFF_T}})\frac{V_{\mathrm{Throw}}\bar{i_{\mathrm{T}}}}{V_{\mathrm{REF_T}}I_{\mathrm{REF_T}}}f_{\mathrm{sw}} \tag{4.10}$$

$$P^{\mathrm{T}}_{\mathrm{cond}} = d^{\mathrm{T}}_{\mathrm{b},mi}V_{\mathrm{CE_{ON_T}}}\bar{i_{\mathrm{T}}}. \tag{4.11}$$

Similarly, conduction loss of a single diode is defined by variable $P^{\mathrm{D}}_{\mathrm{cond}}$ and can be approximated by equation (4.12),

$$P^{\mathrm{D}}_{\mathrm{cond}} = d^{\mathrm{D}}_{\mathrm{b},mi}V_{\mathrm{F_D}}\bar{i_{\mathrm{D}}}. \tag{4.12}$$

Bear in mind, $\bar{i_{\mathrm{T}}}$ and $\bar{i_{\mathrm{D}}}$ are both equal to magnitude of branch current $|i_{\mathrm{b},m}|$ and V_{Throw} is equal to the given reference voltage for each submodule V^{*}_{C}. Furthermore, in order to determine the mean values for the active power losses, all calculations are performed over a hyper–period defined earlier as $T_h = 1/\mathrm{gcd}(f_{\mathrm{abc}}, f_{123})$.

The functioning of the proposed "virtual V^2_{C} controller" under NLC modulation technique is depicted in Fig. 4.16. It shows a transient behavior of ΔP trace of approximately 1.25 seconds, nonetheless the controller is able to reach steady state conditions with a value of 1.303 kW, while providing active power reference for the

Table 4.2: Nominal parameters of the IGBT and Diode part number: IRG4BC30KDPbF and operational conditions.

Transistor	Collector–to–emitter voltage	V_{CES}	600V
	Continuous collector current	I_{C}@ T_{C}=25°C	28A
	Collector–to–emitter saturation voltage	$V_{\mathrm{CE}_{\mathrm{ON}_{\mathrm{T}}}}$	2.21V
	Turn–on switching loss	$E_{\mathrm{ON}_{\mathrm{T}}}$	0.60mJ
	Turn–off switching loss	$E_{\mathrm{OFF}_{\mathrm{T}}}$	0.58mJ
Diode	continuous forward current	$I_{\mathrm{F}_{\mathrm{D}}}$	12A
	forward voltage drop	$V_{\mathrm{F}_{\mathrm{D}}}$	1.4V
Operational conditions	Operating voltage	$V_{\mathrm{REF}_{\mathrm{T}}}$	167V
	Peak value of operating current	$\hat{I}_{\mathrm{REF}_{\mathrm{T}}}$	10A
	Transistor throw voltage	V_{Throw}	167V

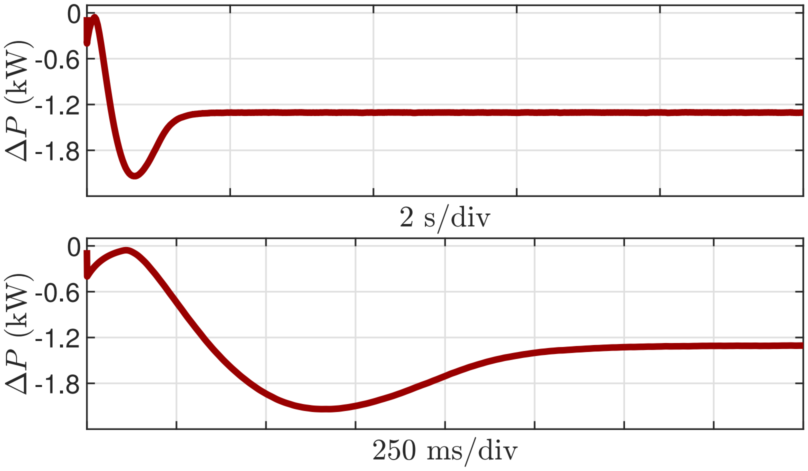

Figure 4.16: Test Case II: NLC ΔP value obtained with "virtual V_{C}^2 control".

AC system $\{123\}$. As shown in Fig. 4.17, this value of ΔP agrees with active power reference P_{123}^{*} and its measurement. Furthermore, it can be stated that both traces of P_{123}^{*} and P_{123} are in practice on top of each other. This indicates the performance of the "virtual V_{C}^2 controller". Considering the efficiency equation defined by $\eta = \frac{P_{\mathrm{abc}}-\Delta P}{P_{\mathrm{abc}}} \times 100$, the Hexverter power converter seems to be performing at $\eta = 91.31$

efficiency. This value obtained agrees with the studies regarding efficiency developed in [9]. Correspondingly, performance assessment of "virtual V_C^2 controller" under PD–

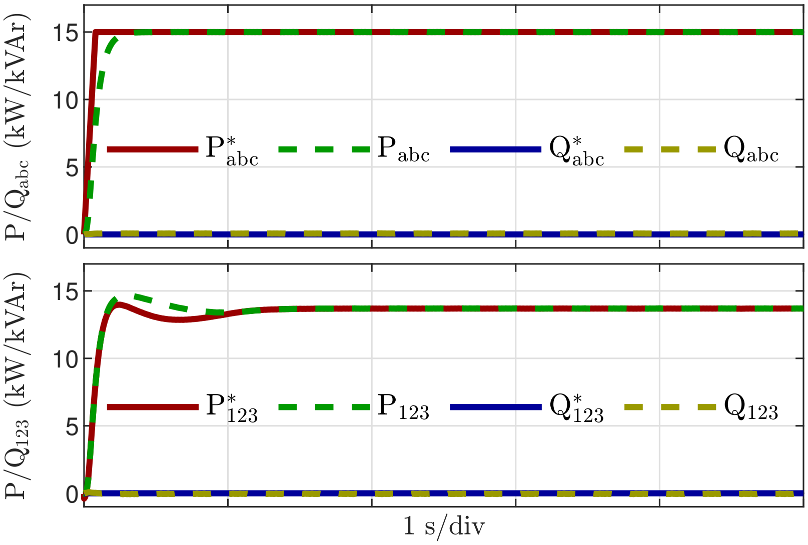

Figure 4.17: Test Case II: comparison of (P^*_{abc}, Q^*_{abc}, P^*_{123} and P^*_{123}) vs measurements under NLC modulation.

SPWM modulation strategy is shown in Fig. 4.18. After the transient behavior of ΔP trace, the controller reaches steady state in about 1.4 seconds with a value of 1.317kW. At the same time, it provides active power reference for the three–phase AC system {123}. This value of ΔP agrees with active power reference P^*_{123} and its measurement,

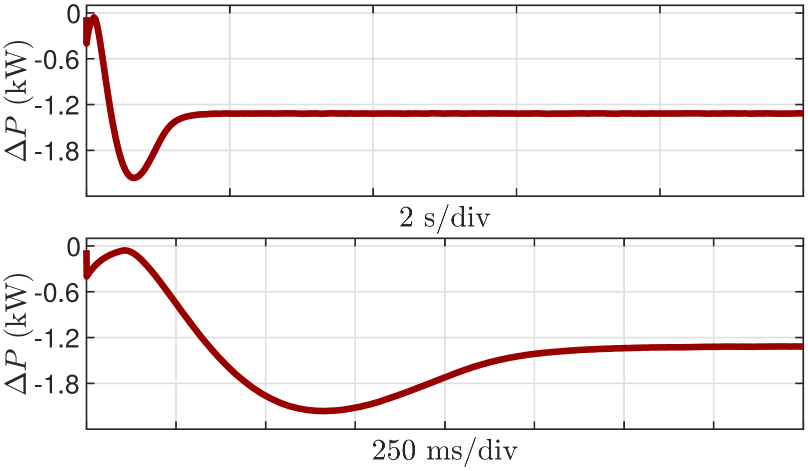

Figure 4.18: Test Case II: PD–SPWM ΔP value obtained with "virtual V_C^2 control".

as it is illustrated in Fig. 4.19. Furthermore, it can be stated that both traces of P^*_{123}

and P_{123} are practically attached to each other. This indicates the performance of the "virtual V_C^2 controller". Under the above circumstances, the Hexverter–based system seems to perform with a value of η =91.22 efficiency. In summary, by comparing the results obtained out of Test Cases I and II, the Hexverter–based system seems to be more efficient when NLC modulation technique is utilized.

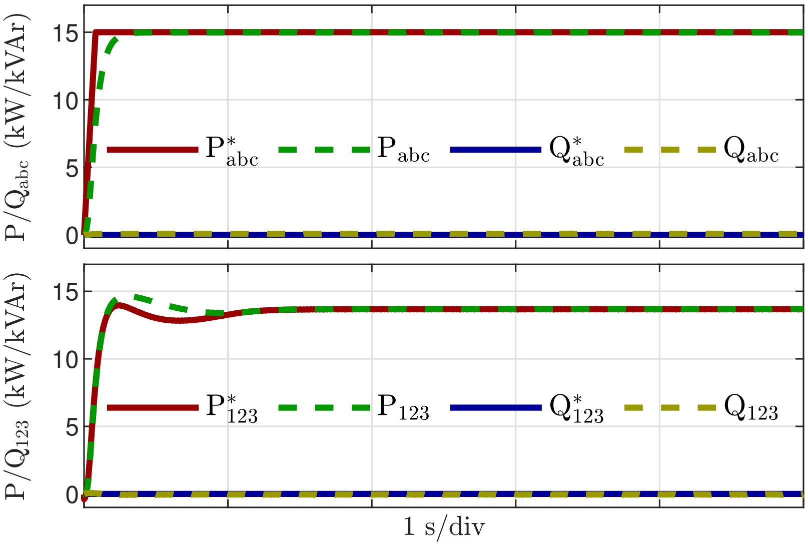

Figure 4.19: Test Case II: comparison of (P^*_abc, Q^*_abc, P^*_{123} and P^*_{123}) vs measurements under PD–SPWM.

4.3.7 Assessment of harmonic spectrum and total harmonic distortion

Total harmonic distortion (THD) of any single phase waveform, can be estimated by equation (4.13),

$$\mathrm{THD} = \frac{\sqrt{\sum_{k=2}^{\infty} \mathrm{h}_k^2}}{\mathrm{h}_1}, \tag{4.13}$$

where h_1 accounts for the amplitude of the fundamental frequency and h_k stands for any harmonic's amplitude multiple of the fundamental frequency.

4.3.8 Single phase voltage THD assessment under NLC

Five cycles of single phase voltage v_a are depicted in the top–left section of Fig. 4.20. This voltage is measured at Hexverter' terminals labeled as $\mathrm{PCC_{abc}}$ (see Fig.

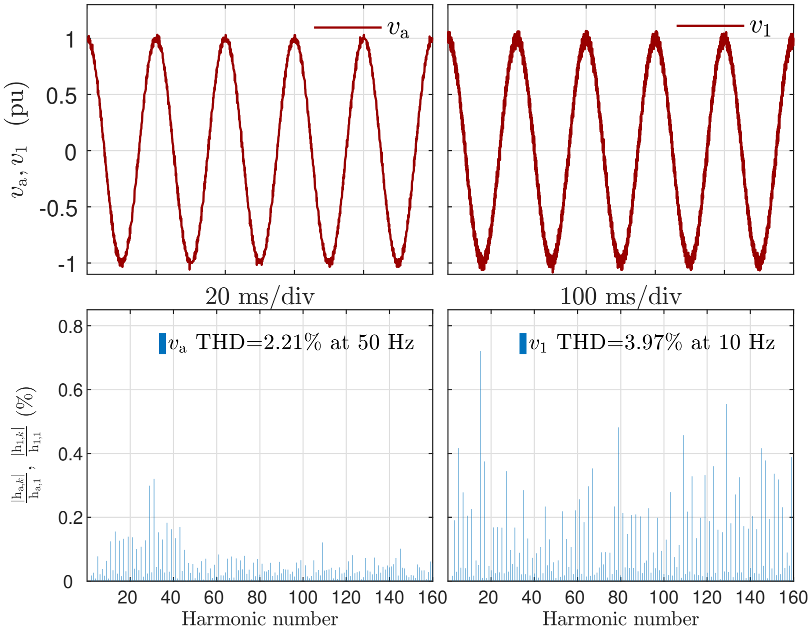

Figure 4.20: Spectrum of v_a, v_1 and THD calculations, when NLC modulation technique is utilized.

2.4). Its frequency, magnitude and phase are compliant with simulation parameters. Moreover, the harmonic content of v_a is assessed and illustrated in the bottom–left of Fig. 4.20. A set of 160 harmonics labeled as $h_{a,k}$ are shown. As expected its magnitudes are monotonically decreasing as its harmonic order increases. Its THD is then calculated and equal to 2.21%. Harmonic's number 29^{th}= 1450 Hz and 31^{th}=1550 Hz are the most representative featuring a magnitude of approximately 0.30%. In the same fashion, five cycles of single phase voltage v_1 are shown at the top–right section of Fig. 4.20. This voltage is being measured at Hexverter' terminals labeled as PCC_{123} (see Fig. 2.4). By simple inspection of Fig. 4.20, v_1 looks more distorted as compare to v_a. This claim is consistent with the evaluation of v_1 harmonic content which generates a value of 3.97% THD. A set of 160 harmonics labeled as $h_{1,k}$ are shown in the bottom–right section of Fig. 4.20. Notice, its magnitudes are monotonically decreasing as its harmonic order increases. In this case, harmonic's number 15^{th}= 150 Hz, 79^{th}= 790 Hz and 129^{th}=1290 Hz are the most representative, they feature magnitudes of 0.7%, 0.5% and 0.55%, respectively.

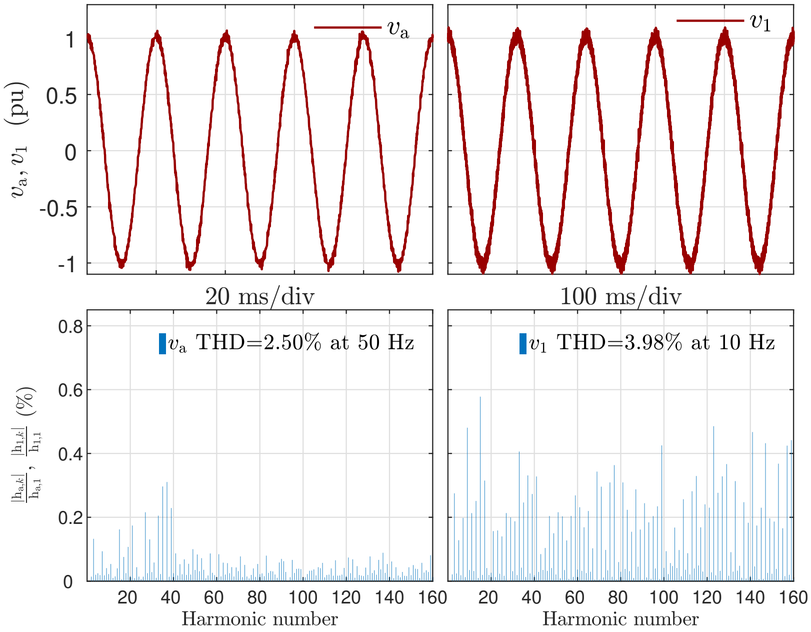

Figure 4.21: Spectrum of v_a, v_1 and THD results, when PD–SPWM modulation technique is utilized.

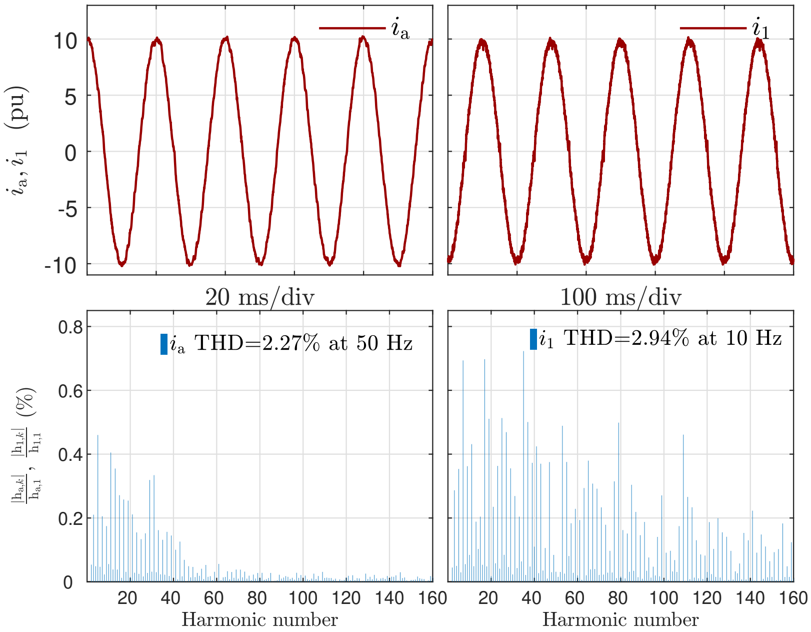

Figure 4.22: Spectrum of i_a, i_1 and THD calculations, when NLC modulation technique is utilized.

4.3.9 Single phase voltage THD assessment under PD–SPWM

Five cycles of single phase voltage v_a are shown in top–left section of Fig. 4.21. Correspondingly, top–right section of the same figure shows five cycles of single phase voltage v_1. Both voltage waveforms were measured at each PCC, respectively. Harmonic distortion measurement of single phase voltage v_a indicates a THD value = 2.50%. It is 13.2% higher in comparison to the THD value obtained by NLC modulation. Similarly, a THD value of v_1 equal to 3.98% is calculated. This former number indicates that independently of the modulation technique, almost no difference regarding the THD value of v_1 can be observed. Be aware, harmonic number 15^{th}= 150 Hz, feature the highest magnitude (0.7% and 0.6%, respectively) under both modulation techniques.

4.3.10 Single phase current THD assessment under NLC

Single phase current i_a is depicted in the top–left section of Fig. 4.22. This current shows an amplitude of 10 Amperes, that in turn, is compliant with simulation parameters. Its harmonic content is evaluated and shown in bottom–left section of Fig. 4.22. The THD calculation indicates a number equal to 2.27%. Low order harmonics, less than 3000 Hz, are the most representative featuring a highest magnitude of 0.46%. Similar trace is shown to indicate i_1 in the top–right section of Fig. 4.22. As expected, this current feature an amplitude of nearly 10 Amperes. Its harmonic content correspond to a value of 2.94%. Harmonics number 7^{th}, 17^{th} and 35^{th} are the more representative featuring magnitudes fairly close to 0.7%.

4.3.11 Single phase current THD assessment under PD–SPWM

Single phase current i_a is depicted in the top–left section of Fig. 4.23. Likewise, top–right section of Fig. 4.23 shows single phase current i_1. Both traces were measured at each PCC. Harmonic distortion computation of single phase currents indicate THD values of 3.19% and 4.52%, respectively. THD values of PD–SPWM

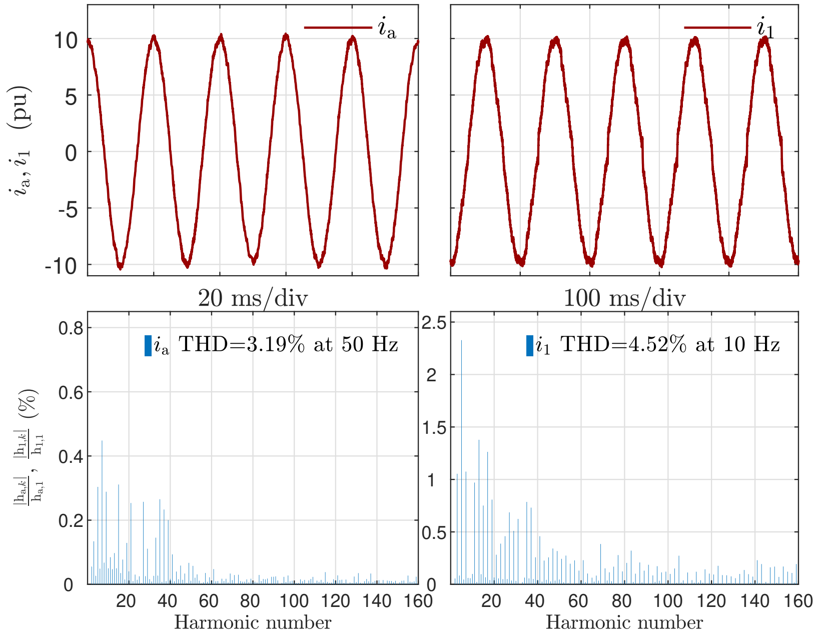

Figure 4.23: Spectrum of i_a, i_1 and THD results, when PD–SPWM modulation technique is utilized.

are higher than NLC in 40.6% and 54%, each. Be aware, i_1 harmonic number $5^{\mathrm{th}} =$ 50 Hz features the highest amplitude of 2.3% under PD–SPWM.

In summary, all the THD values obtained out of PSCAD/EMTDC simulations are compliant with international standards IEEE 519 [2] and IEC61000–3–2 [3]. Moreover, it seems NLC modulation strategy outperforms PD–SPWM modulation technique when THD of synthesized waveforms is considered. In future work, some THD values can be reduced to a minimum by properly implementing modulation techniques such as harmonic elimination and selective harmonic elimination.

4.4 Conclusions

In this chapter, the operational principle of the direct AC–AC multilevel power converter "Hexverter" was presented. The subsystems *(i)* branch current controller performing in a unified two–frequency *dq* framework, and *(ii)* a proposed "virtual V_C^2 controller" were integrated to a power converter setup composed of: *(a)* modulator, *(b)* voltage balancing algorithm and *(c)* Hexverter system. The results obtained suggest the control scheme is able to regulate the Hexverter–based system under both modulation strategies. Moreover, an assessment of total harmonic distortion of AC three–phase voltages and currents was thoroughly developed. It seems, NLC modulation strategy outperforms PD–SPWM modulation technique. For instance, THD of v_{a} is 13.2% higher under PD–SPWM than under NLC. Likewise, THD of i_1 is 54% higher under PD–SPWM than under NLC. Be aware, all the THD values obtained out of PSCAD/EMTDC simulations are compliant with international standards IEEE 519 [2] and IEC61000–3–2 [3]. Validations of proposed "virtual V_{C}^2 control" were presented. According to the results obtained, "virtual V_{C}^2 controller" was able to accurately determine the active power loss of the Hexverter–based system. Furthermore, by assessing ΔP values of both modulation techniques and under the scenarios of Test Case I and II, nearest level control technique yielded superior efficiency. Experimental validation of the analysis presented herein is currently under investigation. Results will be published as they become available.

CHAPTER 5

DETAILED MODELING OF LARGE SCALE PHOTOVOLTAIC POWER PLANTS UNDER PARTIAL SHADING CONDITIONS

5.1 Motivation & present state of knowledge

A photovoltaic (PV) panel is a renewable energy source that directly converts solar irradiance into electricity through the PV effect. With the current growth of PV adoption, many believe it will become a significant contributor to our energy generation portfolio. To aid in this growth, there is currently significant interest in developing viable PV systems for large scale installations. The large geographic footprint of a large scale installation, known as a PV power plant, has unique challenges. Due to the large surface area, clouds, dust, and shadows may have a non–uniform effect on the solar irradiance seen by a PV power plant. This phenomenon, known as partial shading (PS), is a major source of reduction for both the lifespan and the output power generated by a PV power plant.

Output power reduction stems from the added complexity that PS creates for the control algorithm. In an effort to maximize the amount of power extracted from a PV system, a maximum power point tracking (MPPT) algorithm is utilized. MPPT algorithms typically take advantage of the convex shape of the power–voltage (P–V) performance curve. PS conditions, however, create several local maxima along the convex P–V performance curve [30], making the MPPT considerably more challenging. Conventional MPPT algorithms tend to get trapped by these local maxima, instead of finding the global maxima, thus reducing the amount of power extracted.

In addition to PS reducing output power, lifespan is also reduced. Building–block components of a PV system, known as PV cells, see a varied amount of solar irradiance during PS. Lifespan reduction occurs from the hot–spots that form in the PV cells seeing less irradiance. When PV cells are connected in series, the PV cells seeing less irradiance are forced to carry the same current as the PV cells seeing a higher irradiance [31, 30, 32]. The PV cells seeing less irradiance act as loads and thus heat up, reducing the lifespan of the PV system.

Large scale PV systems can be prone to faulty conditions which further contribute to the reduction of power production and lifespan. These faulty conditions can be the result of mechanical, environmental, or electrical conditions. To overcome these challenges, real–time advanced monitoring techniques have been proposed to monitor and diagnose PV system components. In [33], the authors introduced fault indicator thresholds based on predefined healthy operating conditions. The proposed method was able to determine if the PV system was operating in fault status, and it was also able to determine the type of fault. In a separate approach to reduce power losses due to PS conditions, [34] proposed detecting temporary faults utilizing voltage and current indicators.

In an effort to reduce the detrimental effects of PS, there has been significant research on connecting a string of PV cells in anti–parallel with a bypass–diode (BPD). A BPD allows the higher current, due to the PV cells experiencing higher irradiance, to bypass the PV cells experiencing a lower amount of irradiance. In a review and analysis, [31] shows that implementing BPDs increase the lifespan of PV cells and also maximize power output by minimizing the losses associated with cells acting as loads.

There have been significant advances towards creating a viable PV system for widespread PV power plant adoption. Studies have researched the way PV cells are connected and optimized, in order to minimize the effects of partial shading. Considerable attention has been paid to determine the optimal architecture of a PV power plant, including techniques for modularization as well as reconfiguration and topological interconnection of cells. Efforts have also been made to efficiently and accurately model PV systems, both thermally and electrically. Other studies have integrated MPPT algorithms into power converters and are capable of adapting their behavior. The following is a literature review that helps locate this work in the field of PV research.

Significant research has been performed to improve performance during PS, including several studies focused on the effects of various topological connections of PV cells to power converters. A modular configuration for PV power generation was proposed by [35]. First, this modular system consists of PV arrays connected directly to dedicated DC–DC converters, that are all tied to a common DC bus. Each PV array is then independently controlled by an MPPT algorithm, ensuring that the MPP is achieved. Second, DC–AC inverters, known as voltage source inverters (VSI), are then parallel–connected to the common DC bus. Utilizing a current–decoupling method, the parallel–connected VSI modules optimize load sharing and provide redundancy, thus improving system efficiency. The main drawback of this approach, compared to the conventional centralized topology, is the increased economic cost due to the additional power converters and inverters. In a separate paper, [36] proposed a different modularization strategy for large PV power plants. The authors connected a bidirectional DC–DC converter, per every two series–connected PV panels, which was controlled independently according to environmental conditions. Additionally, a DC–DC converter was connected to every parallel branch, to control the DC bus voltage. The main drawback of this approach was the need for the extra DC–DC converter, to sufficiently step–up the DC bus voltage.

Taking a different approach, [37] proposed utilizing a modular multilevel converter, in order to extract the maximum power under PS conditions. The authors proposed connecting a PV panel in parallel with the capacitor in each submodule of the modular multilevel converter. The maximum power can then be extracted by regulating the voltage across each capacitor, in order to achieve the PV systems maximum power point (MPP). This approach is advantageous during PS because the PV panels are not directly series–connected, thus the power losses can be kept to a minimum. These papers all demonstrate the benefit of additional power converters during PS conditions.

In other efforts to reduce the effects of PS, several papers have researched the effects of different electrical connections on power generation. In [38] topological interconnections of PV panels were analyzed and compared during six different scenarios of PS conditions. These configurations were named accordingly to their interconnection as series, series–parallel, total–cross–tied, bridge–linked and honeycomb. Results of shading cases were compared in terms of shading loss, mismatch loss and fill factor. In addition, an assessment of the power produced from each topological interconnection was carried out. It was determined, for all cases of PS conditions, that total–cross–tied configuration featured the highest maximum power, the lowest mismatch loss and fill factor. Further studies of topological interconnections can be found in [39] and [40] and demonstrate the positive effect of creative interconnections during PS conditions.

Using another method to minimize the PS issue, several papers have explored dynamic reconfiguration of the electrical topology. One reconfiguration technique was demonstrated in [41], in order to improve power extraction from a PV system in a reduced computational time. This technique employed the greedy optimization principle, creating a simple strategy to find the optimal PV cell electrical topology. In this strategy, the electrical connection of PV panels was swapped, through switches, from one series–connected row to another. This was done in order to connect, in series, PV panels experiencing a similar level of irradiance. This swapping process was utilized until it was not possible to further minimize the irradiance difference inside the series–connected rows. In a different approach [42] studied an electrical array reconfiguration technique using high–speed processors, low–cost switching devices and data acquisition systems. Similar to the Mahmoud paper mentioned previously, the physical location of the modules remained the same while its electrical connections were altered. The difference here is that the authors optimized the electrical connections by the particle swarm optimization method. Comprehensive comparisons of energy savings, power generated and various electrical array reconfiguration techniques were performed. While studying another approach, [43] proposed utilizing a computer–aided design tool to model, study and understand the effects of PS on PV systems. This tool can be used to study the effects of various PV array configurations on the output power when taking into consideration likely shading patterns. In all of these papers, the authors decreased the effect of PS on PV systems by actively managing the reconfigurations of the electrical connections between panels.

In order to accurately model the behavior of a PV system, its thermal effects need to be considered. This is a challenge because the PV cell junction temperature is typically not available for direct measurement. Due to this, there have been several authors [44], [45], and [46] that have developed expressions to estimate the PV cell junction temperature. These models are based on several parameters, including ambient temperature, wind speed, and solar irradiance. Comparing the results of these models ([44] and [45]) show little difference and then they also suggest that this is due to wind speed significantly cooling down the PV cell junction temperature. These models, however, are limited because they do not take into account the additional thermal effects of the BPD.

Lifespan reduction, due to the hot–spots created by PS is another research topic. A BPD strategy proposed by [47] significantly reduced hot–spot temperature in both partial and full PS conditions. This technique utilized a series–connected MOSFET transistor, which reduces the reverse voltage created by the shaded solar cells, by acting as a voltage divider. The proposed solution does not rely on either a control logic or a power supply. According to the authors, experimental results have shown that the shaded cells hot–spot temperature can be reduced by up to 24 °C further than the standard BPD approach.

In addition to topological research, many studies have focused on the mathematical modeling of the PV cell. Several authors have reported that the five–parameter single–diode model can effectively represent the current–voltage (I–V) characteristics of a PV cell. The five–parameter model, given by [48], uses the I–V relationship for a PV cell and includes the ability to model PV cells or panels connected in series. An enhanced version of the aforementioned model was proposed in [49]. It was demonstrated that the model can accurately represent the electrical behavior of any size array of PV cells. Focusing on a different method, [50] proposed modeling a PV cell with a modified two–diode model. Typical two–diode models are not favored, compared to one–diode models, due to their large increase in computational time. However, they were able to reduce the simulation computational time by using a method that required only four parameters, instead of seven, to characterize the I–V and P–V curves of a PV cell. Furthermore, their software was able to simulate large PV arrays, assuming they were connected to power electronic converters controlled by MPPT algorithms. While these studies have all been able to accurately model a PV cell, they have not included the use of a BPD.

In yet another attempt to increase power extraction from PV systems, MPPT algorithms are used to track the global maximum power point. However, conventional MPPT methods such as perturb and observe and also incremental conductance are not able to accurately cope with PS conditions. This drawback has given rise to various advanced MPPT algorithms approaches. These advanced techniques employ strategies such as linear search, which is an improvement over conventional MPPT algorithms. Other advanced MPPT algorithms employ artificial intelligence techniques such as utilizing a neural network and fuzzy logic. Also utilizing artificial intelligence, some MPPT algorithms utilize a meta–heuristic procedure based on optimization techniques such as particle swarm optimization [51]. Several studies have also focused on the integration of MPPT methods and power electronic converters.

For example, an MPPT algorithm able to consider the various local maxima of the P–V curve, due to PS conditions, was developed in [52]. Here the authors controlled a standard DC–DC converter with this new MPPT algorithm. Similarly, [53] integrated a new MPPT technique to a standard DC–DC converter. Here the authors developed an online geometrical MPPT technique that uses the voltage and current deviations of a PV system, to find its power slopes. The algorithm then selects how to change the current coming from the PV system, based on the power slopes, in an attempt to achieve the MPP. Unlike conventional MPPT techniques, PS MPPT algorithms are adaptive to the power curves, however, they are unable to maximize a BPD connected PV system.

The above–mentioned studies have contributed to significant advancements in the power extraction of PV systems experiencing PS. They did not, however, take into account detailed modeling of PV cells connected to BPDs. In addition, junction temperature modeling of PV cells connected to BPDs was not investigated in regards to variations caused by ambient temperature, cell temperature, and wind speed fluctuations.

In an effort to address the above–mentioned research gap, the aim of this investigation is to synthesize a thermoelectric modular model of PV cells connected to BPDs. This is done in order to more accurately emulate the behavior of PV cells connected to BPDs under PS conditions. The proposed model features modularity and thus can be scaled to represent any size array of PV cells.

The effectiveness of the proposed model is then benchmark validated against the built–in Matlab–Simscape PV panel block [54]. Here we also validate and analyze the model in PSCAD/EMTDC. This validation includes the use of partial shading modeling, real data measurements of ambient temperature, cell temperature, and wind speed. Finally, a performance analysis of several MPPT algorithms, proposed in [55], is carried out.

In summary, the contributions of this work are:

- A thermoelectric modular model that is able to represent a PV power plant of an arbitrary size capturing the details of all the constituent PV cells and BPDs through a single equivalent circuital representation. The model synthesizes *I*–*V* performance curves and computes junction temperatures of PV cells and BPDs from data that is generally available from measurements: solar irradiance, ambient temperature and wind speed.

- A novel thermal equation that yields BPDs' junction temperature, including the heat transfer phenomena into the junction box, due to dissipated power, radiation, convection, and conduction.

- An application example of the proposed model comprising a comparative evaluation of several MPPT algorithms while operating on a large grid–connected PV power plant, subjected to realistic PS conditions. The simulation is implemented in PSCAD/EMTDC, and includes the proposed model, a VSI, a step up transformer and a Thévenin equivalent of a power grid, along with real values of solar irradiance, ambient temperature, and wind speed measurements.

The rest of this work is organized as follows. First, a model for BPDs connected to PV cells, as well as a discussion regarding the derivation of the proposed model, is described in section 5.2.1. Next, model validations are presented in section 5.3. Then, an application example is detailed and analyzed in section 5.4. Finally, conclusions are reported in section 5.5.

5.2 Technical approach

5.2.1 Mathematical modeling

This section develops a thermoelectric modular model of PV cells connected to BPDs, able to be scaled to any size. The model characterization considers standard

Nomenclature

A	Cross–section area of the diode (cm^2)
A^*	Richardson's constant (112 $\mathrm{Acm}^{-2}\mathrm{K}^{-2}$)
E_a	Dopant activation energy (eV)
E_g	Bandgap energy (eV)
E_0	Tunneling energy (eV)
G	Solar irradiance ($\mathrm{W/m}^2$)
G_0	Reference solar irradiance on panel (1000 $\mathrm{W/m}^2$)
I_0	Cell saturation current (A)
I_{d0}	Diode saturation current (A)
I_{irr}	Photocurrent (A)
$I_{\mathcal{P}\mathrm{array}}$	Total output current of $\mathcal{P}_{\mathrm{array}}$ (A)
$I_{\mathcal{P}\mathrm{cell}}$	Total output current of $\mathcal{P}_{\mathrm{cell}}$ (A)
$I_{\mathcal{P}\mathrm{diode}}$	Total output current of $\mathcal{P}_{\mathrm{diode}}$ (A)
$I_{\mathcal{P}\mathrm{panel}}$	Total output current of $\mathcal{P}_{\mathrm{panel}}$ (A)
$I_{\mathcal{P}\mathrm{section}}$	Total output current of $\mathcal{P}_{\mathrm{block}}$ (A)
N_{cs}	Number of series connected cells
N_{cp}	Number of parallel connected strings of cells
N_{ds}	Number of series connected diodes
N_{dp}	Number of parallel connected strings of diodes
N_{ps}	Number of series connected PV panels
N_{pp}	Number of parallel connected strings of PV panels
N_{ss}	Number of series connected sections
$\mathcal{P}_{\mathrm{array}}$	$N_{\mathrm{cs}} \times N_{\mathrm{cp}}$ array of series–parallel connected PV panels
$\mathcal{P}_{\mathrm{block}}$	A parallel connection of $\mathcal{P}_{\mathrm{cell}}$ and $\mathcal{P}_{\mathrm{diode}}$ partitions
$\mathcal{P}_{\mathrm{cell}}$	$N_{\mathrm{cs}} \times N_{\mathrm{cp}}$ array of series–parallel connected PV cells
P_d	Junction box dissipated power (W)
$\mathcal{P}_{\mathrm{diode}}$	$N_{\mathrm{ds}} \times N_{\mathrm{dp}}$ array of series–parallel connected BPD
$\mathcal{P}_{\mathrm{panel}}$	series connected $\mathcal{P}_{\mathrm{block}}$
R_{ds}	Diode series resistance (Ω)
R_p	Cell shunt resistance (Ω)
R_s	Cell series resistance (Ω)
R_{s0}	BPD reference series resistance (Ω)
$\mathrm{R}_{\theta\mathrm{ab}}$	Surrounding air–junction box radiation and convection thermal resistance (Ω)
$\mathrm{R}_{\theta\mathrm{bair}}$	Junction box conduction thermal resistance (Ω)
$\mathrm{R}_{\theta\mathrm{air}}$	Air enclosed on junction box equivalent thermal resistance (Ω)
$\mathrm{R}_{\theta\mathrm{cj}}$	Junction case conduction thermal resistance (Ω)
T	Cell temperature (K)
T_a	Ambient temperature (K)
T_{bs}	PV panel back–surface temperature (K)
T_j	Junction temperature (K)
T_0	BPD reference junction temperature (K)
V_{cloud}	Cloud speed (m/s)
$V_{\mathcal{P}\mathrm{array}}$	Terminal voltage of $\mathcal{P}_{\mathrm{array}}$ (V)
$V_{\mathcal{P}\mathrm{cell}}$	Terminal voltage of $\mathcal{P}_{\mathrm{cell}}$ (V)
$V_{\mathcal{P}\mathrm{diode}}$	Terminal voltage of $\mathcal{P}_{\mathrm{diode}}$ (V)
$V_{\mathcal{P}\mathrm{panel}}$	Terminal voltage of $\mathcal{P}_{\mathrm{panel}}$ (V)
$V_{\mathcal{P}\mathrm{section}}$	Terminal voltage of $\mathcal{P}_{\mathrm{block}}$ (V)
V_w	Wind speed measured at standard 10 m height (m/s)
α	Characteristic fitting parameter of a given semiconductor material (eV/K)
β	Characteristic fitting parameter of a given semiconductor material (K)
α'_t	Relative temperature coefficient of short–circuit current (%/°C)
ΔT	Difference between T and T_{bs} at G of 1000 $\mathrm{W/m}^2$ (276.15 K)
Φ_{b0}	Schottky barrier height (eV)
a	Upper limit for panel temperature at low V_w and high G (-3.47)
b	Rate at which panel temperature drops as V_w increases (-0.0594)
d	Distance between solar collectors (m)
k	Boltzamnn's constant ($1.3806503 \times 10^{-23}$ J/K)
n	PV cell ideality factor
n_b	BPD ideality factor
n_0	BPD reference ideality factor
q	Electron's electric charge (1.602×10^{-19} C)
$_{\mathrm{ref}}$	Reference value

electric models for both a single PV cell as well as a BPD. Thermal effects are incorporated accounting for solar irradiance, wind speed, and ambient temperature. Based on actual PV system architecture, the model is built to characterize any size array of PV cells.

The modeling procedure begins by defining the following two building blocks. Let

$\mathcal{P}_{\text{cell}}$ be a $N_{\text{cs}} \times N_{\text{cp}}$ array of series and parallel–connected PV cells. Similarly, let $\mathcal{P}_{\text{diode}}$ be a $N_{\text{ds}} \times N_{\text{dp}}$ array of series and parallel–connected BPD. The letter $\mathcal{P}$ is chosen to highlight the fact that each of these arrays are "partitions" of a larger structure. When these building blocks are parallel connected, they give rise to a third partition of PV panels depicted in Fig. 5.1(a), termed as $\mathcal{P}_{\text{block}}$. A PV panel partition, termed $\mathcal{P}_{\text{panel}}$, is obtained by connecting in series a number of $\mathcal{P}_{\text{blocks}}$ and it is shown in Fig. 5.1(b). In the same fashion, an aggregation in series and in parallel of $N_{\text{ps}} \times N_{\text{pp}}$ panels yields to a PV array representation termed $\mathcal{P}_{\text{array}}$ illustrated in Fig. 5.1(c). A $\mathcal{P}_{\text{array}}$ is thus any size array of PV panels that may represent an entire PV power plant or a section of it, preserving both the inner structure and also modeling details of its inner blocks. Fig. 5.1, shows the various partitions comprising the array. The figure specifically uses the PV panel Kyocera KC85TS as an example. The panel is built using three series–connected $\mathcal{P}_{\text{block}}$, with each block comprised of a 12×2 $\mathcal{P}_{\text{cell}}$ connected in parallel with 1×3 $\mathcal{P}_{\text{diode}}$.

5.2.2 Thermoelectric model of $\mathcal{P}_{\text{cell}}$

This section develops a thermoelectric model of any size array of $N_{\text{cs}} \times N_{\text{cp}}$ series–parallel connected PV cells.

5.2.2.1 Electrical model of $\mathcal{P}_{\text{cell}}$

The circuital model for $\mathcal{P}_{\text{cell}}$ proposed by [30], is established from a current source, an anti–parallel diode modeled by a controlled current source, a series and also a shunt resistance. One key advantage of this model is that any size array of any number of cells connected in series and parallel depicted in Fig. 5.2(a), can be modeled through a single equivalent circuit. This circuit is illustrated in the top section of Fig. 5.2(b). In this figure and throughout the rest of this work, continuous blue lines are used to indicate measurements, whereas dashed blue lines represent signals used to drive controlled sources. Simple circuit analysis leads to the following transcendental equation relating the total output current $I_{\mathcal{P}_{\text{cell}}}$ and terminal voltage $V_{\mathcal{P}_{\text{cell}}}$,

(a) $\mathcal{P}_{\text{block}}$ (b) $\mathcal{P}_{\text{panel}}$

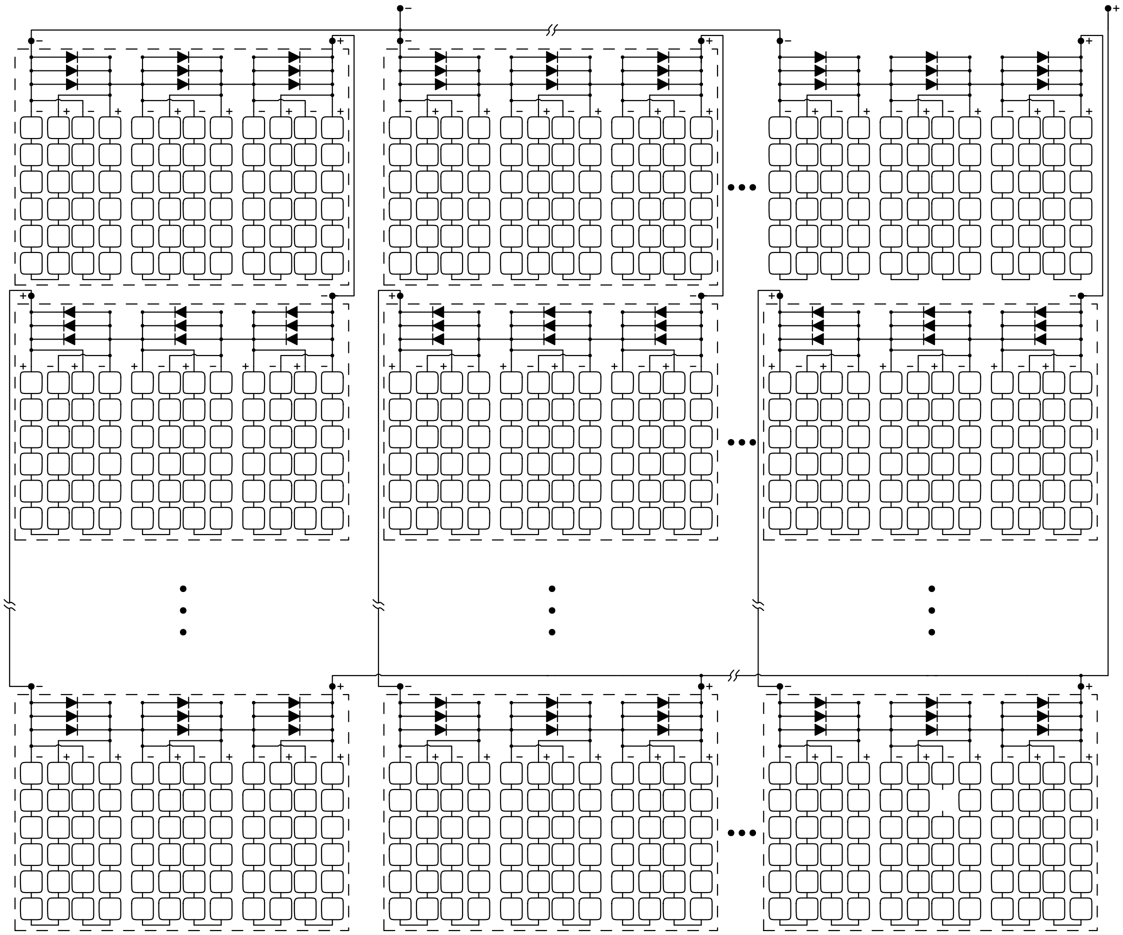

(c) $\mathcal{P}_{\text{array}}$

Figure 5.1: Construction of $\mathcal{P}_{\text{array}}$ from partitions $\mathcal{P}_{\text{cell}}$, $\mathcal{P}_{\text{diode}}$, $\mathcal{P}_{\text{block}}$ and $\mathcal{P}_{\text{panel}}$ using the Kyocera KC85TS PV panel as an example.

$$I_{\mathcal{P}_{\text{cell}}} = I'_{\text{irr}} - I'_0 \left[\exp\left(\frac{q\left(V_{\mathcal{P}_{\text{cell}}} + I_{\mathcal{P}_{\text{cell}}} R'_{\text{s}}\right)}{N_{\text{cs}} \text{n} k T} \right) - 1 \right] - \frac{V_{\mathcal{P}_{\text{cell}}} + I_{\mathcal{P}_{\text{cell}}} R'_{\text{s}}}{R'_{\text{p}}}. \tag{5.1}$$

In (5.1), q is the electron charge ($q = 1.602 \times 10^{-19}$ C), n is the ideality factor of the PV cells, k is the Boltzmann constant ($k = 1.3806503\ 10^{-23}$ J/K), and T stands for PV cell temperature. The various "prime" accounts for the series–parallel aggregation, and are related to their single–cell counterparts according to $I'_{\mathrm{irr}} = N_{\mathrm{cp}} I_{\mathrm{irr}}$; $I'_0 = N_{\mathrm{cp}} I_0$; $R'_{\mathrm{p}} = \frac{N_{\mathrm{cs}}}{N_{\mathrm{cp}}} R_{\mathrm{p}}$; and $R'_{\mathrm{s}} = \frac{N_{\mathrm{cs}}}{N_{\mathrm{cp}}} R_{\mathrm{s}}$. I_{irr} is the photo current, which is generated when the cell is exposed to solar irradiance, G. I_0 is the cell saturation current, and R_{s} and R_{p} represent the series and shunt resistance, respectively. The parameters I_{irr}, I_0, R_{s} and R_{p} depend on G and T, as well as on some reference parameters,

$$I_{\mathrm{irr}} = I_{\mathrm{irr,ref}} \frac{G}{G_{\mathrm{ref}}} \left[1 + \alpha'_{\mathrm{t}}(T - T_{\mathrm{ref}})\right], \tag{5.2}$$

$$I_0 = I_{0,\mathrm{ref}} \left(\frac{T}{T_{\mathrm{ref}}}\right)^3 \exp\left(\frac{E_{\mathrm{g,ref}}}{kT_{\mathrm{ref}}} - \frac{E_{\mathrm{g}}}{kT}\right), \tag{5.3}$$

$$R_{\mathrm{p}} = R_{\mathrm{p,ref}} \left(\frac{G}{G_{\mathrm{ref}}}\right), \tag{5.4}$$

$$R_{\mathrm{s}} = R_{\mathrm{s,ref}}, \tag{5.5}$$

$$\mathrm{n} = \mathrm{n}_{\mathrm{ref}}. \tag{5.6}$$

In (5.2), α'_{t} is the absolute temperature coefficient of the cell short–circuit current, which represents the rate of change of the short–circuit current with respect to T. In (5.3), E_{g} is the bandgap energy for silicon in (eV) and may be computed as:

$$E_{\mathrm{g}} = 1.17 - 4.73 \times 10^{-4} \frac{T^2}{T + 636}. \tag{5.7}$$

The parameters of the single–diode PV model can be extracted from manufacturer's datasheets [56],[49]. Alternatively, several authors have also proposed methodologies for extracting the five–parameter model based on experimental measurements representing the I–V curves; see for instance [57] and references within. A different method to extract the five–parameter model was proposed by [58]. The parameters were determined using the PV panel manufacturer's datasheet, as well as a single experimental measurement of the shunt resistance. According to the authors, measurement errors of the shunt resistance do not affect the values of the calculated parameters.

5.2.2.2 Thermal model of $\mathcal{P}_{\text{cell}}$

It may be observed the circuital model described in the top section of Fig. 5.2(b), depends on the PV cell temperature T as illustrated in the bottom section of Fig. 5.2(b). Since T, may not be directly available for measurement, several authors have developed expressions for determining T based in the ambient temperature, wind speed and also solar irradiance. From here forward we use the equation from [44],

$$T_{\text{bs}} = G \exp\left(a + bV_{\text{w}}\right) + T_{\text{a}}, \tag{5.8}$$

$$T = T_{\text{bs}} + \frac{G}{G_0}\Delta T, \tag{5.9}$$

where T_{bs} and T_{a}, are, respectively, the PV cell back–surface and ambient temperature, and V_{w} represents the wind speed. The coefficients a, b, and ΔT are empirically determined, taking into account the PV panel type and mounting characteristics. The upper limit for the panel temperature, experienced at low wind speeds and high irradiance, is represented by a. The rate at which the panel temperature drops as the wind speed increases are indicated by b and the temperature difference between the cell and the panel back–surface at an irradiance level of 1000 W/m^2 is represented by ΔT [44].

5.2.2.3 Unified model of $\mathcal{P}_{\text{cell}}$

A unified representation for the partition $\mathcal{P}_{\text{cell}}$ is depicted in Fig. 5.2(b), where the integration of the thermal and electric models is shown.

5.2.3 Thermoelectric model of $\mathcal{P}_{\text{diode}}$

The electrical model used, from a single diode, is well established by the Shockley equation [59]. This subsection describes the model and proposes a simplified thermal model for a BPD, taking into account the junction box temperature dynamics. The electric and thermal models are then unified and generalized, to account of an array of $N_{\text{ds}} \times N_{\text{dp}}$ BPDs.

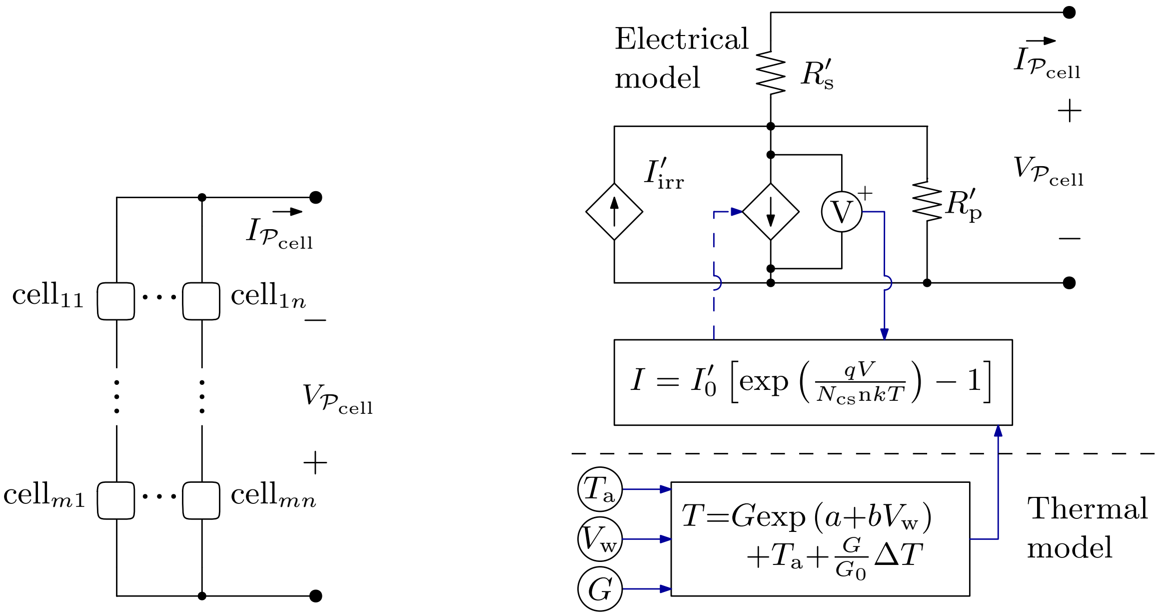

(a) (b)

Figure 5.2: (a) an array of PV cells, (b) its equivalent thermoelectric model $\mathcal{P}_{\mathrm{cell}}$.

5.2.3.1 Electrical model of a single BPD

The Shockley diode equation is defined by [59] as follows:

$$I_{\mathrm{BPD}} = I_{\mathrm{b0}} \left[\exp\left(\frac{q(V_{\mathrm{BPD}} - I_{\mathrm{BPD}} R_{\mathrm{ds}})}{\mathrm{n_b} k T_{\mathrm{j}}}\right) - 1\right], \tag{5.10}$$

where I_{BPD} is the diode's current, V_{BPD} is the voltage across the diode, $\mathrm{n_b}$ is the ideality factor of the diode, T_{j} is the junction temperature and R_{ds} is the diode's series resistance and, I_{b0} is the diode saturation current and it can be obtained from (5.11) following the procedure presented in [60],

$$I_{\mathrm{b0}} = AA^* T_{\mathrm{j}}^2 \exp\left(-\frac{q\Phi_{\mathrm{b0}}}{kT_{\mathrm{j}}}\right), \tag{5.11}$$

where Φ_{b0} is the Schottky barrier height, A^* is the effective Richardson constant and equals to 112 $\mathrm{Acm^{-2}K^{-2}}$ [61] and, A is the diode's cross section area.

Notice, $\mathrm{n_b}$, R_{ds} and Φ_{b0} BPD parameters vary due to their heat transfer phenomena. In the next subsection, mathematical expressions are reviewed in order to take into account these variations.

5.2.3.2 Thermal model of a single BPD

Analytical expressions for the ideality factor and the diode's series resistance are typically obtained through curve fitting from experimental measurements. Herein the ideality factor, diode's series resistance, and Schottky barrier height are obtained by following the procedure in [60], [59] and [62] in conjunction with the manufacturers' datasheet.

Researchers have found that the ideality factor, the series resistance, the Schottky barrier height and their dependencies formulation as a function of T_{j} can be expressed as follows:

$$\mathrm{n_b}(T_{\mathrm{j}}) = n_0 + \frac{T_0}{T_{\mathrm{j}}}, \tag{5.12}$$

$$R_{\mathrm{ds}}(T_{\mathrm{j}}) = R_{\mathrm{s0}} \exp\left(\frac{E_{\mathrm{a}}}{kT_{\mathrm{j}}}\right), \tag{5.13}$$

$$\Phi_{\mathrm{b0}}(T_{\mathrm{j}}) = E_0 - \alpha \frac{T_{\mathrm{j}}^2}{T_{\mathrm{j}} + \beta}, \tag{5.14}$$

where n_0 and T_0 are constants, and can be obtained from the linear fitting of the plot of ideality factor versus inverse temperature [60], E_{a} is the dopant activation energy, R_{s0} is a constant [63], E_0 computed at 0 K, α and β are the characteristic fitting parameters of a given material [62].

5.2.4 Unified model of $\mathcal{P}_{\mathrm{diode}}$

Consider any number of identical series connected diodes. In this case the total output voltage across the equivalent diode will be the sum of the voltages across each of the identical series connected diodes. Furthermore, the current flowing through each of the diodes must be equal. Its mathematical equation is described by (5.15),

$$I_{\mathrm{BPDs}} = I_{\mathrm{b0}} \left[\exp\left(\frac{q\left(V_{\mathrm{BPDs}} - I_{\mathrm{BPDs}} R_{\mathrm{ds}} N_{\mathrm{ds}}\right)}{N_{\mathrm{ds}} \mathrm{n_b} k T_{\mathrm{j}}}\right) - 1\right], \tag{5.15}$$

where V_{BPDs} is the voltage across the equivalent diode (V).

Now, consider any number of identical parallel–connected strings of diodes. Under these circumstances, the voltage across each of the diodes must be the same. Therefore, the parallel connected diodes can be modeled as follows:

$$I_{\mathrm{BPDp}} = N_{\mathrm{dp}} I_{\mathrm{b0}} \left[\exp\left(\frac{q\left(V_{\mathrm{BPDp}} - I_{\mathrm{BPDp}} \frac{R_{\mathrm{ds}}}{N_{\mathrm{dp}}}\right)}{\mathrm{n_b} k T_{\mathrm{j}}} \right) - 1 \right]. \tag{5.16}$$

Finally, since any number of identical parallel connected strings of diodes will increase the output current, (5.15) can be rewritten as,

$$I_{\mathcal{P}_{\mathrm{diode}}} = N_{\mathrm{dp}} I_{\mathrm{b0}} \left[\exp\left(\frac{q\left(V_{\mathcal{P}_{\mathrm{diode}}} - I_{\mathcal{P}_{\mathrm{diode}}} R_{\mathrm{ds}} \frac{N_{\mathrm{ds}}}{N_{\mathrm{dp}}}\right)}{N_{\mathrm{ds}} \mathrm{n_b} k T_{\mathrm{j}}} \right) - 1 \right], \tag{5.17}$$

which is an equation of a single BPD, in any size array, connected in series and in parallel. Any size array of BPDs connected in series and in parallel is depicted in Fig. 5.3(a), whereas its equivalent thermoelectric circuit is shown in Fig. 5.3(b). The model expressed by (5.17), is considered a second building block termed $\mathcal{P}_{\mathrm{diode}}$. These values for the reference parameters can be obtained experimentally or can also be extracted by following the procedure in [61] coupled with the manufacturer datasheet.

Notice that the BPD junction temperature T_{j} is subjected to variations due to its dissipated power P_{d}, fluctuations in ambient temperature and characteristics of the PV panel junction box. These junction box characteristics can include material, geometry and its specific location. The next subsection proposes an equivalent thermal circuit that accounts for these variations.

5.2.5 Thermal model of the BPD junction box

This section details how the thermal model for the BPD junction box was developed. Factors taken into consideration include operating conditions, environmental

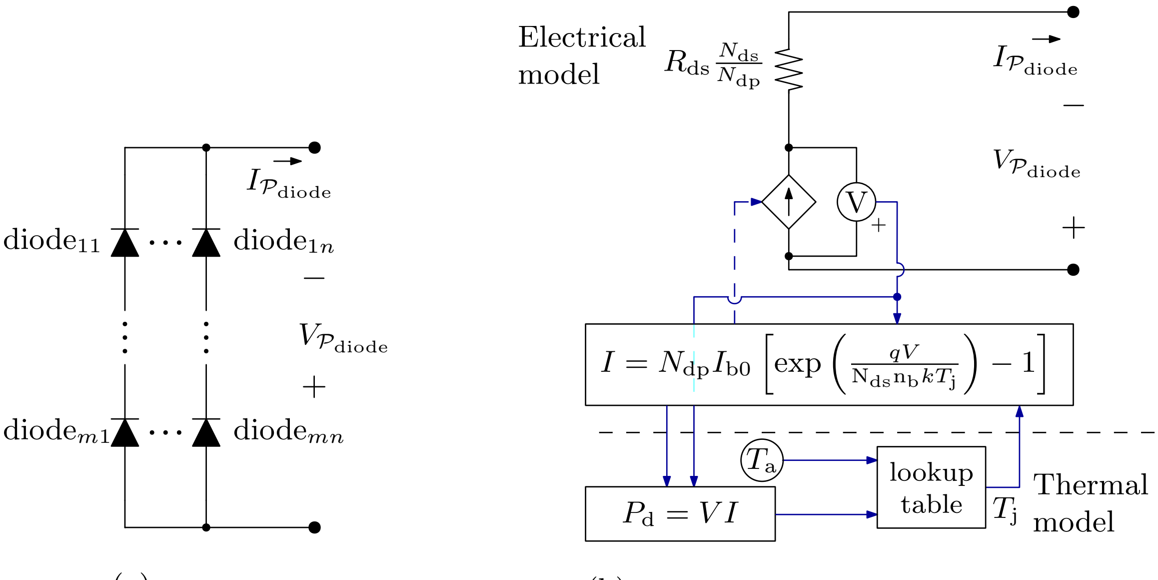

(a) (b)

Figure 5.3: (a) an array of BPD, (b) its equivalent thermoelectric model $\mathcal{P}_{\text{diode}}$.

conditions, the physical arrangement inside of the enclosure, dimensions of the enclosure, and the materials that comprise these elements. This section highlights first how the proposed model was developed, then how an independent experiment was conducted and finally how the proposed model compares to the independent experimental results.

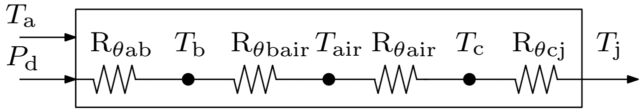

Figure 5.4: Equivalent junction box thermal model.

5.2.5.1 Estimation of BPD T_{j} considering its junction box physical properties and thermal effects

Modeling approaches for the conduction, convection, and radiation phenomena are described in depth in [64]. These are considered in order to obtain a thermal model for an equivalent BPD and its junction box. By taking into account the material of the junction box and the air enclosed on it, equivalent conduction and convection thermal resistances are modeled following the Fourier's law and Newton's law of cooling using the Rayleigh–Bénard procedure. Individual thermal resistances and corresponding BPD losses are combined into an equivalent and simplified model depicted in Fig. 5.4. There, $\mathrm{R}_{\theta \mathrm{ab}}$ represents radiation and convection thermal resistance between the junction box and the surrounding air. $\mathrm{R}_{\theta \mathrm{bair}}$ stands for conduction thermal resistance of the junction box and $\mathrm{R}_{\theta \mathrm{air}}$ expresses a Rayleight–Bénard equivalent thermal resistance of the air enclosed in the box. Finally, $\mathrm{R}_{\theta \mathrm{cj}}$ accounts for the junction–case conduction thermal resistance. Now, with the summation of $\mathrm{R}_{\theta \mathrm{ab}}$, $\mathrm{R}_{\theta \mathrm{bair}}$, $\mathrm{R}_{\theta \mathrm{air}}$ and $\mathrm{R}_{\theta \mathrm{cj}}$ we get $\mathrm{R}_{\theta \mathrm{eq}}$, which is the total thermal resistance between T_{a} and T_{j}. However, due to the calculations of T_{j} involving non–linear relations, these cannot be performed online. These non–linear relations include the buoyancy–driven flow of the air, heated from different directions resulting in non–linear and chaotic dynamics, which must be taken into account by the Rayleigh–Bénard procedure. To overcome this situation, the BPD and junction box thermal model can be solved offline by using the numerical solvers available in standard software platforms such as Matlab.

In this work, the proposed thermal model for BPD and junction box was implemented on a Matlab script. First, operating ranges for ambient temperature $T_{\mathrm{a}}(k)$ and dissipated power $P_{\mathrm{d}}(k)$ was selected according to nominal operational conditions, where $k \in \{1, 2..s\}$ with s accounting for the number of step changes in T_{a} and P_{d}. Second, the number of BPDs, their dimensions, and their thermal parameters were considered. Third, junction box geometry, convection surfaces and the material's coefficient of conductivity were obtained. Fourth, $T_{\mathrm{a}}(k)$, $P_{\mathrm{d}}(k)$, along with the calculated BPDs and junction box parameters were entered into a function where the nonlinear thermal model shown in Fig. 5.4 is solved and the BPD junction temperature $T_{\mathrm{j}}(k)$ is obtained. $T_{\mathrm{j}}(k){=}T_{\mathrm{a}}(k){+}P_{\mathrm{d}}(k) \times \{\mathrm{R}_{\theta \mathrm{ab}}(k) + \mathrm{R}_{\theta \mathrm{bair}}(k) + \mathrm{R}_{\theta \mathrm{air}}(k) + \mathrm{R}_{\theta \mathrm{cj}}(k)\}$. Fifth, the lookup table in row $(k){=}[T_{\mathrm{a}}(k), P_{\mathrm{d}}(k), T_{\mathrm{j}}(k)]$ was updated. Six, this process continues iterating until $k = s$. In this work, the lookup table was generated offline. The lookup table is storing T_{j} data, assuming a large PV plant has been built, and it is performing under nominal operating conditions. This lookup table will output T_j when fed by P_d and T_a during simulation time. An extraction of this lookup table is shown in Table 5.1.

Table 5.1: Illustration of the lookup table

T_a (°C)	P_d (W)	T_j (°C)
20	1.00	45.39
20	2.00	65.60
20	3.00	84.14
20	4.00	101.60
20	5.00	118.40
⋮	⋮	⋮
80	8.00	222.30
80	9.00	236.50
80	10.00	250.50

5.2.5.2 Estimation of BPD T_j considering junction box experimental results

To provide validation for the proposed model, the following is an independent experimental approach to determine BPD junction temperature T_j by [65]. Here the authors studied BPD reliability, when experiencing high temperatures and thermal cycling under controlled testing conditions. Forward diode voltage V_fd and case temperature T_c where experimentally measured. Additionally, the authors set a constant diode forward current $I_\mathrm{fd} = 10$ A for 1000 hours. With this, $P_\mathrm{d} = V_\mathrm{fd} \times I_\mathrm{fd}$ can be easily estimated.

In order to utilize the experimental results of [65], to determine T_j, the following assumptions have been made: *(i)* the authors connected a bypass diode VT2045BP package TO–220AC so that $\mathrm{R}_{\theta\mathrm{jc}} = 1.5$ °C/W is known, *(ii)* junction box dimensions

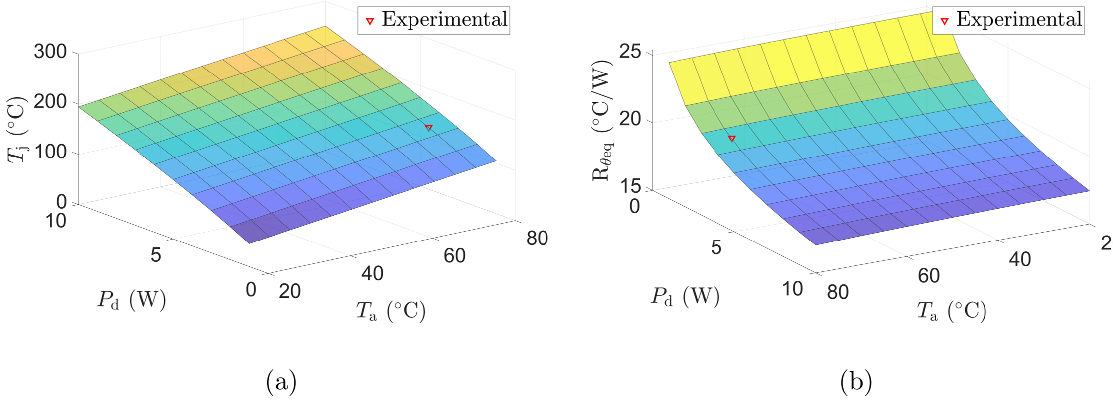

Figure 5.5: (a) Comparison of experimental and proposed model values for T_{j}, (b) nonlinear surface of $\mathrm{R}_{\theta\mathrm{eq}}$.

have been extracted from the information provided in [65], and *(iii)* average measured values for V_{fd} and T_{c} have been used. Finally, $T_{\mathrm{j,experimental}}$ can be approximated by (5.18),

$$T_{\mathrm{j,experimental}} = T_{\mathrm{c,experimental}} + R_{\theta\mathrm{jc}} \times P_{\mathrm{d,experimental}}. \tag{5.18}$$

5.2.5.3 Comparison of modeled vs experimental results of BPD T_{j}

This section compares the adjusted proposed model to the experimental results from [35]. Let $T_{\mathrm{j,model}}$ stand for the proposed approach, which is based on the BPDs' junction box physical properties and thermal effects to estimate T_{j}. Similarly, let $T_{\mathrm{j,experimental}}$ stand for real estimation of T_{j}, according to the setup presented in [35]. The surface of Fig. 5.5(a) shows the results of $T_{\mathrm{j,model}}$ and the single highlighted point shows the result of $T_{\mathrm{j,experimental}}$. Here, making use of the standard software platform Matlab, both approaches were compared. According to Fig. 5.5(a), both approaches produced a similar estimation of T_{j}. Comparing just the operating point of the experimental result gives $T_{\mathrm{j,experimental}} = 146.73$ °C and $T_{\mathrm{j,model}} = 146.44$ °C.

It is important to note that since our model is nonlinear, shown in Fig. 5.5(b), the thermal resistance $\mathrm{R}_{\theta \mathrm{eq}}$ is a function of the operating point of the system (T_a and P_d).

5.2.6 Model of $\mathcal{P}_\mathrm{block}$

An equivalent circuit of an array of $N_\mathrm{cs} \times N_\mathrm{cp}$ cells in parallel with an equivalent circuit of an array of $N_\mathrm{ds} \times N_\mathrm{dp}$ BPD, can be modeled by including (5.17) into the model proposed by [30]. It is a combination of the two previous building blocks $\mathcal{P}_\mathrm{cell}$ and $\mathcal{P}_\mathrm{diode}$. Its name is defined as $\mathcal{P}_\mathrm{block}$ and is depicted in Fig. 5.6. This approach introduces a thermoelectric modular model representing a PV panel section.

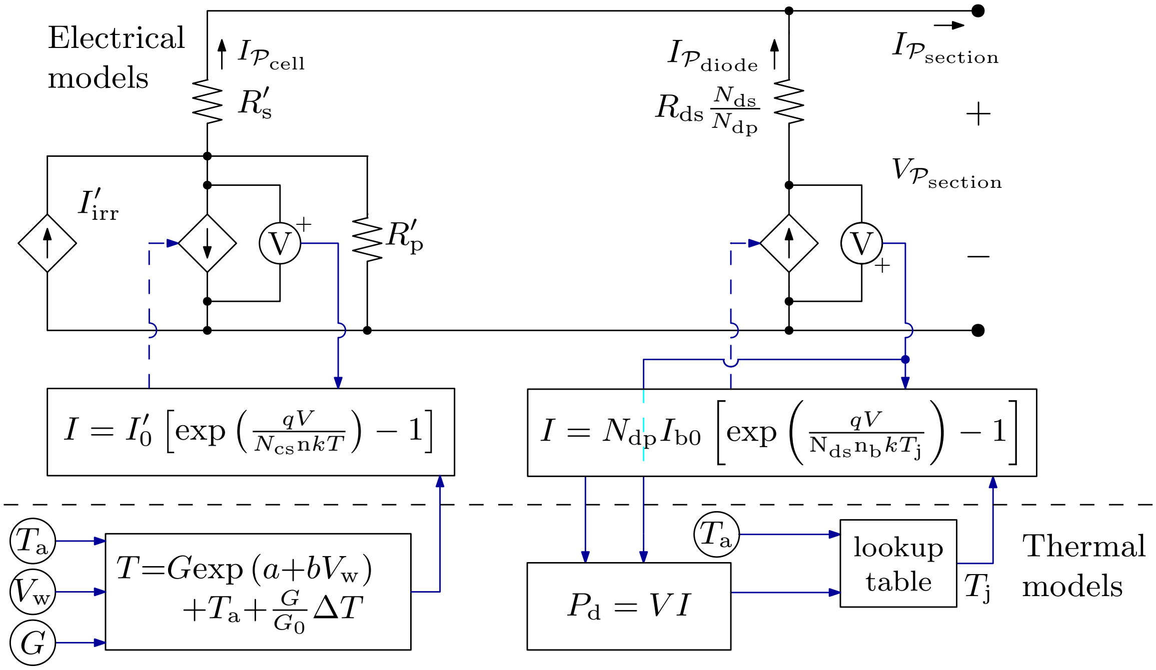

Figure 5.6: Proposed thermoelectric modular model of a PV panel section identified as $\mathcal{P}_\mathrm{block}$.

The total output current, as shown in Fig. 5.6, can be expressed as:

$$I_{\mathcal{P}_\mathrm{section}} = I_{\mathcal{P}_\mathrm{cell}} + I_{\mathcal{P}_\mathrm{diode}}, \tag{5.19}$$

where, $I_{\mathcal{P}_\mathrm{cell}}$ and $I_{\mathcal{P}_\mathrm{diode}}$, are defined by (5.1) and (5.17) respectively. Hence, (5.19) can be reexpressed as a function of $I_{\mathcal{P}_{\text{section}}}$ and $V_{\mathcal{P}_{\text{section}}}$ as:

$$\begin{aligned} I_{\mathcal{P}_{\text{section}}} =& I'_{\text{irr}} - I'_0 \left[\exp\left(\frac{q\left(V_{\mathcal{P}_{\text{section}}} + (I_{\mathcal{P}_{\text{section}}} - I_{\mathcal{P}_{\text{diode}}})R'_{\text{s}}\right)}{N_{\text{cs}}\text{n}kT}\right) - 1\right] \\ &- \frac{V_{\mathcal{P}_{\text{section}}} + (I_{\mathcal{P}_{\text{section}}} - I_{\mathcal{P}_{\text{diode}}})R'_{\text{s}}}{R'_{\text{p}}} + I_{\mathcal{P}_{\text{diode}}}, \\ I_{\mathcal{P}_{\text{diode}}} =& N_{\text{dp}} I_{\text{b0}} \left[\exp\left(\frac{q\left(V_{\mathcal{P}_{\text{section}}} - I_{\mathcal{P}_{\text{diode}}} R_{\text{ds}} \frac{N_{\text{ds}}}{N_{\text{dp}}}\right)}{N_{\text{ds}}\text{n}_{\text{b}} k T_{\text{j}}}\right) - 1\right]. \end{aligned} \tag{5.20}$$

5.2.7 Model of $\mathcal{P}_{\text{panel}}$

Based on the presented approach, a complete PV panel is made up of a number of series–connected PV sections N_{ss}. The total output voltage across a single equivalent BPD of a PV panel will be the aggregation of each voltage $V_{\mathcal{P}_{\text{diode}}}$ measured across each single equivalent BPD standing for a PV section. It is assumed the whole PV panel is subjected to the same G and T_{a}. As a result, (5.17) can be rewritten as follows:

$$I_{\mathcal{P}_{\text{diode}}} = N_{\text{dp}} I_{\text{b0}} \left[\exp\left(\frac{q\left(V_{\mathcal{P}_{\text{panel}}} - I_{\mathcal{P}_{\text{diode}}} R_{\text{ds}} N_{\text{ss}} \frac{N_{\text{ds}}}{N_{\text{dp}}}\right)}{N_{\text{ss}} N_{\text{ds}} \text{n}_{\text{b}} k T_{\text{j}}}\right) - 1\right], \tag{5.21}$$

where $V_{\mathcal{P}_{\text{panel}}} = N_{\text{ss}} V_{\mathcal{P}_{\text{diode}}}$, is the voltage across the single equivalent BPD of a PV panel. Moreover, let $N_{\text{dp}} I_{\text{b0}}$, $N_{\text{ss}} N_{\text{ds}} \text{n}_{\text{b}}$ and $R_{\text{ds}} N_{\text{ss}} \frac{N_{\text{ds}}}{N_{\text{dp}}}$ be defined by I'_{b0}, n'_{b} and R'_{ds} respectively. Thus, (5.21) can be rewritten as:

$$I_{\mathcal{P}_{\text{diode}}} = I'_{\text{b0}} \left[\exp\left(\frac{q\left(V_{\mathcal{P}_{\text{panel}}} - I_{\mathcal{P}_{\text{diode}}} R'_{\text{ds}}\right)}{\text{n}'_{\text{b}} k T_{\text{j}}}\right) - 1\right]. \tag{5.22}$$

Furthermore, (5.1) needs to be rewritten to take into account the total number of sections N_{ss} making up a PV panel. Hence, the output current of the any number of cells comprised over a PV panel is calculated as:

$$I_{\mathcal{P}_{\text{cell}}} = I'_{\text{irr}} - I'_0 \left[\exp\left(\frac{q\left(V_{\mathcal{P}_{\text{panel}}} + I_{\mathcal{P}_{\text{cell}}} N_{\text{ss}} R'_{\text{s}}\right)}{N_{\text{ss}} N_{\text{cs}} \text{n} k T} \right) - 1 \right] - \frac{V_{\mathcal{P}_{\text{panel}}} + I_{\mathcal{P}_{\text{cell}}} N_{\text{ss}} R'_{\text{s}}}{N_{\text{ss}} R'_{\text{p}}}. \tag{5.23}$$

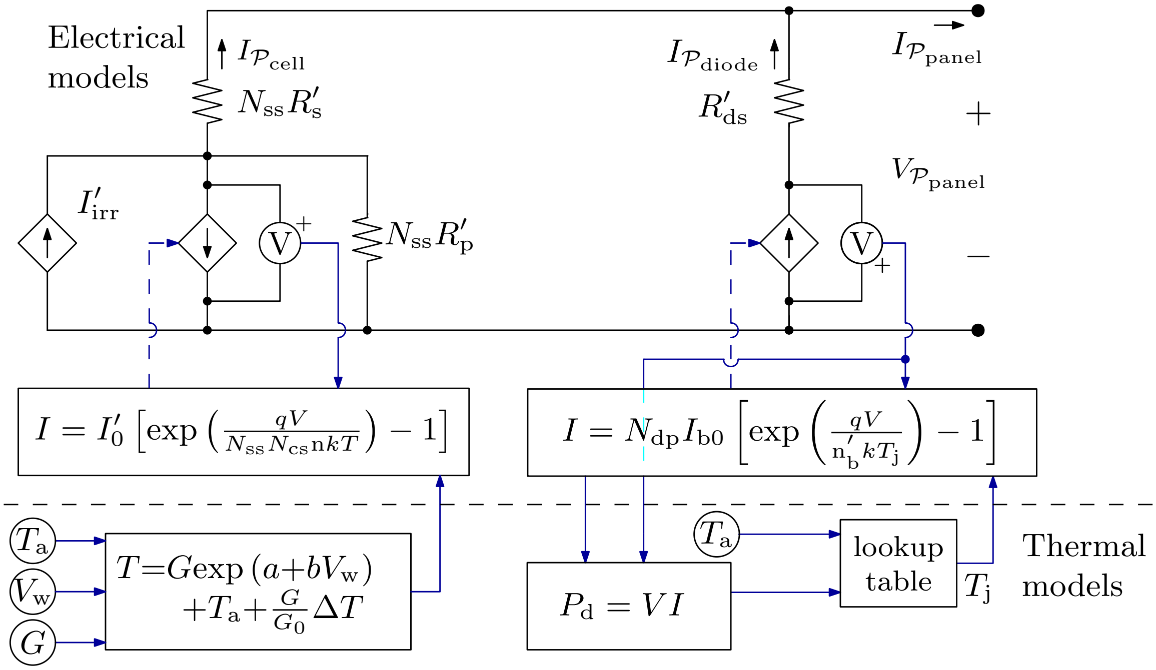

Figure 5.7: Improved PV panel representation, named as $\mathcal{P}_{\text{panel}}$.

An improved representation, that can effectively characterize any number of $\mathcal{P}_{\text{blocks}}$ conforming a PV panel, is depicted in Fig. 5.7, which in turn is termed as $\mathcal{P}_{\text{panel}}$. As it is shown, the total output current can be obtained as:

$$I_{\mathcal{P}_{\text{panel}}} = I_{\mathcal{P}_{\text{cell}}} + I_{\mathcal{P}_{\text{diode}}}, \tag{5.24}$$

where, $I_{\mathcal{P}_{\text{diode}}}$ and $I_{\mathcal{P}_{\text{cell}}}$ are defined by (5.22) and (5.23) respectively. Thus, (5.24) can be rewritten as a function of $I_{\mathcal{P}_{\text{panel}}}$ and $V_{\mathcal{P}_{\text{panel}}}$ as follows:

$$\begin{aligned}
I_{\mathcal{P}_{\text{panel}}} =& I'_{\text{irr}} - I'_0 \left[\exp\left(\frac{q\left(V_{\mathcal{P}_{\text{panel}}} + (I_{\mathcal{P}_{\text{panel}}} - I_{\mathcal{P}_{\text{diode}}}) N_{\text{ss}} R'_s\right)}{N_{\text{ss}} N_{\text{cs}} \text{n} k T} \right) - 1 \right] \\
& - \frac{V_{\mathcal{P}_{\text{panel}}} + (I_{\mathcal{P}_{\text{panel}}} - I_{\mathcal{P}_{\text{diode}}}) N_{\text{ss}} R'_s}{N_{\text{ss}} R'_p} + I_{\mathcal{P}_{\text{diode}}}, \\
I_{\mathcal{P}_{\text{diode}}} =& I'_{\text{b0}} \left[\exp\left(\frac{q\left(V_{\mathcal{P}_{\text{panel}}} - I_{\mathcal{P}_{\text{diode}}} R'_{\text{ds}}\right)}{\text{n}'_{\text{b}} k T_{\text{j}}} \right) - 1 \right].
\end{aligned} \tag{5.25}$$

The mathematical expression indicated in (5.25), is an equivalent representation of a PV panel $\mathcal{P}_{\text{panel}}$, which includes the effects of any number of series–connected PV sections $\mathcal{P}_{\text{block}}$.

5.2.8 Model of $\mathcal{P}_{\text{array}}$

A PV system is made up of both series and parallel connections of PV panels. Whereas a series connected PV panel will increase the total output voltage, a parallel connected PV panel will increase the total output current. Thus, (5.22) and (5.23) must be rewritten, since it is necessary to consider any number of PV panels connected in series and in parallel. Let N_{pp} and N_{ps} be defined as the number of PV panels connected in parallel and series respectively. Since the total output current is directly proportional to the number of PV panels connected in parallel, I'_{irr}, I'_0, I'_{b0} can be rewritten as a function of N_{pp} as follows: $I''_{\text{irr}} = N_{\text{pp}} I'_{\text{irr}}$; $I''_0 = N_{\text{pp}} I'_0$; $I''_{\text{b0}} = N_{\text{pp}} I'_{\text{b0}}$. Similarly, $\text{n}_{\text{b}}{}'$ and $N_{\text{ss}} N_{\text{cs}} \text{n}$ can be expressed as a function of N_{ps} as follows: $\text{n}' = N_{\text{ps}} N_{\text{ss}} N_{\text{cs}} \text{n}$; $\text{n}_{\text{b}}{}'' = N_{\text{ps}} \text{n}'_{\text{b}}$. Finally, $N_{\text{ss}} R'_{\text{s}}$, $N_{\text{ss}} R'_{\text{p}}$ and R'_{ds} can be rewritten as a function of the ratio between N_{ps} and N_{pp} as: $R''_{\text{s}} = (N_{\text{ps}}/N_{\text{pp}}) N_{\text{ss}} R'_{\text{s}}$; $R''_{\text{p}} = (N_{\text{ps}}/N_{\text{pp}}) N_{\text{ss}} R'_{\text{p}}$ and $R''_{\text{ds}} = (N_{\text{ps}}/N_{\text{pp}}) R'_{\text{ds}}$. As a result, (5.25) can be rewritten as in (5.26) and it is illustrated in Fig. 5.8.

$$\begin{aligned} I_{\mathcal{P}_\text{array}} =& I''_\text{irr} - I''_0\left[\exp\left(\frac{q\left(V_{\mathcal{P}_\text{array}} + (I_{\mathcal{P}_\text{array}} - I_{\mathcal{P}_\text{diode}})R''_s\right)}{\text{n}'kT}\right)-1\right] \\ &- \frac{V_{\mathcal{P}_\text{array}} + (I_{\mathcal{P}_\text{array}} - I_{\mathcal{P}_\text{diode}})R''_s}{R''_p} + I_{\mathcal{P}_\text{diode}}, \\ I_{\mathcal{P}_\text{diode}} =& I''_\text{b0}\left[\exp\left(\frac{q\left(V_{\mathcal{P}_\text{array}} - I_{\mathcal{P}_\text{diode}}R''_\text{ds}\right)}{\text{n}''_\text{b}kT_\text{j}}\right)-1\right]. \end{aligned} \tag{5.26}$$

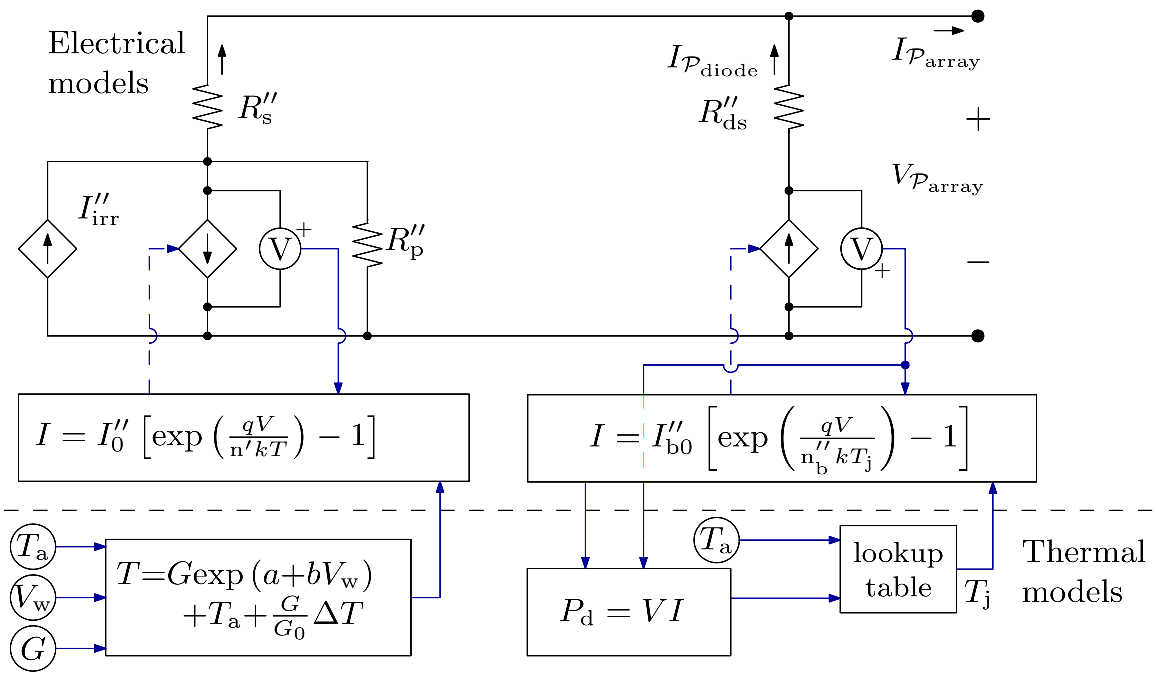

Figure 5.8: Equivalent circuit of $N_\text{ps} \times N_\text{pp}$ array of PV panels, named as $\mathcal{P}_\text{array}$.

This proposed thermoelectric circuital representation, known here as $\mathcal{P}_\text{array}$, is an effective way to simplify the representation of a large PV plant. However, it assumes that all the PV panels feature identical specifications and they are subjected to the same T_a and G [66].

5.3 Detailed validation

In order to validate the proposed model, the schematic of Fig. 5.8 is implemented in Matlab–Simscape. The model's performance is then matchmarked against the Matlab–Simscape's built–in PV panel simulation block, herein known as SPV. The five parameter model is used by SPV to represent any size PV system. For this validation the PV panel Canadian Solar CS6X–325P was used for modeling both $\mathcal{P}_{\text{array}}$ and SPV. The data sheet based representation of this PV panel is displayed in Table 5.2. Then, following the procedure of [57], the five reference parameters listed on Table 5.3 are computed.

Then, the ideality factor, diode series resistance and Schottky barrier height are determined for the BPD LITEON Schottky diode 15SQ045 used in the above mentioned Canadian Solar CS6X–325P. These variables were calculated following the procedure from [60], [59] and [62] using the manufacturer datasheet. BPD reference parameters are listed in Table 5.4.

Finally, four test cases are selected from numerous comparisons between $\mathcal{P}_{\text{array}}$ and SPV panel representations. Those cases are detailed, compared and analyzed in this section. It should be noted that the BPD Matlab–Simscape block requires only two manufacturer datasheet parameters, which are resistance $R_{\text{dio}} = 4.4\ \text{m}\Omega$ and forward voltage $V_{\text{f}} = 0.55$ V. The desktop computer used to run these software simulations has the following specs: Intel core i7–4770 CPU @ 3.40 GHz, 16 GB RAM, Windows 10 Enterprise.

5.3.1 Case study I

For case study I, an SPV panel block is being compared against the proposed representation $\mathcal{P}_{\text{panel}}$ which is based on the proposed model $\mathcal{P}_{\text{block}}$. Here we test the proposed model and the SPV panel block, five separate times, at five different values for G while holding constant the values for T_{a} and V_{w}. [$G_1 = 1000\ \text{W/m}^2$, $G_2 = 800\ \text{W/m}^2$, $G_3 = 600\ \text{W/m}^2$, $G_4 = 400\ \text{W/m}^2$ and $G_5 = 200\ \text{W/m}^2$]. A graphical representation of this case study appears in Fig. 5.9. Since the SPV panel block only provides access to its positive and negative terminals, a string of three series–connected BPDs are connected as illustrated in Fig. 5.9(a). Each BPD represents a real Canadian Solar PV panel partition $\mathcal{P}_{\text{block}}$. Correspondingly, the $\mathcal{P}_{\text{panel}}$

Table 5.2: Electrical and temperature parameters of PV panel Canadian Solar CS6X–325P at STC

Parameter	datasheet value
Nominal maximum power P_{max}	325 W
Open circuit voltage V_{OC}	45.5 V
Voltage at maximum power point V_{MP}	37.0 V
Temperature coefficient of V_{OC}	-0.47 %/°C
Cells per module	72
Short circuit current I_{SC}	9.34 A
Current at maximum power point I_{MP}	8.78 A
Temperature coefficient of I_{SC}	0.053 %/°C

Table 5.3: Reference parameters of PV panel Canadian Solar CS6X–325P at STC

Reference parameter	calculated value
$I_{\text{irr,ref}}$	9.340121238592964 A
$I_{0\text{,ref}}$	$1.0450461712793198 \times 10^{-8}$ A
$R_{\text{s,ref}}$	$3.607947269888581 \times 10^{-3}$ Ω
$R_{\text{p,ref}}$	277.9976323858558 Ω
n_{ref}	1.19337826241932

representation contains one BPD over each of the PV panels $\mathcal{P}_{\text{block}}$ as depicted in Fig. 5.9(b). Simulation results, of this case study, are shown in Fig. 5.10. These traces are a good match and are able to accurately reproduce all five of the I–V curves of the Canadian solar PV panel. To further verify the accuracy of our model, compared to the SPV panel block, we have calculated the RMS error normalized to the mean of the SPV panel block values. The error was obtained using (5.27) and the results are shown in Table 5.5. As can be seen, the errors are all less that 1 %. It is important to note that during case study I, no PS conditions are present.

Table 5.4: Reference parameters of LITEON Schottky barrier diode 15SQ045

Reference parameter	calculated value
n_0	0.76207720
T_0	80.9063881 K
R_{s0}	0.00065000 Ω
E_a	0.04400000 eV
E_0	1.15570000 eV
α	0.00070210 $^{\mathrm{eV}}/_{\mathrm{K}}$
β	1108 K

Additionally, the resultant MPP during $G_1 = 1000\ \mathrm{W/m^2}$, shown in Table 5.6, is nearly identical to the specified $\mathrm{P_{max}}$ of the Canadian Solar CS6X–325P PV panel listed in Table 5.2.

The equation used to obtain the $\mathrm{RMS_{error}}$ is given as:

$$\mathrm{RMS_{error}} = \frac{1}{\widetilde{\theta}}\sqrt{\frac{\sum_{k=1}^{n}(\widehat{\theta}_k - \theta_k)^2}{n}}, \tag{5.27}$$

where $\widetilde{\theta}$ is the mean of the SPV panel block result data set, $\widehat{\theta}_k$ is our proposed model data set and θ_k is the SPV panel block result data set.

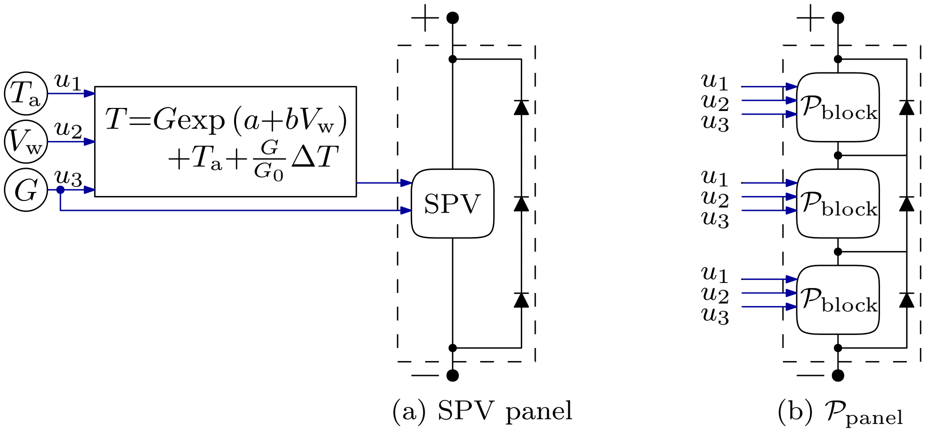

(a) SPV panel (b) $\mathcal{P}_{\mathrm{panel}}$

Figure 5.9: Case study I: (a) SPV panel block, (b) $\mathcal{P}_{\mathrm{panel}}$ based model.

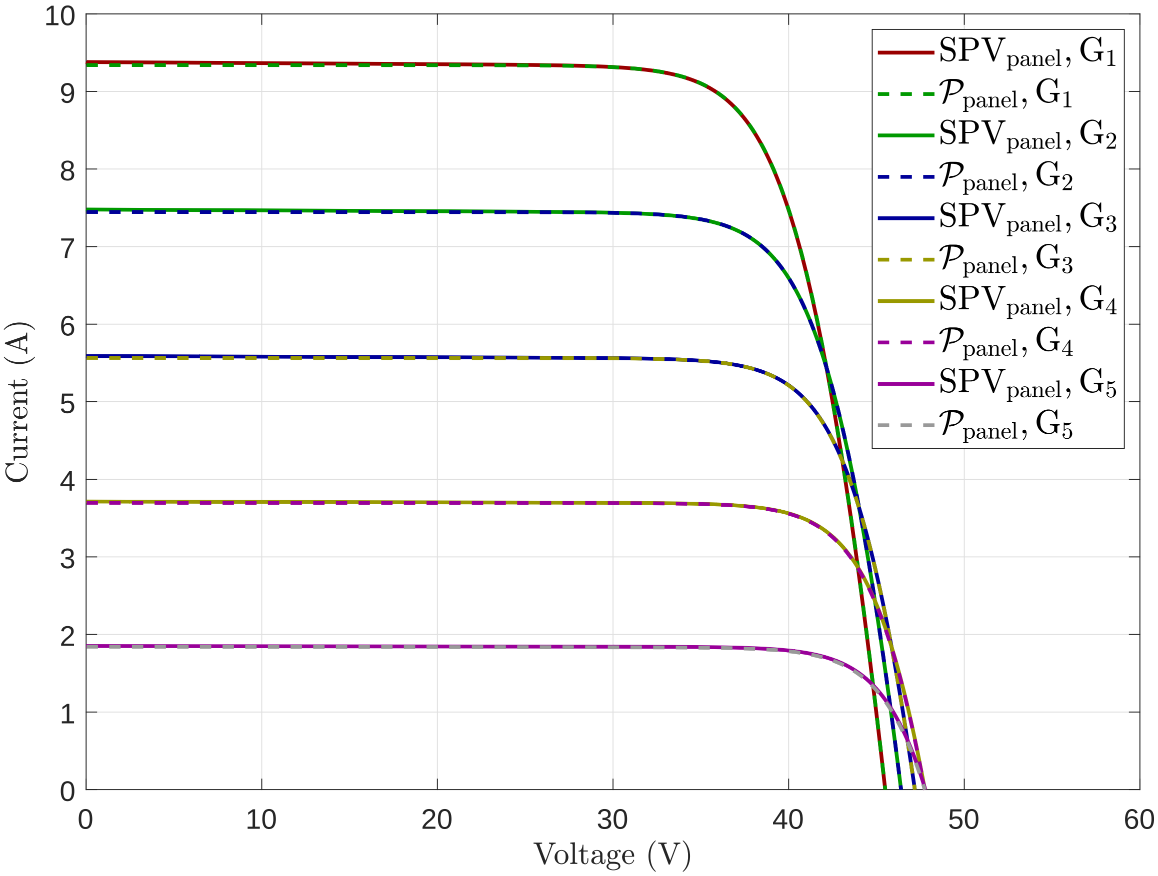

Figure 5.10: Case study I: SPV panel block and $\mathcal{P}_{\mathrm{panel}}$ model I–V curves comparison at different irradiance values.

Table 5.5: $\mathrm{RMS}_{\mathrm{error}}$ in % between SPV panel block and $\mathcal{P}_{\mathrm{panel}}$ model

G (W/m^2)	1000	800	600	400	200
%	0.2352	0.2561	0.2883	0.3428	0.6855

Table 5.6: Case study I: simulation results

Model	Power (W)
$\mathrm{SPV}_{\mathrm{panel,MPP}}$	324.81
$\mathcal{P}_{\mathrm{panel,MPP}}$	324.87

5.3.2 Case study II

Case study II is a comparison of three series–connected SPV panel blocks and three series connected $\mathcal{P}_{\text{panel}}$. Both of these representations include BPDs, following the pattern specified in case study I. Considering PS conditions, each PV panel is subjected to different values of irradiance [$G_1 = 1000$ W/m^2, $G_2 = 700$ W/m^2, $G_3 = 300$ W/m^2], as indicated in Fig. 5.11 and a reduction in the power produced is expected. The ambient temperature is kept equal to $T_{\text{a}} = 287.15$ K and wind speed $V_{\text{w}} = 1$ m/s. It can be seen that there is a mismatch between the traces depicted in Fig. 5.12. Upon further investigation, it seems that the SPV panel block does not include the heat transfer phenomena into the BPD junction box such as dissipated power, radiation, convection and conduction. All of these factors impact the BPD junction temperature when PS conditions are present. The deviations that can be seen in Fig. 5.12 are accounted for by the thermal effects included in the proposed model $\mathcal{P}_{\text{panel}}$. These thermal effects result in a power reduction of approximately 2.22 W, as indicated in Table 5.7.

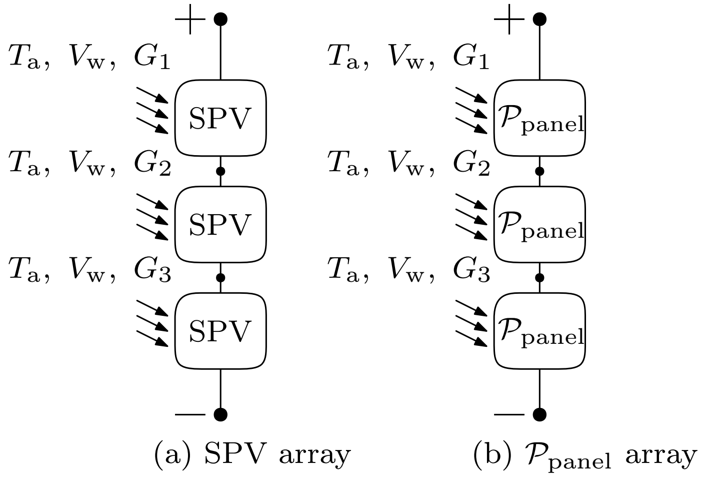

(a) SPV array (b) $\mathcal{P}_{\text{panel}}$ array

Figure 5.11: Case study II: (a) SPV panel based array, (b) $\mathcal{P}_{\text{panel}}$ based array.

5.3.3 Case study III

For this third case study, an SPV array and the proposed representation of a $\mathcal{P}_{\text{array}}$ are compared. Both configurations are comprised of an array of 9×10 PV

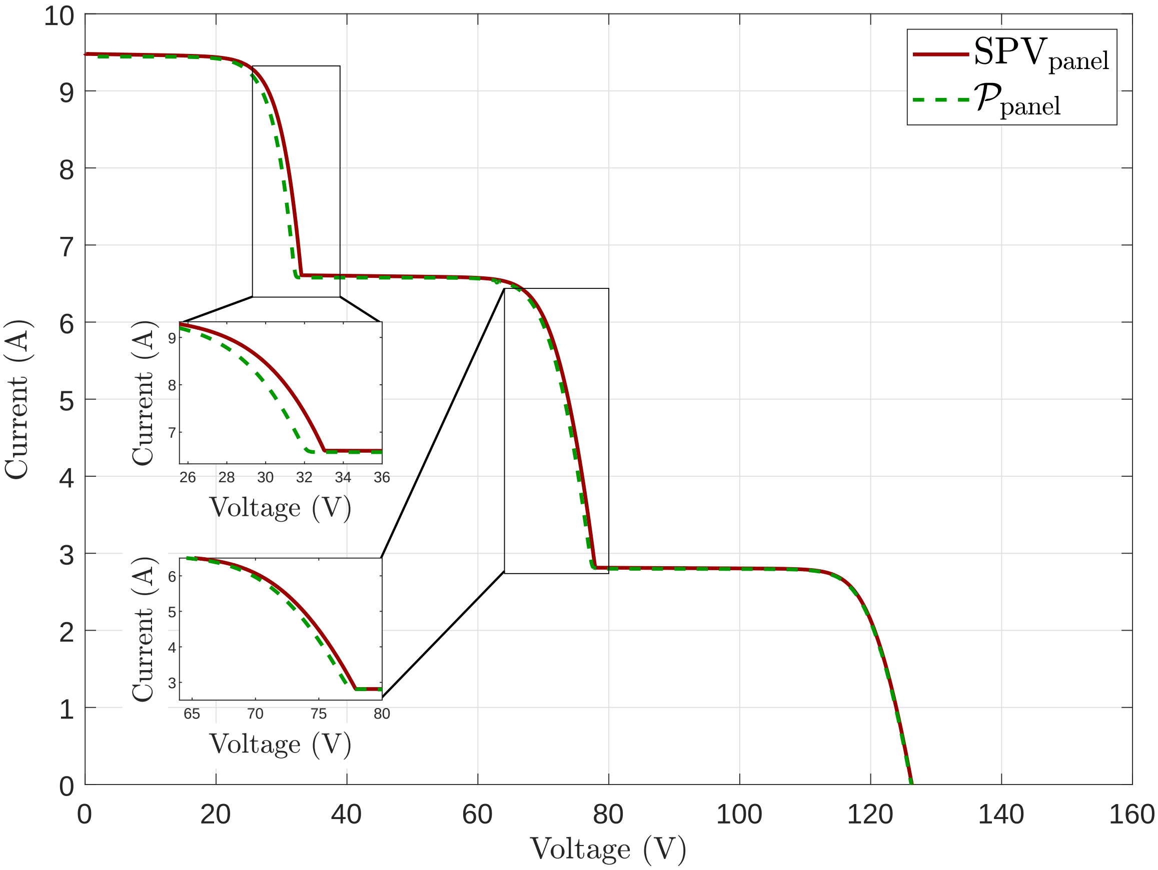

Figure 5.12: Case study II: SPV panel based array and $\mathcal{P}_{\text{panel}}$ based array I–V curves comparison including BPDs and PS.

Table 5.7: Case study II: simulation results

Model	MPP (W)
$\text{SPV}_{\text{panel,MPP}}$	430.6439
$\mathcal{P}_{\text{panel,MPP}}$	428.4288

panels. Three distinct sub–arrays are series–connected and are subjected to different values of irradiance [$G_1 = 1000$ W/m^2, $G_2 = 700$ W/m^2, $G_3 = 300$ W/m^2]. As in the case study I, BPDs are connected to the PV panels. This case study is depicted in Fig. 5.13 and the simulation results are shown in Fig. 5.14. It can be observed that there is a mismatch between these traces. It seems that this mismatch is due to the difference in the way each model accounts for the heat losses of the BPD junction box when PS conditions exist. Furthermore, according to Table 5.8, the proposed $\mathcal{P}_{\text{array}}$ representation outperforms the SPV array when simulation times are compared. The large savings in simulation time, meaning the $\mathcal{P}_{\text{array}}$ requires only 1.3 % of the time in comparison to the SPV array, is a result of no aggregation being performed of the BPD for the SPV array model. Lastly, consistent with case study II, an approximately 110 W reduction of power produced is shown. It seems the proposed model $\mathcal{P}_{\text{array}}$ more accurately takes into account this power reduction for a $\mathcal{P}_{\text{array}}$ experiencing the effect of PS.

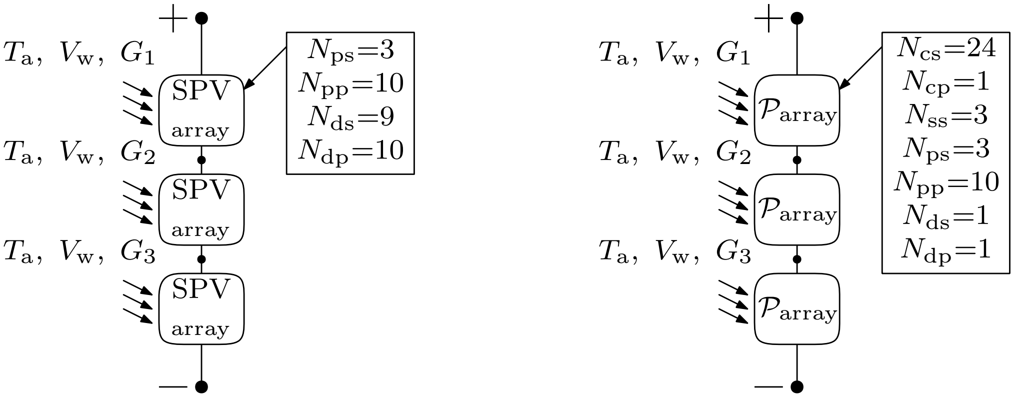

(a) string of three SPV array (b) string of three $\mathcal{P}_{\text{array}}$ blocks

Figure 5.13: Case study III: (a) SPV array, (b) $\mathcal{P}_{\text{array}}$ model based.

Table 5.8: Case study III: simulation results

Model	MPP (kW)	Time (s)
$\text{SPV}_{\text{array,MPP}}$	12.919	3861
$\mathcal{P}_{\text{array,MPP}}$	12.809	53

5.3.4 Case study IV

Case study IV is a variation of case study III. The difference here is that the array of BPDs ($N_{\text{ds}} = 9 \times N_{\text{dp}} = 10$) are linked over each series–connected SPV array and are being aggregated into a single equivalent Matlab–Simscape BPD block. Also, two modified parameters $V_{\text{f,eq}}$ and $R_{\text{dio,eq}}$ are calculated according to (5.28) and are

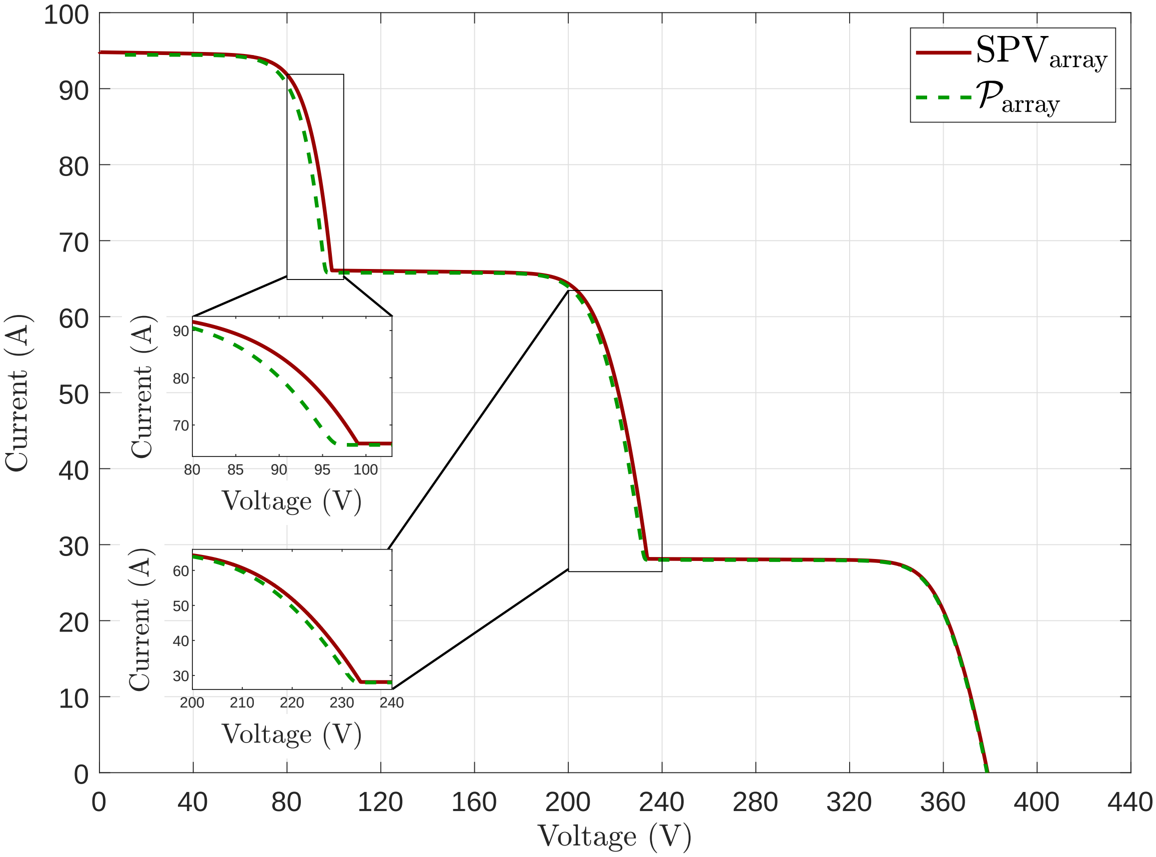

Figure 5.14: Case study III: SPV array and $\mathcal{P}_{\text{array}}$ model based I–V curves comparison including BPDs and PS.

entered into the single equivalent Matlab–Simscape BPD block. This case study IV is depicted in Fig. 5.15. To verify the accuracy of the BPD aggregation and to be consistent with case study III, Figures 5.14 and 5.16 are compared. It can be seen that there is nearly a perfect match between the traces in these figures. Furthermore, according to Tables 5.8 and 5.9, the MPP values calculated from their I–V curves are nearly the same. These results are then verified by comparing simulation run times, indicated in Tables 5.8 and 5.9. Due to equation (5.28) allowing the aggregation of any number of series and parallel connected BPDs into a single equation, a simulation time savings of over 99 % is obtained.

$$V_{\mathrm{f,eq}} = V_{\mathrm{f}} N_{\mathrm{ps}} N_{\mathrm{ss}} N_{\mathrm{ds}}, \quad R_{\mathrm{dio,eq}} = \frac{R_{\mathrm{dio}} N_{\mathrm{ps}} N_{\mathrm{ss}} N_{\mathrm{ds}}}{N_{\mathrm{pp}} N_{\mathrm{dp}}}. \tag{5.28}$$

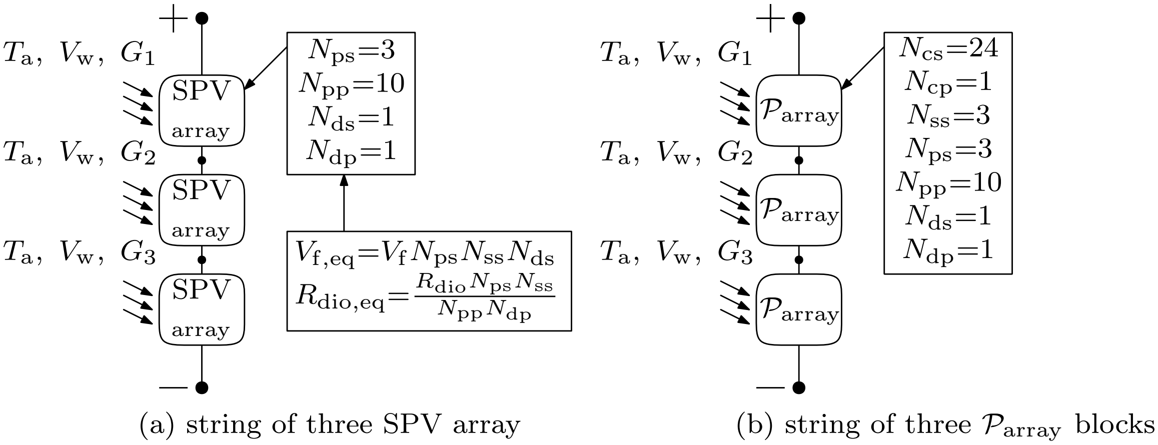

(a) string of three SPV array (b) string of three $\mathcal{P}_{\mathrm{array}}$ blocks

Figure 5.15: Case study IV: (a) SPV array, (b) $\mathcal{P}_{\mathrm{array}}$ model based.

Table 5.9: Case study IV: results

Model	MPP (kW)	Time (s)
$\mathrm{SPV}_{\mathrm{array,MPP}}$	12.919	20
$\mathcal{P}_{\mathrm{array,MPP}}$	12.852	52

5.4 Application example

In this section, an application example is detailed and implemented in PSCAD/EMTDC. This includes the proposed thermoelectric modular model, partial shading modeling, real data measurements of ambient temperature, cell temperature, and wind speed and also a performance analysis of several MPPT algorithms proposed in [55].

5.4.1 Partial shading due to a cloud movement

A major challenge of PS is that while moving across a PV plant, clouds can evolve, change shape and change direction. These constantly changing variables require a complex model with no simple solution. Therefore, this investigation makes the following set of assumptions. First, the clouds move at a constant speed, V_{cloud},

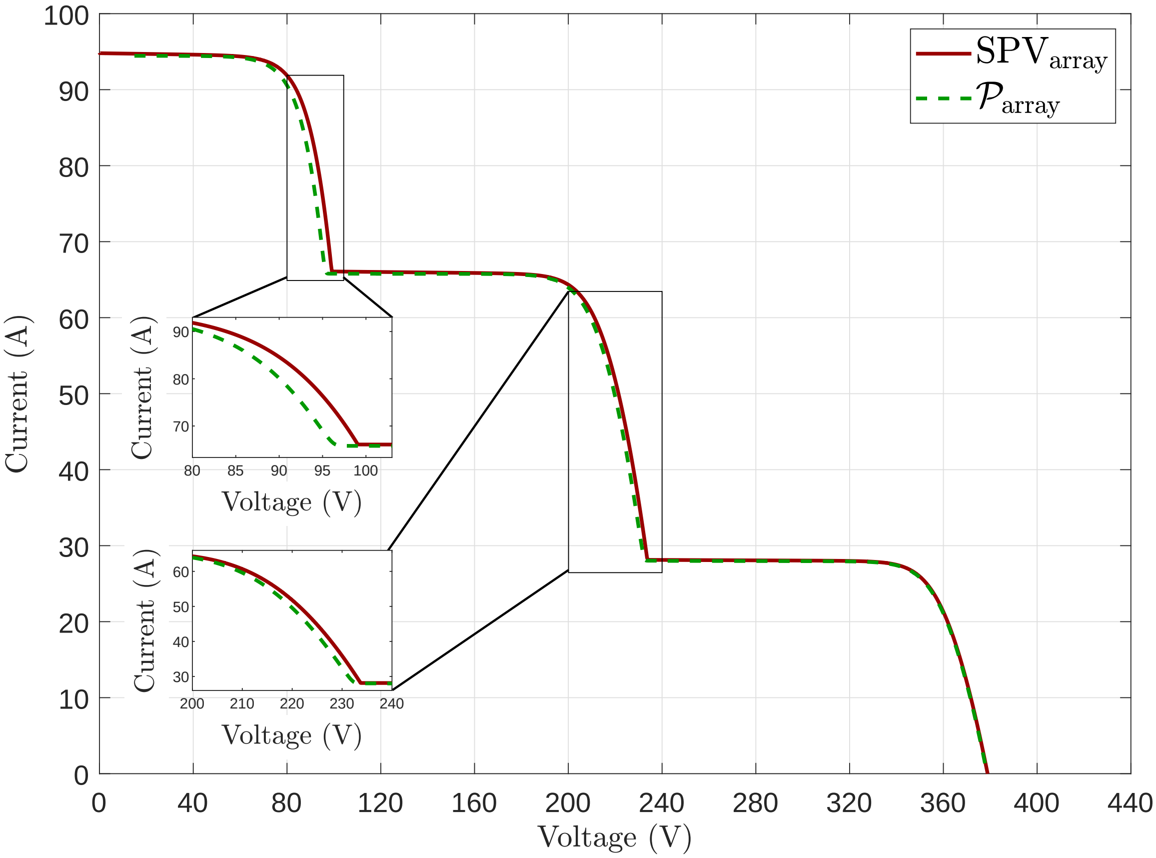

Figure 5.16: Case study IV: SPV array and $\mathcal{P}_{\text{array}}$ model based I–V curves comparison including BPDs and PS.

and in a direction that is in parallel with the PV plant. Second, the clouds will neither change shape nor evolve. Finally, the clouds will be in the middle cloud level, which is characterized by white or greyish large clouds that are able to blot out the sun. Let G_1, G_2, G_3 be defined by the solar irradiance at the points shown in Fig. 5.17. Since the cloud moves at a constant speed and moves over the distance between solar collectors d in time d/V_{cloud}, the following would hold for the irradiance at these points [67]:

$$G_3(t + \Delta T_{\text{cloud}}) = G_1(t), \tag{5.29}$$

$$G_1(t) = G_2(t), \tag{5.30}$$

$$\Delta T_{\text{cloud}} = \frac{d}{V_{\text{cloud}}}. \tag{5.31}$$

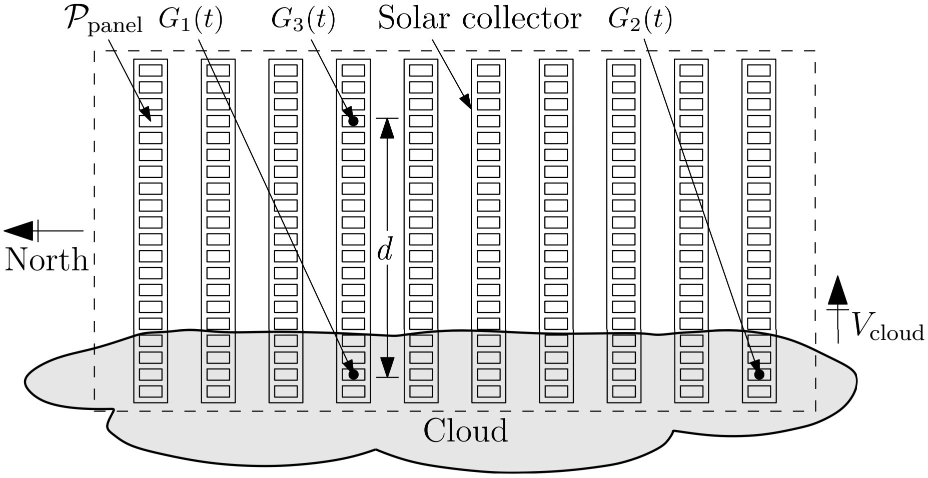

Figure 5.17: Cloud moving across a PV plant.

In [68], this approach was utilized, moreover three sensors were located in different positions to captured this effect, see [69] and references within. Notice, ΔT_{cloud} can be rewritten as a function of the distance d, the cloud height (h) and cloud's speed V_{cloud} as follows:

$$\Delta T_{\text{cloud}} = \left(\frac{d + 0.009h}{V_{\text{cloud}}} \right), \tag{5.32}$$

where $0.009h$ is the effective width of the sun at the cloud height [70]. This means that the irradiance at any point within the area can be approximated by a time–shifted irradiance data for one point location [67]. Even though the shaded section temperature will be lower than the unshaded section, research has shown that such a difference can be neglected [69].

5.4.2 Single–stage PV system

This section details a PSCAD/EMTDC simulation of a 455 kW grid–connected single–stage PV power plant. As illustrated in Fig. 5.19, the realization includes the proposed model, a VSI, a step up transformer and a Thévenin equivalent of the power grid. The design of the various components is performed according to a typical "1000 V DC" architecture.

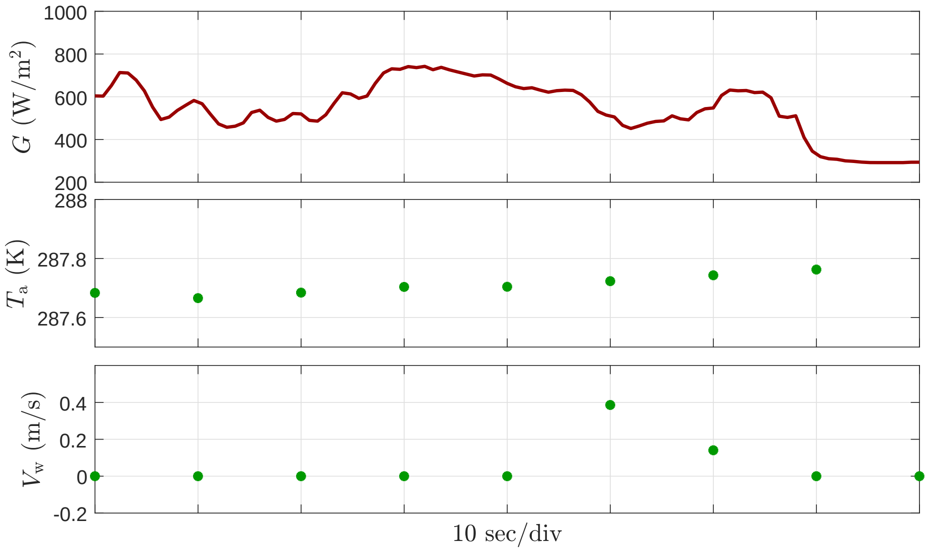

Figure 5.18: Actual G, T_{a} and V_{w} profiles that were used during the simulation.

The PV array is constructed using 70 parallel–connected strings of 20 series–connected Canadian Solar CS6X–325P PV modules. This PV array is implemented based on the proposed $\mathcal{P}_{\text{array}}$ representation. A total of 10 parallel–connected south–facing solar collectors are used. The optimal physical operating conditions for winter season performance were then calculated according to [71]. This included optimizing the distance between the solar collectors (16.3 m), the tilt angle (63.18°) and the shading angle (25.42°).

The VSI switching frequency is chosen to be equal to $F_{\text{s}} = 6$ kHz, and the DC–link capacitor is equal to 5000 μF. The filter inductor, capacitor and damping resistance were selected to be $L = 38.675$ μH, $C_{\text{f}} = 363.87$ μF and $R_{\text{f}} = 64.2$ mΩ respectively. The VSI control was computed following the guidelines in [55].

A step up transformer, rated at 600 kVA, with a transformation ratio of 270 V/12.47 kV and an impedance of 6 % is utilized. In addition, the Thévenin equivalent of the power grid, rated at 100 MVA, featuring 12.47 kV/60 Hz and a unity X/R ratio is included.

To give this simulation further validity, real data of PV operating conditions were also used. Over a period of 80 s, as shown in Fig. 5.18, G was sampled every 800

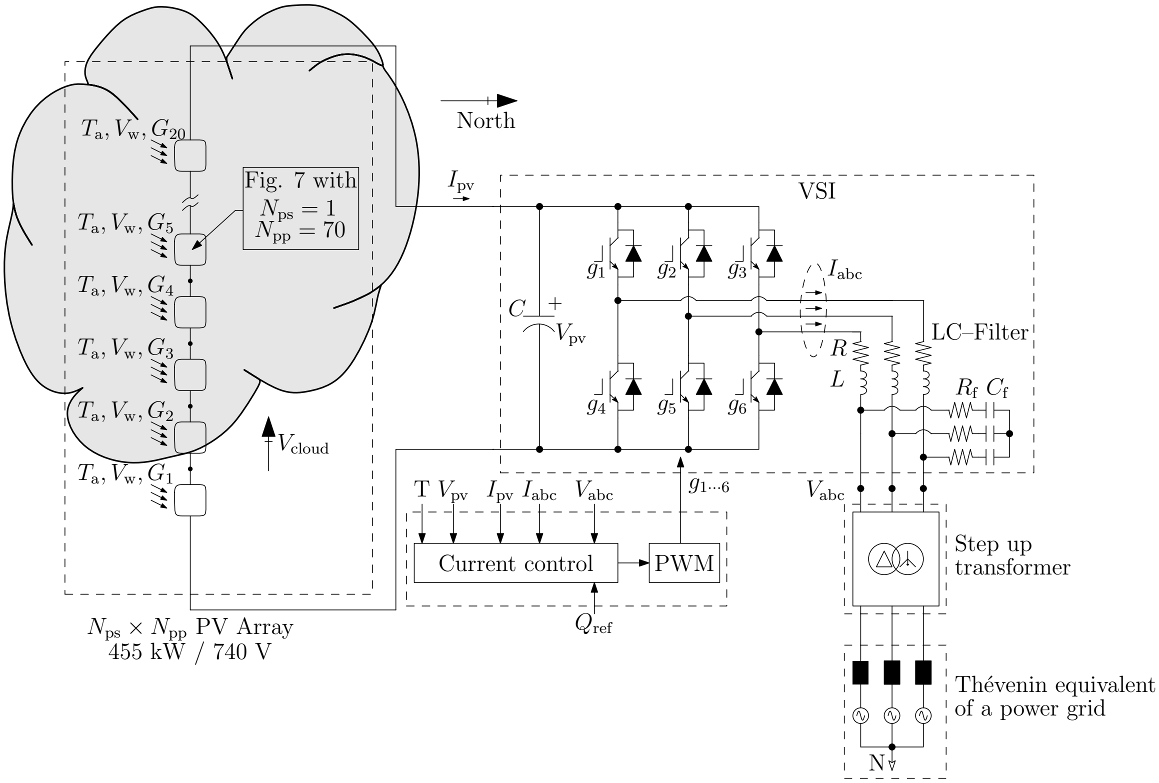

Figure 5.19: Circuit schematic of the grid–connected single–stage PV plant.

ms while T_a and V_w were recorded every 10 s. This PV operating condition data was measured in Denver, Colorado, USA, on a partially cloudy day. Finally, the fixed sampling period, for the iterative MPPT algorithms, was set to 0.2 s. Studies were then performed on the MPPT algorithms reacting to constant V_{cloud} moving from East to West. It is assumed that the cloud will fully cover 70 parallel–connected strings of one series–connected PV module at a time. ΔT_{cloud} was found to be equal to 1.6 s at $V_{cloud} = 18$ m/s and $h = 3$ km [72]. A solar irradiance of 762.731 W/m^2, wind speed of 3.082 m/s and the ambient temperature of 291.358 K was used to represent a clear sky setting. These data measurements were collected by NREL, [73], in the city of Denver on May 4, 2018, at 9:00 am. The simulation was run for 12 s under clear sky conditions, to ensure each MPPT was able to reach its MPP.

The MPPT algorithms, used in this comparison study, are of the conventional type and were chosen based on the paper published by [74]. That paper showed that large scale PV systems most commonly use the conventional perturb and observe or incremental conductance MPPT techniques. The benefits of conventional MPPT algorithms include their simplicity, required measurements, convergence speed, effectiveness, cost, and comparatively low number of input parameters.

The main purpose of this simulation was to measure the actual extracted power. Then a comparison was done on how far each MPPT algorithm was from the PV panel's optimal MPP. The comparison was made for not only power but also on voltage measurements.

5.4.3 Simulation results

The overall performance of the MPPT algorithms is shown in Fig. 5.20. The data demonstrates that the MPPT algorithms behaved poorly under PS conditions. The normalized difference between the theoretical power at the MPP and the actual extracted power (Diff) shows that none of the algorithms are able to perfectly track the MPP during the whole simulation. This is reflected in the corresponding tracking factors (TF), defined as the ratio between the actual amount of energy extracted from the PV panel and the theoretically available power. All the algorithms have to overcome several local maximum, in order to find the global maximum. The discrete P–V curve shown in Fig. 5.21, exhibit multiple extrema behavior. As a result, the actual extracted power might not be the optimal one. The results presented in Fig. 5.20, show that the algorithms are able to track the MPP in the 400 V to 500 V range because the global maximum remains relatively constant as can be seen in Fig. 5.21. However, the algorithms are trapped by a local maximum when the global maximum starts to fluctuate moving from right to left. For this reason, Fig. 5.20 shows a gap in the beginning and at the end of the simulation. It can also be seen that the TF of NN based algorithm achieved the poorest performance, with a value of 95.43 %. This is due to the fact that the NN based algorithm is not based on the proposed $\mathcal{P}_{\text{array}}$ model.

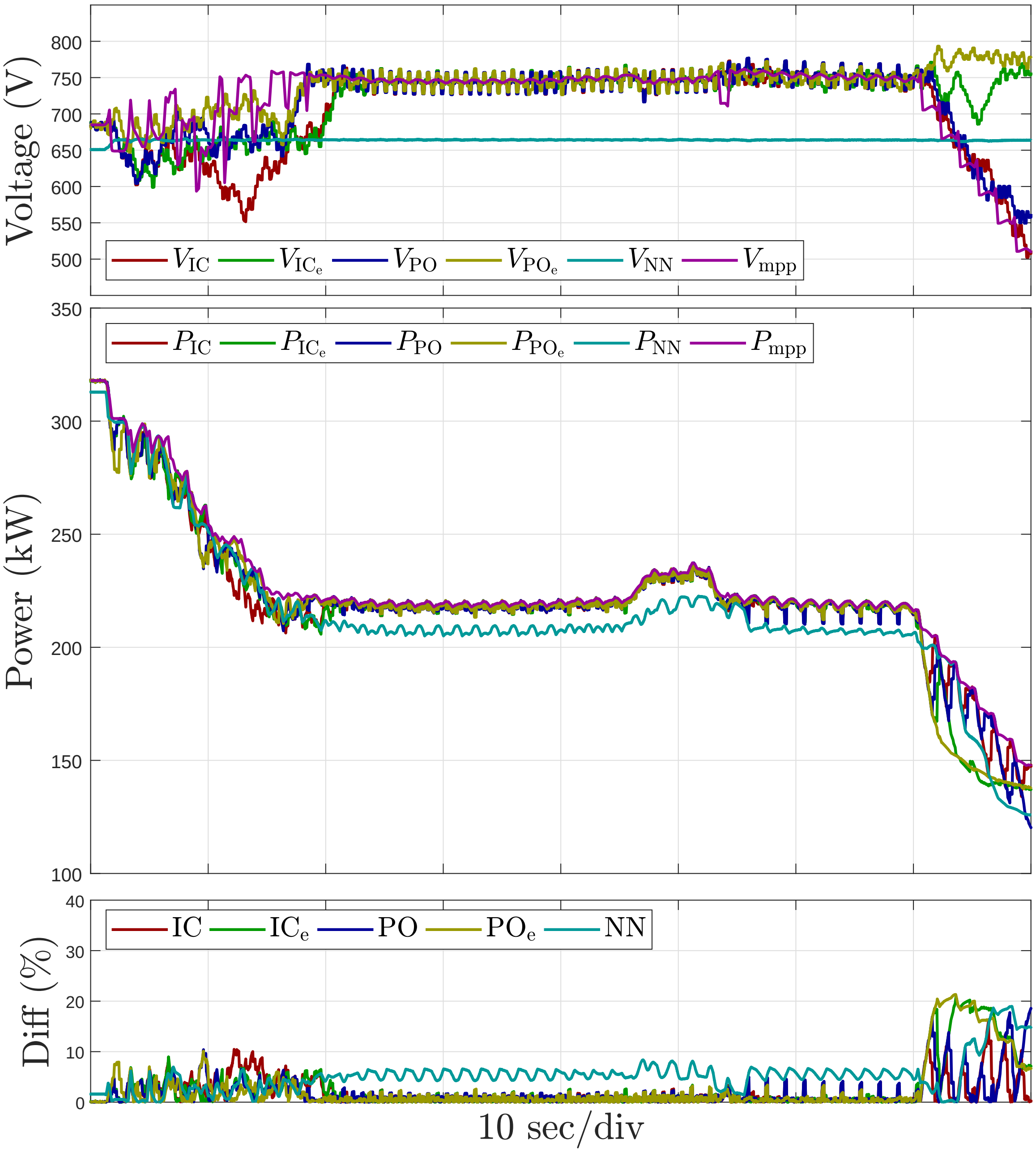

Figure 5.20: Performance of the IC, P&O, enhanced IC, P&O and, the NN algorithms.

5.5 Conclusions

This work proposed a thermoelectric modular model, that represents in detail PV cells parallel–connected to BPDs. This model is comprised of two models, one is of an equivalent array of PV cells $N_{\mathrm{cs}} \times N_{\mathrm{cp}}$ identified as $\mathcal{P}_{\mathrm{cell}}$ and the other is of an equivalent array of BPDs $N_{\mathrm{ds}} \times N_{\mathrm{dp}}$ termed as $\mathcal{P}_{\mathrm{diode}}$. When these building blocks are then parallel–connected, an equivalent model for an array of PV cells and

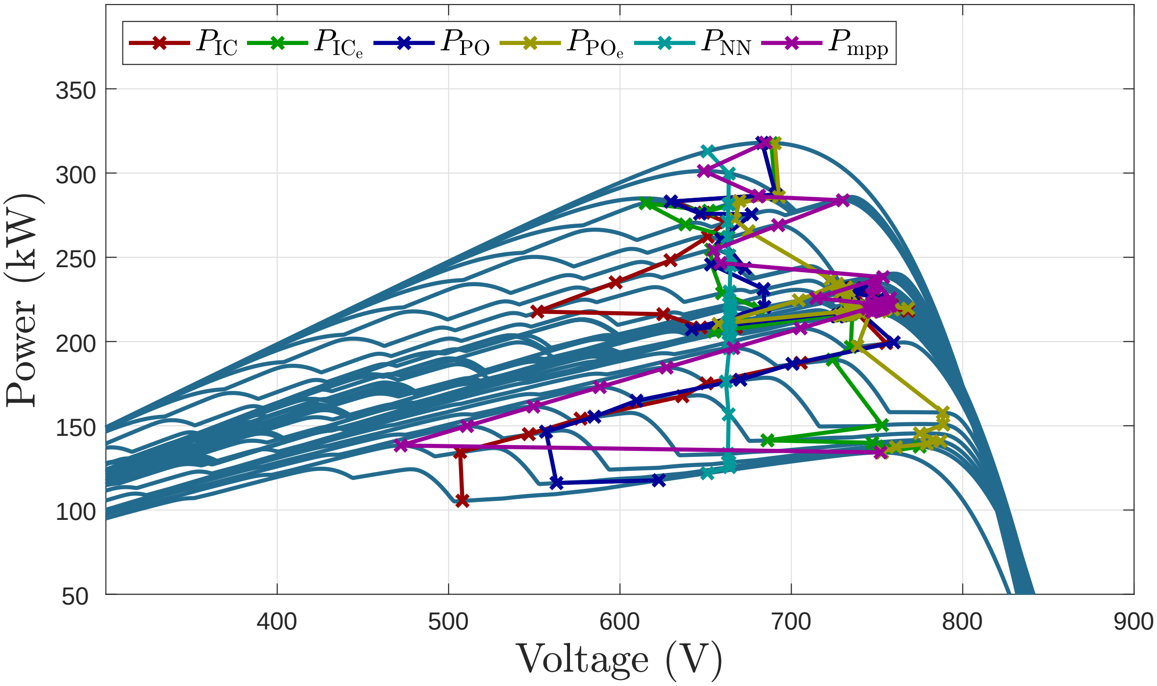

Figure 5.21: Performance of the MPPT algorithms at specific periods of time.

Table 5.10: Performance of conventional and enhanced MPPT algorithms

Algorithm	TF (%)
$\mathrm{IC_e}$	97.82
IC	98.23
$\mathrm{P\&O_e}$	97.89
P&O	98.24
NN	95.43

an array of BPDs, $\mathcal{P}_{\text{block}}$, is obtained. Thus, a $\mathcal{P}_{\text{panel}}$ can be modeled by connecting in series N_{ss} number of $\mathcal{P}_{\text{blocks}}$. Also, an aggregation in series and in parallel of any number of $\mathcal{P}_{\text{panel}}$, yields a PV array representation termed $\mathcal{P}_{\text{array}}$. This proposed model features modularity, simplicity, and ease of use on a unified framework. This modified PV panel circuit can be easily implemented in simulation programs such as PSCAD/EMTDC and Matlab–Simscape.

Validations of the proposed model $\mathcal{P}_{\text{array}}$ were detailed and analyzed in depth.

Reference parameters for both the Canadian Solar CS6X–325P PV model and the LITEON Schottky 15SQ045 were determined, following the methodologies highlighted in recently published literature. From the validation results, the proposed $\mathcal{P}_{\text{array}}$ seems to be accurate in determining the power produced by a PV system, all while accounting for fluctuations in ambient temperature, junction temperature and wind speed over the PV cells and BPDs. Moreover, it takes into account the thermal effects of the BPD junction temperature, due to the heat transfer phenomena, such as dissipated power, radiation, convection and conduction. These thermal effects reduce the output power of a real–world PV system and the proposed model accurately emulates this reduction. This proposed model was then carefully validated through detailed Matlab–Simscape and PSCAD/EMTDC simulations. The close match of the I–V and P–V curves, during different test cases, demonstrated the reliability and accuracy of the proposed model.

Lastly, a comparison study was implemented in PSCAD/EMTDC and then analyzed in depth. Several MPPT algorithms were compared, with respect to both power and voltage measurements, as they performed in a 455 kW grid–connected single–stage PV system. This PSCAD/EMTDC simulation included both the proposed model $\mathcal{P}_{\text{array}}$ of the PV system and the effects of realistic PS cloud cover.

An area of further research is highlighted by the fact that none of the compared MPPT algorithms were able to perfectly track the MPP under realistic PS conditions. Due to the multiple extrema behavior of P–V curves; MPPT algorithms were frequently trapped by local maximum, rather than finding the global maximum.

Acknowledgment

The work of A. Angulo was supported by Fondecyt Chile under Grant 11170229, by the Basal Project FB0008 “Advanced Center for Electrical and Electronic Engineering”.

CHAPTER 6

CONCLUDING REMARKS

In this chapter a list of contributions, research products, as well as conclusions and future work are presented.

6.1 Contributions

- Modeling and control approach in a unified two–frequency *dq* reference frame for a Hexverter–based system

- Proposal and assessment of a "virtual V_C^2 controller" that dynamically accounts for Hexverter's active power losses, allowing to achieve active power balance on the fly

- Detailed assessment and validation of modulation strategies through total harmonic distortion of synthesized voltages and currents out of computer simulations developed in PSCAD/EMTDC software platform

- Modeling of a thermoelectric modular model that is able to represent a PV power plant of an arbitrary size capturing the details of all constituent PV cells and bypass diodes through a single equivalent circuital representation

- A novel thermal equation that yields bypass diodes' junction temperature, including the heat transfer phenomena into the junction box, due to dissipated power, radiation, convection, and conduction

- An application example of the proposed model comprising a comparative evaluation of several maximum power point tracking algorithms, while operating on a large grid–connected photovoltaic power plant, subjected to realistic partial shading conditions

6.2 Research products

- **H. R. Robles–Campos**, and F. Mancilla–David, “Selective Harmonic Elimination for the Modular Multilevel Converter,” *2016 North American Power Symposium (NAPS), Denver, Colorado, USA*, Sep. 2016, pp. 1–6.

- **H. R. Robles–Campos**, and F. Mancilla–David, “A comparative evaluation of modulation strategies for Hexverter–based Modular Multilevel Converters,”, *International Conference on Industrial Technology (ICIT) 2019, Melbourne, Australia*, Feb. 2019, pp. 1–6. **This research product obtained the IEEE Industrial Electronic Society “Student best paper award” in Aug, 2020.**

- **H. R. Robles–Campos**, and F. Mancilla–David, “A control scheme in the dq reference frame for Hexverter–based systems,” *2019 North American Power Symposium (NAPS), Wichita, Kansas, USA*, Oct. 2019, pp. 1–6.

- **H. R. Robles–Campos**, B. J. Azuaje–Berbecí, C. J. Scheller, A. Angulo, and F. Mancilla–David, “Detailed modeling of large scale photovoltaic power plants under partial shading conditions,”, *Solar Energy*, Volume 194, Pages 485–498, Dec., 2019.

- **H. R. Robles–Campos**, and F. Mancilla–David, “Detailed Assessment of Modulation Strategies for Hexverter–Based Modular Multilevel Converters,”, *Energies*, Volume 15, Mar., 2022.

6.3 Conclusions

In this dissertation, the operational principle of the direct AC–AC multilevel power converter “Hexverter” was presented. The subsystems *(i)* branch current controlled performing in a unified two–frequency dq framework, and *(ii)* a proposed "virtual V_{C}^2 controller" were integrated to a multilevel power converter setup composed of: *(a)* modulator, *(b)* voltage balancing algorithm and *(c)* a Hexverter system. The results obtained suggest the proposed control scheme is able to regulate the Hexverter–based system under NLC and PD–SPWM modulation strategies. Moreover, an assessment of total harmonic distortion of AC three–phase voltages and currents was thoroughly developed. It seems, NLC modulation strategy outperforms PD–SPWM modulation technique. Be aware, all the THD values obtained out of PSCAD/EMTDC simulations are compliant with international standards IEEE 519 [2] and IEC61000–3–2 [3]. Validations of proposed "virtual V_{C}^2 control" were presented. According to the results obtained, "virtual V_{C}^2 controller" was able to accurately determine the active power loss of the Hexverter–based system. Furthermore, by assessing ΔP values of both modulation techniques and under the scenarios of Test Case I and II, nearest level control technique yielded superior efficiency. Experimental validation of the analysis presented herein is currently under investigation.

Furthermore, since one of the goals of the presented dissertation is to help advance the integration of photovoltaic systems into the distribution grids by tackling technical challenges this technology is facing. Some technical solutions were developed to help support the high penetration of photovoltaic systems, while improving efficiency, reliability and power quality of distribution grids. This dissertation proposed the modeling of a thermoelectric modular model that is able to represent a PV power plant of an arbitrary size capturing the details of all constituent PV cells and bypass diodes through a single equivalent circuital representation. In addition, a novel thermal equation that yields bypass diodes' junction temperature, including the heat transfer phenomena into the junction box, due to dissipated power, radiation, convection, and conduction was presented. In the end, an application example of the proposed model comprising a comparative evaluation of several maximum power point tracking algorithms, while operating on a large grid–connected photovoltaic power plant, subjected to realistic partial shading conditions was implemented. The simulation was implemented in PSCAD/EMTDC, and includes the proposed model, a VSI, a step up transformer and a Thévenin equivalent of a power grid, along with real values of solar irradiance, ambient temperature, and wind speed measurements.

6.4 Future work

The presented dissertation opens up possibilities for future work. For instance, experimental validation of the proposed control scheme and the assessment of some other modulation techniques, such as, selective harmonic elimination and space vector modulation, when applied to the Hexverter–based system, offer the possibility to develop an important study. In addition, an area of further research is the comparison of the proposed control approach against others control techniques designed for multilevel power topologies and readily available in recent literature. The application of a grid connected Hexverter–based system to drive a wind energy conversion system is an interesting study to be developed. Moreover, there is a lack of a systematic approach to design each of the Hexverter elements and subsystems in terms of efficiency, costs, communication protocols between subsystems and its operational range. Furthermore, the study of how the proposed control scheme performs under unbalanced operational conditions, along with the proposed solutions to support its correct functioning, is another important study to be developed. Regarding PV systems and highlighted by the fact that none of the compared MPPT algorithms were able to perfectly track the MPP under realistic PS conditions. There is a significant opportunity for the development of an MPPT algorithm able to find the global MPP even if the PV system is under PS conditions. Furthermore, the study of integration of smart PV inverters with battery energy storage systems is nowadays a trending research topic.

REFERENCES

[1] A. Mertens and L. Baruschka. Transformatorloser direktumrichter, Apr. 2010.

[2] IEEE Standards Association. IEEE Std 519–2014 Recomended Practice and Requirements for Harmonic Control in Electric Power Systems, Jan. 2014.

[3] International Electrotechnical Commission. IEC Standard 61000-3-2:2018 Electromagnetic Compatibility (EMC), Jan. 2018.

[4] P. Blaszczyk, K. Kóska, and P. Klimczak. Energy balancing in modular multilevel converter systems. *Bulletin of The Polish Academy of Sciences–Technical Sciences*, 65:685–694, 2017.

[5] A. Lesnicar and R. Marquardt. A new modular voltage source inverter topology. In *Proccedings of 10th European Conference on Power Electronics and Applications*, Jan. 2003.

[6] S. Angkititrakul and R. W. Erickson. Control and implementation of a new modular matrix converter. In *Nineteenth Annual IEEE Applied Power Electronics Conference and Exposition, 2004. APEC '04.*, volume 2, pages 813–819, 2004.

[7] H. Akagi. Classification, Terminology, and Application of the Modular Multilevel Cascade Converter (MMCC). *IEEE Transactions on Power Electronics*, 26(11):3119–3130, Nov. 2011.

[8] L. Baruschka and A. Mertens. A new 3–phase AC/AC modular multilevel converter with six branches in hexagonal configuration. In *2011 IEEE Energy Conversion Congress and Exposition*, pages 4005–4012, Sep. 2011.

[9] L. Baruschka and A. Mertens. A New Three–Phase AC/AC Modular Multilevel Converter With Six Branches in Hexagonal Configuration. *IEEE Transactions on Industry Applications*, 49(3):1400–1410, May. 2013.

[10] D. Karwatzki, L. Baruschka, M. von Hofen, and A. Mertens. Optimised Operation Mode for the Hexverter Topology Based on Adjacent Compensating Power. In *2014 IEEE Energy Conversion Congress and Exposition (ECCE)*, pages 5399–5406, Sep. 2014.

[11] D. Karwatzki, L. Baruschka, M. von Hofen, and A. Mertens. Branch Energy Control for the Modular Multilevel Direct Converter Hexverter. In *2014 IEEE Energy Conversion Congress and Exposition (ECCE)*, pages 1613–1622, Sep. 2014.

[12] D. Karwatzki, L. Baruschka, and A. Mertens. Survey on the Hexverter Topology– A Modular Multilevel AC/AC Converter. In *2015 9th International Conference on Power Electronics and ECCE Asia (ICPE-ECCE Asia)*, pages 1075–1082, Jun. 2015.

[13] D. Karwatzki and A. Mertens. Generalized Control Approach for a Class of Modular Multilevel Converter Topologies. *IEEE Transactions on Power Electronics*, PP(99):1–1, 2017.

[14] Y. Wan, S. Liu, and J. Jiang. Multivariable Optimal Control of a Direct AC/AC Converter under Rotating *dq* Frames. In *2013 Journal of Power Electronics)*, pages 419–428, May. 2013.

[15] Yongqing Meng, Bo Liu, Huiyong Luo, Shuonan Shang, Haitao Zhang, and Xifan Wang. Control scheme of hexagonal modular multilevel direct converter for offshore wind power integration via fractional frequency transmission system. *Journal of Modern Power Systems and Clean Energy*, 6, Jul. 2017.

[16] A. Yazdani and R. Iravani. *Voltage–Sourced Converters in Power Systems: Modeling, Control, and Applications.* IEEE, 2010.

[17] H. R. Robles–Campos and F. Mancilla–David. A comparative evaluation of modulation strategies for Hexverter–based Modular Multilevel Converters. In *2019 IEEE International Conference on Industrial Technology (ICIT)*, pages 1465–1470, 2019.

[18] L. Baruschka and A. Mertens. A New 3–Phase Direct Modular Multilevel Converter. In *Proceedings of the 2011 14th European Conference on Power Electronics and Applications*, Aug. 2011.

[19] D. Karwatzki, L. Baruschka, J. Kucka, M. von Hofen, and A. Mertens. Improved Hexverter Topology with Magnetically Coupled Branch Inductors. In *2014 16th European Conference on Power Electronics and Applications*, pages 1–10, Aug. 2014.

[20] L. Baruschka, D. Karwatzki, M. von Hofen, and A. Mertens. Low–Speed Drive Operation of the Modular Multilevel Converter Hexverter Down to Zero Frequency. In *2014 IEEE Energy Conversion Congress and Exposition (ECCE)*, pages 5407–5414, Sep. 2014.

[21] S. I. Hamasaki, K. Okamura, T. Tsubakidani, and M. Tsuji. Control of Hexagonal Modular Multilevel Converter for 3–phase BTB System. In *2014 International Power Electronics Conference (IPEC–Hiroshima 2014–ECCE ASIA)*, pages 3674–3679, May. 2014.

[22] R. Tsuruta, T. Hosaka, and H. Fujita. A New Power Flow Controller Using Six Multilevel Cascaded Converters for Distribution Systems. In *2014 International Power Electronics Conference (IPEC–Hiroshima 2014–ECCE ASIA)*, pages 1350–1356, May. 2014.

[23] D. Karwatzki, M. von Hofen, L. Baruschka, and A. Mertens. Operation of Modular Multilevel Matrix Converters with Failed Branches. In *IECON 2014–40th Annual Conference of the IEEE Industrial Electronics Society*, pages 1650–1656, Oct. 2014.

[24] H. R. Robles–Campos and F. Mancilla–David. A control scheme in the dq reference frame for hexverter–based systems. In *2019 North American Power Symposium (NAPS)*, pages 1–6, 2019.

[25] J. Qin and M. Saeedifard. Reduced Switching–Frequency Voltage–Balancing Strategies for Modular Multilevel HVDC Converters. *IEEE Transactions on Power Delivery*, 28(4):2403–2410, Oct. 2013.

[26] G. Konstantinou, J. Pou, S. Ceballos, R. Darus, and V. G. Agelidis. Switching Frequency Analysis of Staircase–Modulated Modular Multilevel Converters and Equivalent PWM Techniques. *IEEE Transactions on Power Delivery*, 31(1):28–36, Feb. 2016.

[27] P. Hu and D. Jiang. A Level–Increased Nearest Level Modulation Method for Modular Multilevel Converters. *IEEE Transactions on Power Electronics*, 30(4):1836–1842, Apr. 2015.

[28] D. Knuth. *The Art of Computer Programming*, pages 158–168. Addison–Wesley, 1998.

[29] PSCAD/EMTDC. *version 4.6.3*. Manitoba HVDC Research Centre, 2018.

[30] H. Tian, F. Mancilla–David, K. Ellis, E. Muljadi, and P. Jenkins. Determination of the optimal configuration for a photovoltaic array depending on the shading condition. *Solar Energy*, 95:1–12, Jun. 2013.

[31] R. Ramaprabha and B. L. Mathur. A Comprehensive Review and Analysis of Solar Photovoltaic Array Configurations under Partial Shaded Conditions. *International Journal of Photoenergy*, 2012:1–16, Nov. 2012.

[32] E. Kandemir, N.S. Cetin, and S. Borekci. A comprehensive overview of maximum power extraction methods for PV systems. *Renewable and Sustainable Energy Reviews*, 78(Supplement C):93–112, Oct. 2017.

[33] Y. Chaibi, M. Malvoni, A. Chouder, M. Boussetta, and M. Salhi. Simple and efficient approach to detect and diagnose electrical faults and partial shading in photovoltaic systems. *Energy Conversion and Management*, 196:330–343, Sep. 2019.

[34] S. Silvestre, S. Kichou, A. Chouder, G. Nofuentes, and E. Karatepe. Analysis of current and voltage indicators in grid connected PV (photovoltaic) systems working in faulty and partial shading conditions. *Energy*, 86:42–50, Jun. 2015.

[35] L. Zhang, K. Sun, Y. Xing, L. Feng, and H. Ge. A Modular Grid–Connected Photovoltaic Generation System Based on DC Bus. *IEEE Transactions on Power Electronics*, 26(2):523–531, Feb. 2011.

[36] Ruo–li Tang, Zhou Wu, and Yan–jun Fang. Maximum power point tracking of large–scale photovoltaic array. *Solar Energy*, 134:503–514, Sep. 2016.

[37] F. Rong, X. Gong, and S. Huang. A Novel Grid–Connected PV System Based on MMC to Get the Maximum Power Under Partial Shading Conditions. *IEEE Transactions on Power Electronics*, 32(6):4320–4333, Jun. 2017.

[38] O. Bingöl and B. Özkaya. Analysis and comparison of different PV array configurations under partial shading conditions. *Solar Energy*, 160:336–343, Jan. 2018.

[39] S. Bana and R. P. Saini. Experimental investigation on power output of different photovoltaic array configurations under uniform and partial shading scenarios. *Energy*, 127:438–453, May. 2017.

[40] F. Belhachat and C. Larbes. Modeling, analysis and comparison of solar photovoltaic array configurations under partial shading conditions. *Solar Energy*, 120:399–418, Oct. 2015.

[41] Y. Mahmoud and E. F. El–Saadany. Enhanced Reconfiguration Method for Reducing Mismatch Losses in PV Systems. *IEEE Journal of Photovoltaics*, 7(6):1746–1754, Nov. 2017.

[42] T. S. Babu, J. P. Ram, T. Dragičević, M. Miyatake, F. Blaabjerg, and N. Rajasekar. Particle Swarm Optimization Based Solar PV Array Reconfiguration of the Maximum Power Extraction Under Partial Shading Conditions. *IEEE Transactions on Sustainable Energy*, 9(1):74–85, Jan. 2018.

[43] H. Patel and V. Agarwal. MATLAB–Based Modeling to Study the Effects of Partial Shading on PV Array Characteristics. *IEEE Transactions on Energy Conversion*, 23(1):302–310, Mar. 2008.

[44] D. L. King, W. E. Boyson, and J. A. Kratochvill. Photovoltaic Array Performance Model, Sandia Report No. SAND2004–3535.

[45] E. Skoplaki, A. G. Boudouvis, and J. A. Palyvos. A simple correlation for the operating temperature of photovoltaic modules of arbitrary mounting. *Solar Energy Materials and Solar Cells*, 92(11):1393 – 1402, Nov. 2008.

[46] G. M. Masters. *Renewable and efficient electric power systems.* John Wiley & Sons, Hoboken, second edition, Aug. 2013.

[47] S. Daliento, F. Di Napoli, P. Guerriero, and V. d'Alessandro. A modified bypass circuit for improved hot spot reliability of solar panels subject to partial shading. *Solar Energy*, 134:211–218, Sep. 2016.

[48] W. De Soto, S. A. Klein, and W. A. Beckman. Improvement and validation of a model for photovoltaic array performance. *Solar Energy*, 80(1):78–88, Jan. 2006.

[49] H. Tian, F. Mancilla–David, K. Ellis, E Muljadi, and P. Jenkins. A cell–to–module–to–array detailed model for photovoltaic panels. *Solar Energy*, 86(9):2695–2706, Jun. 2012.

[50] K. Ishaque, Z. Salam, H. Taheri, and Syafaruddin. Modeling and simulation of photovoltaic (PV) system during partial shading based on a two–diode model. *Simulation Modelling Practice and Theory*, 19(7):1613–1626, Aug. 2011.

[51] D. F. Teshome, C. H. Lee, Y. W. Lin, and K. L. Lian. A Modified Firefly Algorithm for Photovoltaic Maximum Power Point Tracking Control Under Partial Shading. *IEEE Journal of Emerging and Selected Topics in Power Electronics*, 5(2):661–671, Jun. 2017.

[52] A. Murtaza, M. Chiaberge, F. Spertino, D. Boero, and M. De Giuseppe. A maximum power point tracking technique based on bypass diode mechanism for PV arrays under partial shading. *Energy and Buildings*, 73:13–25, Apr. 2014.

[53] H. Fathabadi. Novel fast dynamic MPPT (maximum power point tracking) technique with the capability of very high accurate power tracking. *Energy*, 94:466–475, Jan. 2016.

[54] MATLAB and Simscape Toolbox Release R2018b. *MATLAB and Simscape Toolbox Release R2018b.* The MathWorks Inc., Natick, Massachusetts, United States, 2018.

[55] M. Carrasco and F. Mancilla–David. Maximum power point tracking algorithms for single–stage photovoltaic power plants under time–varying reactive power injection. *Solar Energy*, 132:321–331, Jul. 2016.

[56] M. G. Villalva, J. R. Gazoli, and E. R. Filho. Comprehensive Approach to Modeling and Simulation of Photovoltaic Arrays. *IEEE Transactions on Power Electronics*, 24(5):1198–1208, May. 2009.

[57] A. Angulo, M. Carrasco, F. Mancilla–David, A. Street, and R. Cárdenas. Experimental Parameter Extraction in the Single–Diode Photovoltaic Model via a Reduced–Space Search. *IEEE Transactions on Industrial Electronics*, 64(2):1468–1476, Feb. 2017.

[58] Y. Chaibi, M. Salhi, A. El–jouni, and A. Essadki. A new method to extract the equivalent circuit parameters of a photovoltaic panel. *Solar Energy*, 163:376–386, Mar. 2018.

[59] T. Kiuru, J. Mallat, A. V. Raisanen, and T. Narhi. Schottky Diode Series Resistance and Thermal Resistance Extraction From S–Parameter and Temperature Controlled I–V Measurements. *IEEE Transactions on Microwave Theory and Techniques*, 59(8):2108–2116, Aug. 2011.

[60] I. Jyothi, V. Janardhanam, Hyobong Hong, and Chel-Jong Choi. Current–voltage and capacitance–voltage characteristics of Al Schottky contacts to strained Si–on–insulator in the wide temperature range. *Materials Science in Semiconductor Processing*, 39:390–399, Nov. 2015.

[61] Dieter K. Schroder. *Semiconductor Material and Device Characterization, 3rd Edition*. John Wiley & Sons, Hoboken, Apr. 2005.

[62] K. P. O'Donnell and X. Chen. Temperature dependence of semiconductor band gaps. *Applied Physics Letters*, 58(25):2924–2926, Jun. 1998.

[63] O. Ya. Olikh. Review and test of methods for determination of the Schottky diode parameters. *Journal of Applied Physics*, 118(2):24502, Jul. 2015.

[64] Y. A. Çengel and M. A. Boles. *Thermodynamics an Engineering Approach*. McGraw–Hill, Boston, 8th edition, Jan. 2014.

[65] Z. Zhang, J. Wohlgemuth, and S. Kurtz. The thermal reliability study of bypass diodes in photovoltaic modules. In *Photovoltaic Module Reliability Workshop, Golden, CO, USA*, Feb. 2013.

[66] Y. H. Ji, D. Y. Jung, J. G. Kim, J. H. Kim, T. W. Lee, and C. Y. Won. A Real Maximum Power Point Tracking Method for Mismatching Compensation in PV Array Under Partially Shaded Conditions. *IEEE Transactions on Power Electronics.*, 26(4):1001–1009, Apr. 2011.

[67] J. Widén. A model of spatially integrated solar irradiance variability based on logarithmic station–pair correlations. *Solar Energy*, 122:1409–1424, Oct. 2015.

[68] M. Yue and X. Wang. Assessing cloud transient impacts on grid with solar and battery energy systems. In *2013 IEEE 39th Photovoltaic Specialists Conference (PVSC)*, pages 2348–2353, Jun. 2013.

[69] K. Lappalainen, A. Mäki, and S. Valkealahti. Effects of the Sharpness of Shadows on the Mismatch Losses of PV Generators under Partial Shading Conditions Caused by Moving Clouds. In *28th European Photovoltaic Solar Energy Conference and Exhibition, Paris, France*, pages 4081–4086, Sep. 2013.

[70] P. Beaucage, M. C. Brower, J. D. Frank, and J.D. Freedman. Development of a stochastic–kinematic cloud model to generate high–frequency solar irradiance and power data. In *41st World Renewable Energy Forum, American Solar Energy Society (ASES), Denver, CO, USA*, May. 2012.

[71] Deutsche Gesellshaft Für Sonnenenergie. *Planning and installing photovoltaic systems: A guide for installers, architects and engineers*. Earthscan Publications Ltd, London, 2nd edition, Sep. 2011.

[72] Unisys. Upper Air Data, Unisys Weather Information Systems, 2018.

[73] A. Andreas and T. Stoffel. NREL Solar Radiation Research Laboratory (SRRL): Baseline Measurement System (BMS); Golden, Colorado (Data); NREL Report No. DA–5500–56488., May. 2018.

[74] E. Rakhshani, K. Rouzbehi, A. J. Sánchez, A. Cabrera–Tobar, and E. Pouresmaeil. Integration of Large Scale PV–Based Generation into Power Systems: A Survey. *Energies*, 12(8), Apr. 2019.